AWARD NUMBER: W81XWH-14-1-0069

TITLE: Advanced Restoration Therapies in Spinal Cord Injury

PRINCIPAL INVESTIGATOR: Visar Belegu, Ph.D.

CONTRACTING ORGANIZATION: Hugo W. Moser Research Institute at Kennedy Krieger, Inc.
BALTIMORE, MD 21205

REPORT DATE: July 2017

TYPE OF REPORT: Final

PREPARED FOR: U.S. Army Medical Research and Materiel Command
Fort Detrick, Maryland 21702-5012

DISTRIBUTION STATEMENT: Approved for Public Release;
Distribution Unlimited

The views, opinions and/or findings contained in this report are those of the author(s) and
should not be construed as an official Department of the Army position, policy or decision
unless so designated by other documentation.

REPORT DOCUMENTATION PAGE

1. REPORT DATE	2. REPORT TYPE	3. DATES COVERED
July 2017	Final	15 April 2014–14 April 2017

4. TITLE AND SUBTITLE	5a. CONTRACT NUMBER
Advanced Restoration Therapies in Spinal Cord Injury	
	5b. GRANT NUMBER
	W81XWH-14-1-0069
	5c. PROGRAM ELEMENT NUMBER

6. AUTHOR(S)	5d. PROJECT NUMBER
Visar Belegu, Ph.D.(performed research & credited w/ content)	
	5e. TASK NUMBER
	5f. WORK UNIT NUMBER
E-Mail: cox@kennedykrieger.org	

7. PERFORMING ORGANIZATION NAME(S) AND ADDRESS(ES)	8. PERFORMING ORGANIZATION REPORT NUMBER
Hugo W. Moser Research Institute at Kennedy Krieger, Inc. 707 North Broadway Baltimore, MD 21205	

9. SPONSORING / MONITORING AGENCY NAME(S) AND ADDRESS(ES)	10. SPONSOR/MONITOR'S ACRONYM(S)
U.S. Army Medical Research and Materiel Command Fort Detrick, Maryland 21702-5012	
	11. SPONSOR/MONITOR'S REPORT NUMBER(S)

12. DISTRIBUTION / AVAILABILITY STATEMENT

Approved for Public Release; Distribution Unlimited

13. SUPPLEMENTARY NOTES

14. ABSTRACT

Functional electrical stimulation (FES) is a therapeutic intervention based on the concept that the plasticity of the impaired central nervous system can be harnessed through induction of activity. As an activity-based intervention, FES is administered to patients with spinal cord injuries. The mechanisms through which FES generates neurological recovery remain unclear. We have now development a mouse model for long-term delivery of FES after SCI, and this is the most significant deliverable of the current project. The major finding that we have uncovered through this model is that FES improves neurological function particularly motor function. This improvement was observed in the subacute and subchronic stages of SCI. In our work, where the SCI was moderate the improvements pertained to fine motor function but not gross motor function. Direct mechanisms that lead to such improvements remain unresolved but we have begun to uncover these as well. The major discovery in this area is that mechanisms responsible for neurological recovery include a regenerative oligodendroglia response. This finding is particularly relevant because it increases the clinical utility of FES to include treatment for myelin-based disorders such as multiple sclerosis.

15. SUBJECT TERMS: Spinal cord injury, neural progenitor cells, functional electrical stimulation, neurological recovery, myelination, remyelination

16. SECURITY CLASSIFICATION OF:			17. LIMITATION OF ABSTRACT	18. NUMBER OF PAGES	19a. NAME OF RESPONSIBLE PERSON USAMRMC
a. REPORT	b. ABSTRACT	c. THIS PAGE			19b. TELEPHONE NUMBER (include area code)
U	U	U	UU	83	

Table of Contents

INTRODUCTION

Spinal cord injury (SCI) causes paralysis as well as disruption of sensory and autonomic functions. Severity of injury, and the extent of neurological impairment following SCI, limits subsequent neurological recovery. Persons with severe SCI experience limited neurological recovery (Kirshblum et al., 2004; McDonald et al., 2002), and the chances of neurological recovery become even smaller in the chronic phase of SCI (McDonald et al., 2002). Previous studies, however, suggest that through continued rehabilitation efforts, recovery of sensation, function, mobility, and independence in individuals with chronic SCI is possible, months and even years after injury (Harkema et al., 2012; McDonald et al., 2002; Sadowsky et al., 2013). This information has led to increased focus on the development of rehabilitation programs appropriate for individuals with chronic SCI. In particular, active rehabilitation therapy, which aims to induce neurological improvements through continued physical movements, is receiving renewed attention, as studies show that it can effectively increase muscle mass and strength, as well as independence in activities of daily living (ADL) in individuals with SCI (Harkema et al., 2012; Karimi, 2013; Lorenz et al., 2012; Sadowsky et al., 2013). One of the most widely adapted intervention components of active rehabilitation therapy includes functional electric stimulation (FES) (Harkema et al., 2012; Karimi, 2013; Lorenz et al., 2012). The mechanisms through which FES induces functional recovery remain poorly understood. Remyelination has been suggested as a possible mechanism considering it is an activity-dependent process; however, clinical studies are not sufficient to address this question. Therefore, we have undertaken a preclinical study where we have developed a mouse model of FES in injured mice. In addition, we are applying FES in injured transgenic mice, allowing us to lineage trace neural progenitor cells that have shown to be induced to proliferate and differentiate as a consequence of FES. Furthermore, the Award has allowed us to generate a transgenic mouse that promises to be transformative, not only for the study of FES in myelination, but in all myelin related pathologies.

KEYWORDS

Spinal cord injury (SCI)
Neural progenitor cells (NPCs)
Functional electrical stimulation (FES)
Neurological recovery
Myelination
Remyelination

ACCOMPLISHMENTS

What were the major goals of the project?
SPECIFIC AIM 1: Determine if functional electrical stimulation (FES) in a mouse model of chronic spinal cord injury (SCI) induces proliferation and differentiation of genetically labeled NPCs.
SPECIFIC AIM 2: Determine if FES induces remyelination by mature oligodendrocytes in a mouse model of chronic SCI.
SPECIFIC AIM 3: Determine if functional electrical stimulation in a mouse model of chronic SCI induces cortical plasticity as measured by resting state functional magnetic resonance imaging (rs-fMRI).

General Comments:
The work funded under W81XWH-14-1-0069 was organized into three related *in vivo* basic science Specific Aims. The ultimate goal of these studies was to provide data from mouse models of spinal cord injury that will inform future therapies for individual humans living with spinal cord injury and/or disease. Specifically the research done under this Award was designed

to test aspects of FES (functional electrical stimulation)-enhanced post-SCI (spinal cord injury) recovery in mouse models. FES applied to peripheral nerves has been shown to enhance recovery of motor function in humans living with SCI and in rat models In rodent SCI experiments, the transition from rats to mice as the animal of choice has been inspired by the availability of important transgenic mouse lines and the promise of future lines that will greatly aid in understanding the cellular mechanisms of spinal cord repair and subsequent functional recovery.

Dr. Belegu and colleagues were experts at all surgical (SCI and FES electrode implantation), behavioral and tissue analysis procedures and interpretation of data in rat models. Procedures and assays were adapted to mice in this project.

Activities and achievements for each specific aim will be discussed separately, and places where the work for each aim intersects with another will be pointed out.

What was accomplished under these goals?
<u>Specific Aim 1</u>
Determine if functional electrical stimulation (FES) in a mouse model of chronic spinal cord injury (SCI) induces proliferation and differentiation of genetically labeled NPCs (Months 1-12).
<u>Hypothesis SA 1:</u> FES will induce proliferation of NPCs in mice with chronic SCI. FES will induce differentiation of NPCs and OPCs into mature oligodendrocytes in mice with SCI.
In brief, the goals of Specific Aim 1 were as follows. SA 1 proposed using commercially available transgenic mice in SCI/FES experiments. Dr. Belegu purchased and bred several lines of mice. Analysis of spinal cord tissue from moderately injured animals that were treated with FES as a therapeutic intervention and examined for motor function during the survival period, tested the hypothesis that FES acts partly by 1) enhancing proliferation of neural progenitor cells (NPCs) in the spinal cord and 2) improving the rate and amount of differentiation of these progenitors into one or more of the following mature cell types: neurons, astrocytes, microglia and especially myelinating oligodendrocytes. Participation of new (born post-injury), remyelinating oligodendrocytes in repair and recovery forms the basis for SA 2 which will be discussed later.

For SA, 1 adult mice from several transgenic lines were purchased from Jackson Laboratories.
- C57BL/6-Tg(Nes-cre/ERT2)KEisc/J abbreviated **nestin-CreER,**
- B6.129(Cg)-Tg(CAG-Bgeo/GFP)21Lbe/J (Z/EG), abbreviated **Z/EG/GFP** (green fluorescent protein)
- B6.129X1-Gt(ROSA)26Sortm1(EYFP)Cos/J abbreviated **ROSA-YFP** (yellow fluorescent protein)

<u>Experimental Strategy:</u> Using the protein nestin as a marker for NPCs, Nestin-CreER animals were mated with either Z/EG GFP or ROSA- YFP animals. Progeny were Nestin CreER positive, as well as positive for either the GFP or YFP reporter sequence. Adult progeny underwent moderate contusive spinal cord injury (50 kdyn). At either one week or four weeks after injury and recovery from surgery, the animals were injected with 4-hydroxytamoxifen to induce CreER recombination. After successful recombination, new nestin positive cells (NPCs) were to express the reporter protein GFP or YFP. The nestin positive/GFP or YFP positive cells (NPCs) fluoresce green when exposed to appropriate wavelengths of light during fluorescence microscopy. In order to label dividing cells in these same animals, a dose of EdU (5-ethynyl-2'-deoxyuridine), an alternative to the widely used BrdU (5-bromo-2'-deoxyuridine) was given several days after the free 4-hydroxytamoxifen cleared the animal's system.

Spinal Cord Injury Surgery: After deep anesthesia was reached, the mouse's back was shaved and wiped with betadine. Ophthalmic ointment was applied to the eyes to prevent drying. Anesthesia depth was monitored regularly before and during the surgery by testing for lack of response to a toe pinch. Mice were placed on a heating pad to maintain body temperature at 37 degrees C. A 2cm long midline incision was made in the mid-lower back and the muscles gently dissected away to expose the T8-10 spinal vertebrae. The dorsal aspect of the T9 veterbra was removed to expose the underlying spinal cord. After the spinal cord impact, muscles were repaired with a running absorbable suture and the skin closed with wound clips.

After laminectomy at T9, clamps were attached to the spinous processes of T8 and T10 vertebrae and the mouse was secured into the impactor device (Infinite Horizon-impact was computer controlled). Injury was caused at T8-9 via piston impact on the surface of the cord at a force of 50 kdyn (moderate contusion injury). Clamps were removed and the mouse removed from the device. Muscles were sutured and the skin closed with wound clips.

Tests for gross and fine motor function were given weekly throughout the experimental period. Gross motor function was assessed by the Open Field Locomotion Monitoring System (Tatem et al, 2014). Tests for fine motor function were the grid walk, horizontal ladder and Rotarod. Baseline behavior tests were performed seven days prior to spinal cord surgery. The first post-injury testing took place 24 hours after surgery and was repeated weekly until the end of the experiment.

FES: After drug treatments (4-hydroxytamoxifen to induce recombination and EdU), animals were divided randomly into two groups of at least six mice. One group was the "sham operated" group. FES was applied to animals in the second group abbreviated "FES." See Figure 1 for photos of electrode placement surgery. In all animals, FES electrodes were implanted and sutured in the anterior tibialis muscle adjacent to (but not touching) the common peroneal nerve in both hindlimbs. Beginning 24 hours after electrode implantation, FES was applied according to the proposed schedule. The only difference between the two groups was whether FES was applied. These electrodes remained in place for the duration of the stimulation experiment survival period. The FES unit was activated one time nightly (12-1 A.M.). The FES pattern was 1 second (sec) stimulation of one common peroneal nerve followed by 1 sec of rest; 1 sec of stimulation of the peroneal nerve in the other hindlimb followed by 1 sec of rest and the cycle repeated for an hour. The administered stimulus pulses were monophasic, 3 V, 200 µs long, and 20 Hz and produced alternating flexion of the hindlimbs that approximated bilateral stepping (Becker et al., 2010).

At the end point of each experiment, mice were perfused with paraformaldehyde and spinal cords were removed, frozen and sectioned on a cryostat, usually in the longitudinal plane. Double or triple fluorophore Immunofluorescence was performed. Numbers of cells expressing nestin/GFP or YFP as well as EdU were considered to be newly born NPCs. These cells were counted in the spinal cord sections and compared between the two treatment groups (sham and FES) using design-based stereology (Optical Fractionator, StereoInvestigator, MBF Bioscience).
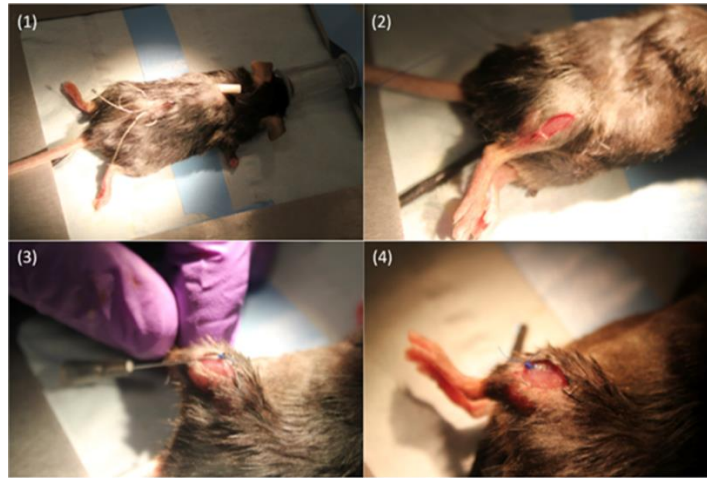
Figure 1. Implanting FES Electrodes in the Mouse Hindlimb

(1) Electrodes were inserted between the shoulder blades under the skin and were shuttled down to the lower back. (2) An incision was made near the common peroneal nerve. (3) The electrode was shuttled under the skin to the hindlimb incision site. (4) The electrode was implanted in and sutured to the anterior tibialis muscle without touching the nerve. Electrodes were implanted in both hindlimbs.

Year 1 SA 1 Activities and Accomplishments

1. ACURO: The Johns Hopkins University Institutional Animal Care and Use Committee and ACURO approved all procedures to be used in SA 1 and 2.
2. Breeding of transgenic mice: Breeding pairs of three transgenic mouse lines were purchased from Jackson Laboratories. Breeding of the nestin-CreER animals with the ROSA-GFP animals was more successful than breeding the nestin-CreER animals with the originally proposed Z/EG/GFP mice. ROSA-YFP was chosen as the reporter line and used in all experiments.
3. Administration of 4-hydroxytamoxifen and EdU: During breeding of the mice and expansion of the Nestin-Cre/ROSA-YFP colony, experiments were performed to test optimal doses and routes of administration of both 4-hydroxytamoxifen and EdU. Uninjured transgenic animals (adults) were used for these preliminary experiments.
   a. A dose of 4mg 4-hydroxytamoxifen (2 mg/day X two days) labeled cells that were both nestin and YFP immunopositive (Figure 2) thus validating a basic principle of the project. However, these double labeled cells were not in sufficient numbers for the planned spinal cord injury experiments. These results indicated that recombination was only partially successful. Further recombination experiments in uninjured tg (transgenic) progeny were performed. Analysis of data showed that a dose of 5mg 4-hydroxytamoxifen per day for 5 days at the end of the FES period resulted in sufficient numbers of nestin/YFP positive NPCs for future SCI/FES experiments.
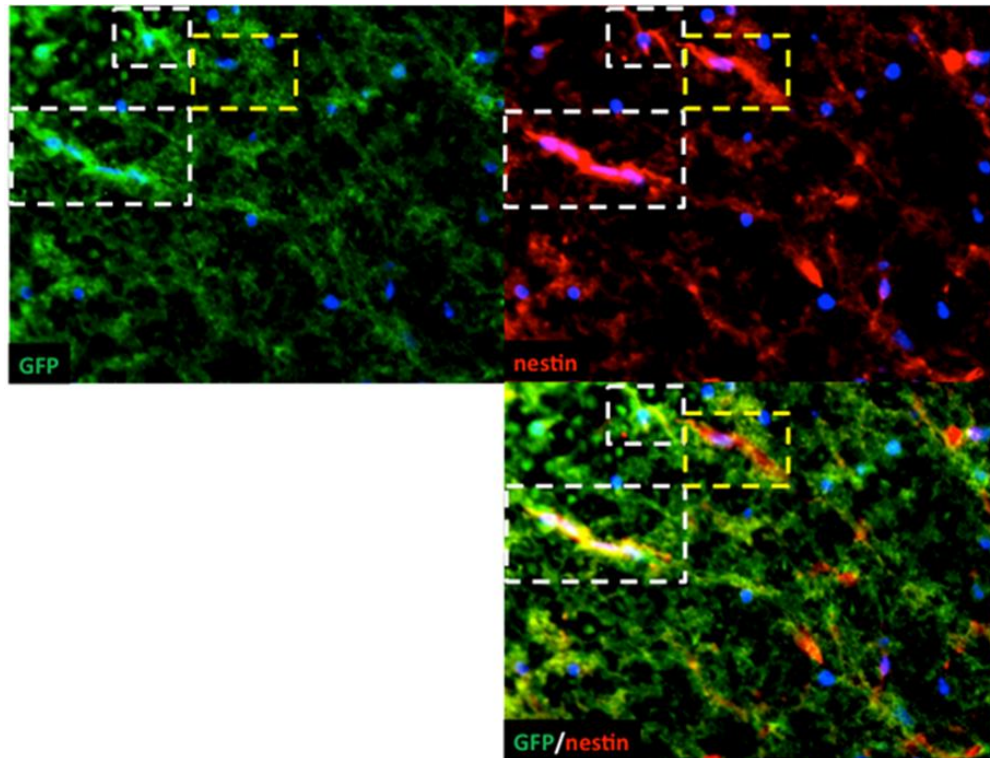
Figure 2. After recombination induced in an uninjured animal, some cells were both nestin-positive and YFP positive.

YFP reporter from the nestin promoter labels NPCs in nestin-CreER/ROSA-YFP mice. White boxes mark YFP-labeled NPCs whereas the yellow boxes label a nestin positive cell that has not undergone CreER. Note that in this figure and all others in this report YFP has been mislabeled as GFP. Both fluoresce green.

b. Intraperitoneal injection of EdU was more effective at labeling dividing cells in the spinal cord than administration of the compound via drinking water (data not shown). A pulse of 25mg EdU/kg given on the last day of FES was found to label sufficient dividing cells, both in the injury epicenter and in regions rostral and caudal to it. See Figure 3. No FES electrodes were implanted in this EdU experiment.
c. After preliminary cell proliferation results were analyzed in early Year 2, the EdU dose was increased to 40mg/kg in order to obtain sufficient numbers of dividing cells.
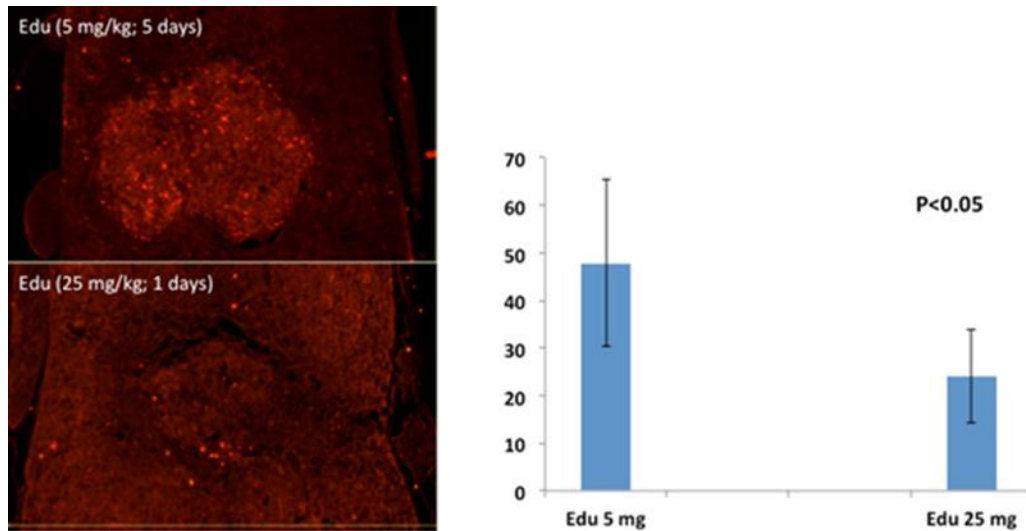
Figure 3. EdU Administration 4 weeks post-SCI

EdU administration in chronically injured mice. While Edu injected daily for 5 days with 5mg/kg (25mg/kg total) labels more dividing cells, these cells were located predominately in the injury epicenter and were of a non-neural lineage. A bolus of 25mg/kg labels fewer total cells but label does not predominate in the injury center.

4. Spinal Cord Injury and FES
   a. After participating in a hands-on mouse SCI training course given by Dr. Aileen Anderson of the Christopher and Dana Reeve Foundation during the second half of Year 1, Dr. Belegu and colleagues began spinal cord injuries and application of FES in 30 C57Bl wild type mice. Non-transgenic mice were used in this experiment in order to obtain first results for the FES experiments. The tg (transgenic) colony was expanding at this time. This first experiment was titled Aim 1 Experiment 1. To repeat, the primary goals were to test the hypotheses that FES after SCI will enhance cell proliferation in and near the injury and that FES will enhance recovery of motor function after SCI. Experiment 1 was a **subacute** experiment: FES was initiated seven days after SCI surgery.

   b. After surgery, animals recovered naturally for six days with no intervention other than routine pain medication and possibly antibiotic treatment for bladder infections. On day six post-SCI, FES electrodes were implanted and FES begun 24 hours later (day seven post-SCI). Most animals underwent FES for four weeks before EdU injection and perfusion. Results from this experiment were analyzed in Year 2.
   c. At the end of Year 1, Dr. Belegu and colleagues injured an additional 20 C57Bl mice in order to refine surgical techniques and application of FES. Their goals were to
      i. Improve consistency and efficiency of the SCI and FES electrode implantation surgeries, making sure survival rate was high and post-surgery care was effective.
      ii. Gain experience and efficiency with behavioral assays.

Summary of Accomplishments Year 1
   1. Established successful breeding colony of Nestin-CreER and ROSA-YFP breeding transgenic animals.

2. Determined in uninjured adult progeny of the above animals that a dose of 5mg 4-hydroxytamoxifen/day for five days resulted in sufficient and specific labeling of NPCs.
3. Determined in a subacute SCI experiment Aim 1 Experiment 1 using C57Bl WT mice that one dose of Edu specifically and sufficiently labeled dividing cells in the spinal cord.

Year 2 SA 1 Activities and Accomplishments
1. Aim 1 Experiment1: FES in a subacute (six days) model of Contusive SCI
    a. At the end of Year 1, Dr. Belegu initiated a subacute SCI/FES experiment in 30 C57Bl mice (Aim 1 Experiment 1). See page five of this report. Six days after SCI, severity of injury was determined by behavioral testing. Electrodes were implanted in all animals and the animals randomly divided into two groups. One group was the "sham operated" group and received no FES. FES was applied to the other group of animals.
    b. In order to get an early look at cell proliferation, six animals (three sham and three FES) were removed from the cohort. On day six of FES, EdU was injected in a pulse of 25mg/kg into these six animals. On day seven of FES, these six animals were perfused and their spinal cords dissected. After longitudinal cryostat sectioning of the cord, EdU immunohistochemistry was performed. Dividing cells were counted in the injury epicenter and at distances rostral and caudal to it. Dividing cells were present in the injured cord as shown by EdU immunolableing, but no experiment was done to determine cell type.
    c. See Figure 4 for results of the "early" experiment. A two-way ANOVA analysis of the data showed that six days of FES did not enhance cell proliferation after SCI. This result was not unexpected due to the short FES application period (six days). FES was continued in the remaining experimental animals (approximately 24) at this time point; evenly divided between sham and FES.
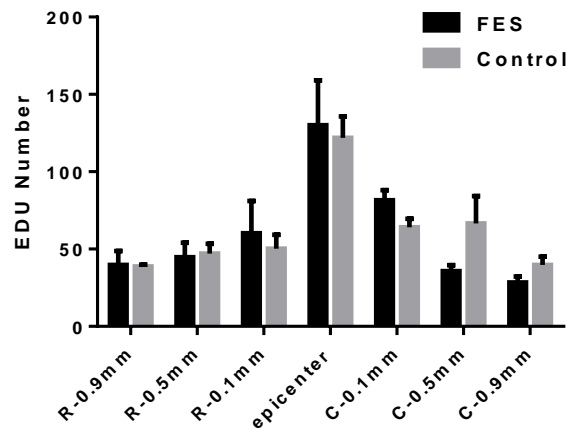
Figure 4. Cell Proliferation after 6 days of FES in chronically injured C57Bl mice.

Six days of FES in chronically injured mice did not enhance cell proliferation at the injury epicenter or rostral or caudal to it. N=3 sham operated control. N=3 FES treatment.

    d. FES was continued for another three weeks (four weeks total) in the remaining FES animals from Experiment 1.On the last day of FES, all animals were injected with one pulse of EdU at 40mg/kg. After perfusion of the animals, dissection and cryostat

sectioning of the spinal cord, EdU immunohistochemistry was performed on longitudinal sections from six animals in each group (sham and FES). As shown in Figure 5, four weeks of FES was effective at enhancing cell proliferation in spinal cord injured mice. The peak location of the mitogenic response was the injury epicenter, however the effect extended up to 5-mm rostral and caudal from the injury epicenter. Statistical difference was determined by t-test comparing numbers of cells at given distances from the epicenter between sham and FES groups. N=6 for each group.

e. Also in Aim 1 Experiment 1, FES was shown to increase the number of mature oligodendrocytes in the injured spinal cord. Mature oligodendrocyte cell bodies in tissue sections were immuno-labeled with an antibody to APC-CC1. See Figure 6. Unlike the cell proliferation response that reflects all cell types in the cord, the oligodendrocyte response was most significant caudal to the injury epicenter. However, the response does extend significantly 5mm rostral to the epicenter and 5mm caudal to it. Statistical difference was determined by t-test, comparing numbers of oligodendrocytes at a given distance from the injury epicenter between sham and FES groups. These results suggest that proliferating cells including possible oligodendrocyte precursor cells (OPCs) migrate from the injury epicenter to replace dying oligodendrocytes as far as 5mm away from the injury epicenter.

Figures 5 and 6 follow.
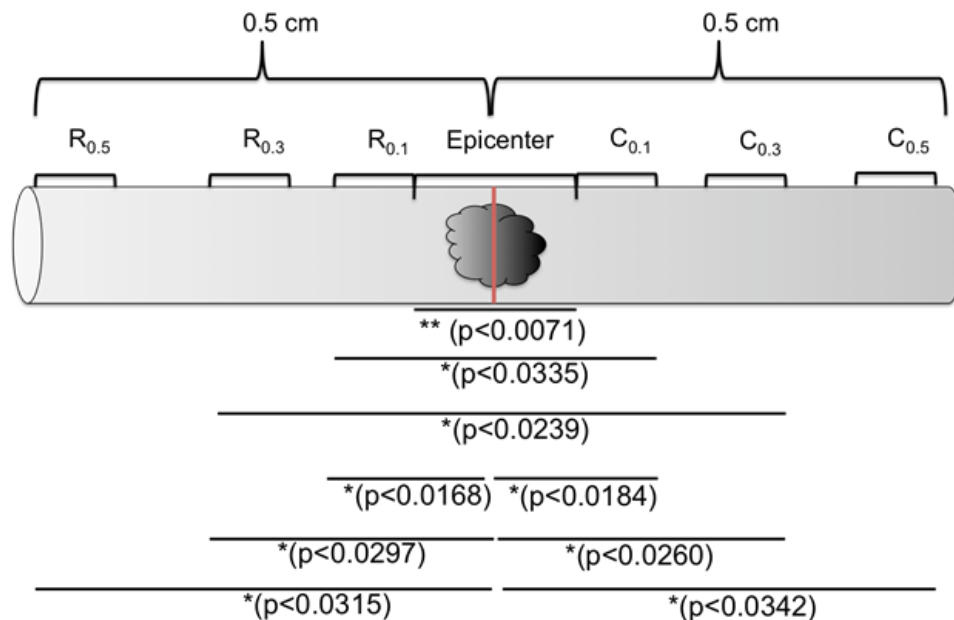
Figure 5. 4 Weeks of FES Enhances Cell Proliferation in a Subacute Model of Spinal Cord Injury

Cell proliferation in response to FES. R was rostral to the SCI epicenter; C was caudal to the SCI epicenter; the subscript numbers indicate the distance in centimeters from the injury epicenter. * signifies statistical difference by t-test between the FES (n=6) and non-FES (n=6) groups with a p-value of <0.05; ** signifies statistical difference by t-test between the FES and non-FES groups with a p-value of <0.01.

Figure 6.

Figure 6. 4 Weeks of FES Increases the Number of Mature Oligodendrocytes in the Injured Spinal Cord of C57Bl mice (subacute injury)

The number of oligodendrocytes increases in response to FES in subacute SCI. R was rostral to the SCI epicenter; C was caudal to the SCI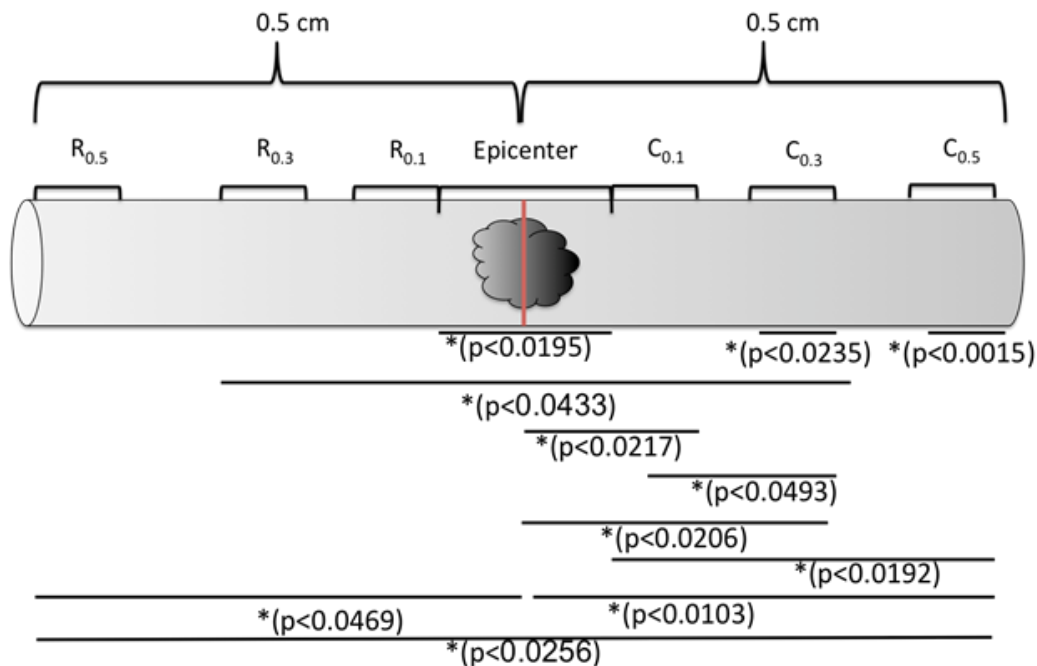 epicenter; the subscript numbers indicate the distance in centimeters from the injury epicenter. * signifies statistical difference by t-test between the FES and sham groups with a p-value of <0.05; ** signifies statistical difference by t-test between the FES and sham groups with a p-value of <0.01.

    f.   Functional Motor Recovery in Aim 1 Experiment 1: At the end of the FES period (four weeks), animals were tested for recovery of fine motor skills using the grid-walk test. Results are shown in Figure 7 below and indicate that in a sub-acute model of mouse SCI, application of FES for four weeks reduces step errors significantly (p<.019) when compared to performance in sham animals.
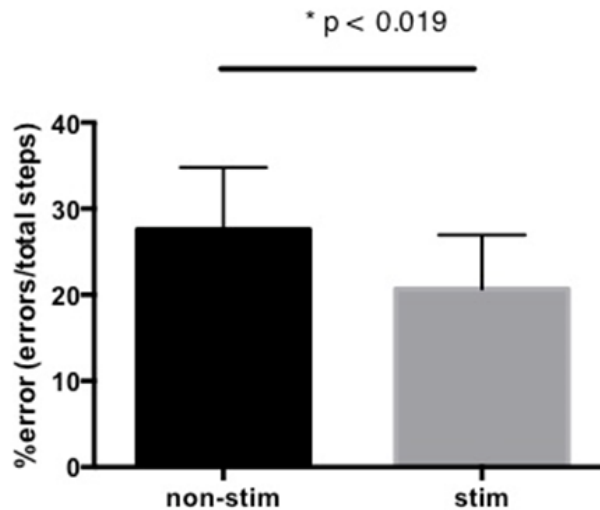
Figure 7. Four Weeks of FES Significantly Lowers the % Errors Made by Spinal Cord Injured Mice as Measured by the Grid-Walk Test

4 weeks of FES improves fine motor function in spinal cord injured C57Bl mice. N=11 for sham (non-stim) and n=13 for FES (stim) groups. Score was calculated as number of errors made per total number of steps taken (% error).

2. <u>Aim 1 Experiment2 - FES after chronic (four weeks) spinal cord injury</u>
   a. This second SCI experiment used C57Bl WT mice in a chronic model of SCI. One week after baseline motor function assessment, Dr. Belegu performed a 50kdyn contusion spinal cord injury on all animals in the cohort. After four weeks of natural recovery without therapeutic intervention, except for pain medication or possible antibiotic treatment for bladder infection, FES electrodes were implanted in all animals as described earlier. Animals were randomly assigned in equal numbers to either the sham group or the FES group. FES was begun 24 hours after electrode implantation and continued nightly for four weeks.
   b. At the end of the four-week FES period, fine motor skills were assessed by using the Rotarod test. Results are shown in Figure 8 and are expressed as latency (in seconds) to a fall from the turning rod. FES animals stayed on the rod significantly longer than sham animals (p<.0240) indicating enhancement of functional recovery from a chronic (4week) injury. N=10 sham, N=12 FES
   c. Anatomical analysis for cell proliferation in this experiment is discussed in accomplishments for Year 3 (a period of No Cost Extension).
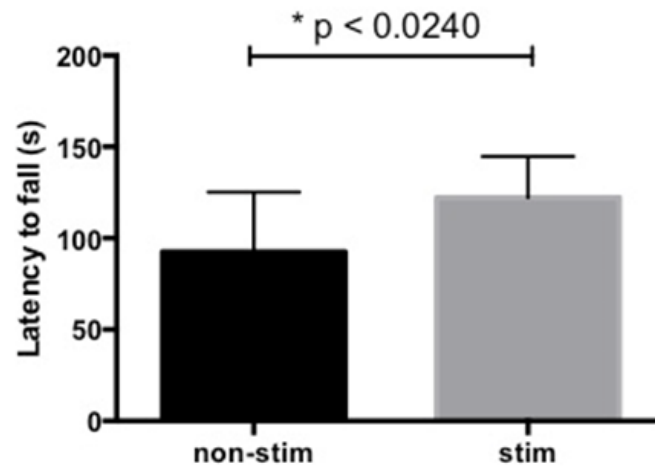
Figure 8. 4 Weeks of FES Significantly Increases the Latency to a Fall in Chronically Injured C57Bl Mice as Assessed by Rotarod

In chronically injured mice, 4 weeks of FES significantly improves (p<.0240) aspects of fine motor function as tested by Rotarod. N=10 for sham (non-stim) and N=12 for FES (stim).

3. Aim 1 Experiment 3: FES in chronically injured (four weeks) Nestin-CreER/YFP mice
   a. The timeline and severity of the injury and FES application in these animals follows that described for Aim 1 Experiment 2 discussed above. Injury, electrode placement, and FES all took place in Year 2. No behavior testing was done on these animals. In a sub-cohort of these chronically injured transgenic animals, (N=5 sham and N=5 FES), FES was applied for two weeks rather than four. These animals were anesthetized and the spinal cords and brains were dissected out and frozen for Western blot procedures. However Western blots were not performed.

Year 3 SA 1 Activities and Accomplishments
1. Tissue Analysis:
   a. Microglia In Year 3 of this project, analysis of data and tissue from SA 1 Experiments 1-3 was continued. To assess the possibility that FES may affect the level of inflammation in the injured cord, a preliminary estimate of the number dividing microglia was made using the Optical Fractionator (design-based stereology). Edu/Iba1 double-labeled cells were localized in the injury epicenter and 1, 3 and 5 mm rostral and caudal to the epicenter. Iba1 (ionized calcium-binding adapter molecule 1) is a specific marker for microglia. No difference in the numbers of dividing microglia was found at any level in the injured cord when sham was compared to FES treatment. Data not shown.
   b. Astrocyte activation. In addition to Iba1, GFAP immunohistochemistry was done to determine the activation status and proliferation of astrocytes at and near the injury epicenter. Dr. Belegu decided to expedite the GFAP analysis by employing the Molecular Devices IXM High Content Imager. In this process, immunofluorescent images were captured at 20X, and then stitched together digitally to create an image of the entire section. The stitched image can be reduced in size and then analyzed. In these images, the area of positive immunofluorescence in the section can be

calculated and expressed as a fraction of the total section area. Images were captured using this approach but the data was not quantitatively analyzed. See Figure 9 below for examples.
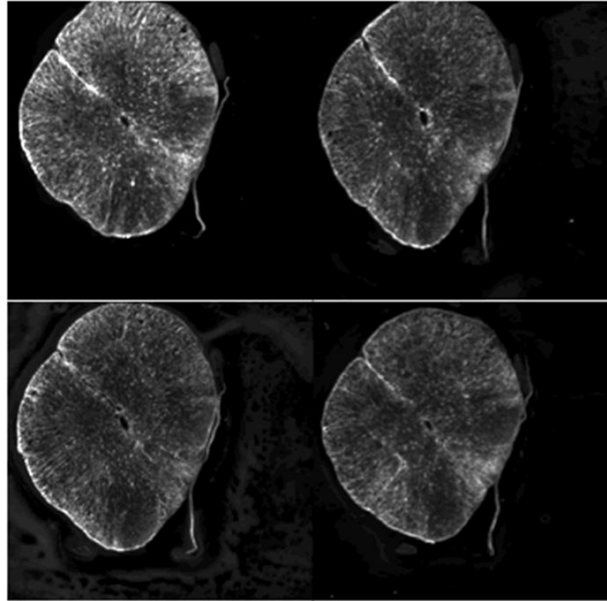
Figure 9. GFAP Immunoreactivity Changes with Distance from the Injury Epicenter

GFAP expression varies with distance from the epicenter of the spinal cord injury. Regions of greater brightness as in the upper left image may reflect astrocyte activation or proliferation.

c. Oligodendrocytes in tg animals. Investigators determined that genetically labeled NPCs in the injured spinal cord differentiate into oligodendrocytes, as determined by expression of YFP and APC-CC1. See Figure 10. However, not all APC-CC1^{+} cells were YFP[+]. This indicates that these cells originated from NPCs but they differentiated into APC-CC1 expressing oligodendrocytes before 4-hydrodroxytamoxifen induced recombination or that they originated from another precursor cell such as an OPC (oligodendrocyte precursor cell) not labeled with YFP). Statistical analysis to determine if FES changes the fate of genetically labeled NPCs was not completed.
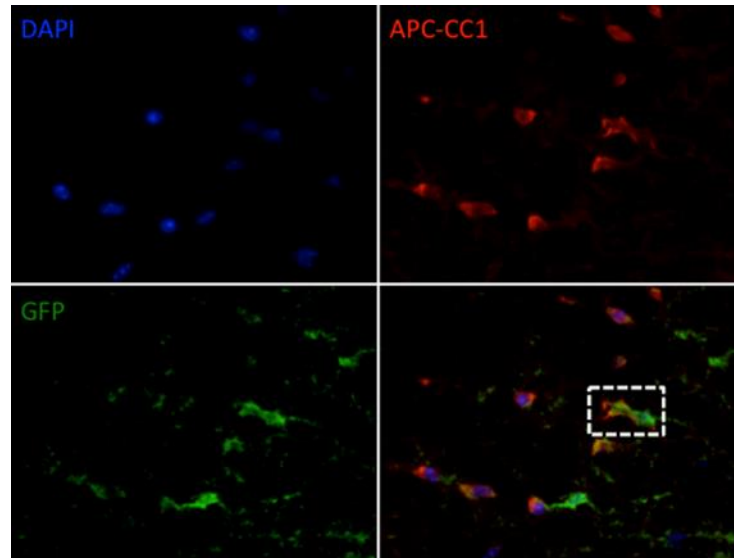
Figure 10. Some Mature Oligodendrocytes in the Injured Spinal Cord are both Nestin and YFP positive.

In the injured spinal cord, mature oligodendrocytes were generated from nestin+ neuronal progenitor cells. The white squares highlight two nestin+ cells (green) where only one cell has differentiated into a mature oligodendrocyte.

2. <u>Aim 1 Experiments 1 and 2: Gross Motor Function as Measured by Open Field Activity Monitoring (Tatem et al, 2014)</u>
   a. Late in Year 3, Dr. Belegu completed analysis of open field locomotion assays for both the subacute and the chronic SCI/FES experiments. In this test, mice are placed in a plexiglas pen lined with photocell emitters and receptors which create a grid of light beams near the floor and at different heights within the chamber. "Beambreaks" are counted by the device. The number of times an animal breaks a beam reflects the activity level of the animal.
   b. In Experiment1, a subacute model of SCI, application of FES for four weeks improves fine aspects of motor function (see Figure 7) but not gross motor function (Figure 11). Lack of an effect could be due to the endogenous recovery mechanisms in this moderate contusion model of SCI: however, an effect would perhaps be observed in a more severe SCI.
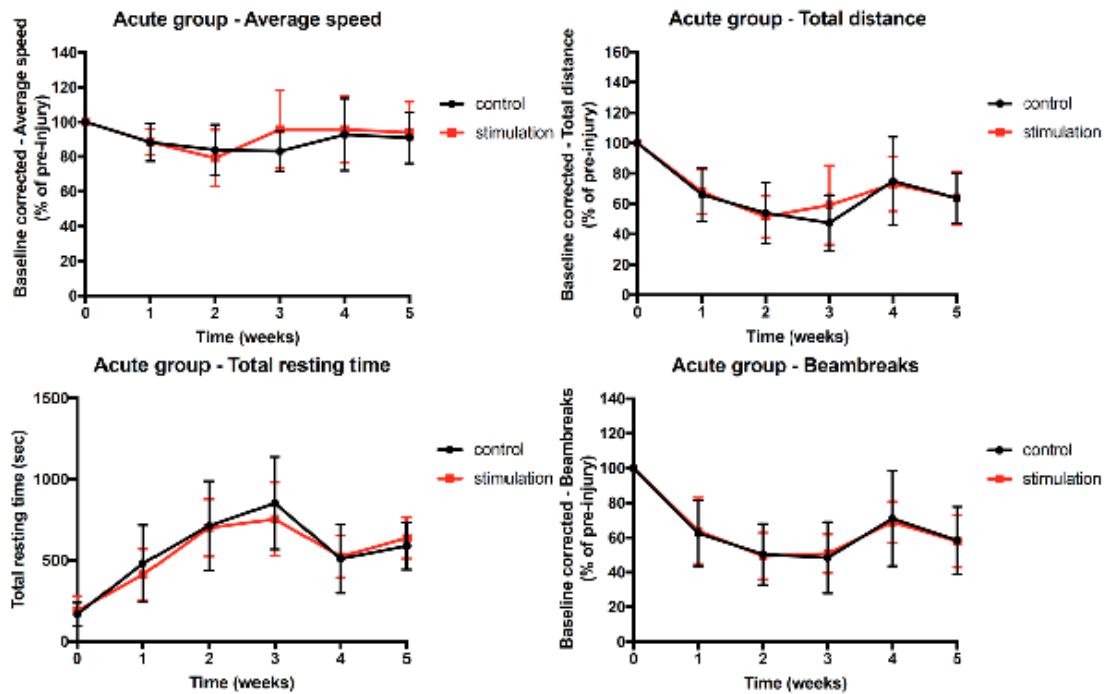
Figure 11. 4 Weeks of FES in Subacute Spinal Cord Injury (Aim1 Experiment1) does not Improve Gross Motor Function as Measured by Parameters of Open Field Activity Monitoring

FES was initiated at week 1 as seen on the graphs above, 6 days after moderate spinal cord injury. Four parameters of locomotion were tested: 1) average speed of locomotion (percent of baseline pre-injury speed) 2) total resting time during the session (in seconds), 3) Total distance walked (percent of pre-injury distance) and 4) Beam breaks (percent of pre-injury).

c. In Experiment 2, a chronic model of SCI, FES was begun four weeks after injury and continued for four weeks. In total this experiment was eight weeks long. In contrast to the results of Experiment1, Figure 12 shows that application of FES for four weeks did significantly improve aspects of gross motor function beginning at week six of the experiment (two weeks after FES was begun) as well as improving a measure of fine motor function (see Figure 8). Results from the subacute and chronic experiment indicate that perhaps some measure of natural recovery and healing must take place before FES can be effective for the gross measures of locomotor function, which reflects general activity.
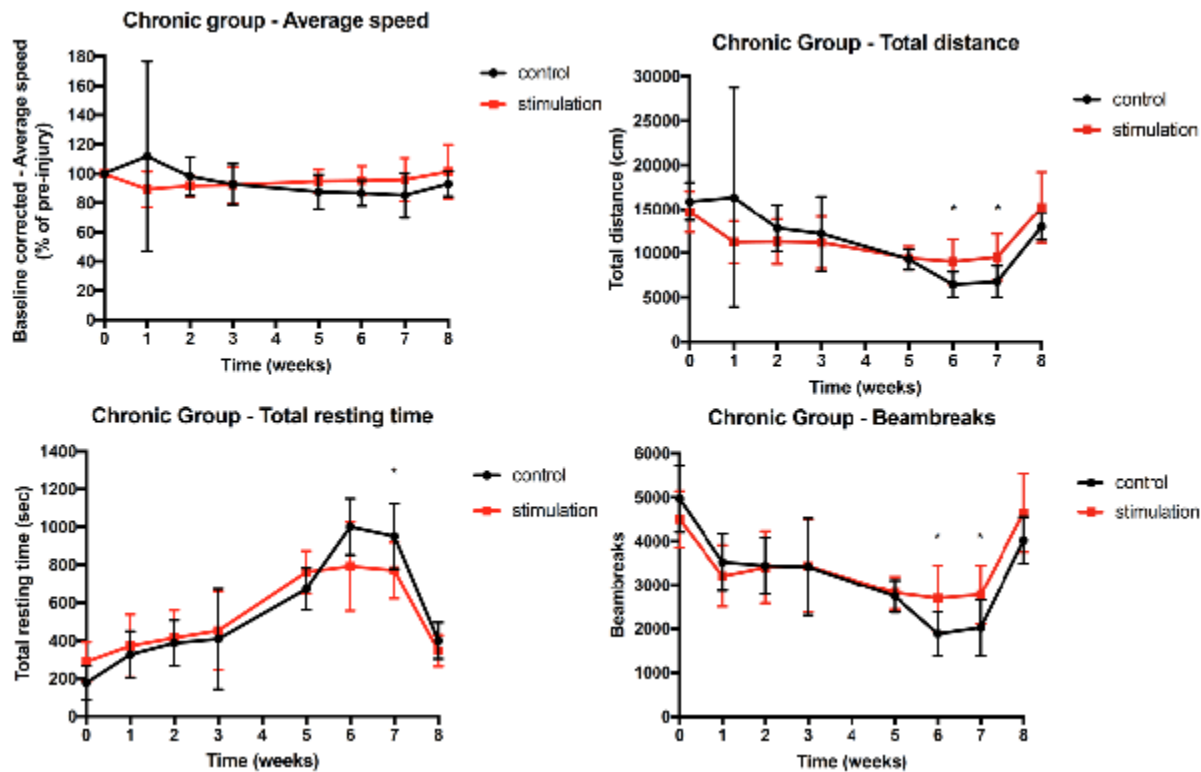
Figure 12. FES Improves Aspects of Gross Motor Function in a Mouse Model of Chronic Spinal Cord Injury

FES was begun at Week 4, 4 weeks after spinal cord injury. Average speed was expressed as percent of preinjury speed. Total resting time was in seconds. Total distance covered was expressed in cm (in contrast to per cent of pre-injury distance as in Figure 9). Beambreaks were expressed as total numbers rather than percent of pre-injury as in Figure 9.

* indicates $p<.05$ when control (sham) function is compared to that in the FES group.

Major Findings of Specific Aim 1

1. Four weeks of FES following SCI improves gross motor function in a chronic model of moderate SCI in mice, but not in a subacute model.
2. Four weeks of FES applied in both chronic and subacute models of SCI significantly improves fine motor function as measured by grid walk and Rotarod, when performance in FES animals is compared to that in sham animals.
3. Four weeks of FES following a chronic, moderate SCI significantly increases cell proliferation in the injury epicenter and up to 5mm rostral and caudal to it, as measured by EdU immuopositive cell counts.
4. FES applied in a chronic model of SCI increases the number of mature oligodendrocytes as measured by counting APC-CC1 positive cells in the injury epicenter and up to 5 mm rostral and caudal to it.

Specific Aim 2
Determine if FES induces remyelination by mature oligodendrocytes in a mouse model of chronic SCI (Months 1-24).
Hypothesis: FES will induce remyelination by recently born, mature oligodendrocytes in a mouse model of contusive spinal cord injury.

General Comments

The goal of Specific Aim 2 was to investigate the process of re-myelination after SCI in mice and to ascertain if and how application of FES in subacute and chronic injury models enhanced remyelination of surviving demyelinated axons. As discussed in the original proposal, remyelination after injury is a meaningful target for therapy. Evidence suggests that as little as 10% of white matter tract integrity was needed to produce significant recovery of function (refs), thus even small amounts of remyelination may contribute to increase WM integrity to 10% . Ten percent seems like a small amount, but discussion with individuals living with SCI makes it clear that ANY recovery is significant and worth effort.

It is known that oligodendrocytes proliferate after spinal cord injury but the extent to which these new cells contribute to myelination of denuded axons is not known. Without markers to distinguish myelin from new oligodendrocytes from that provided by "old" cells, there has been no way to determine the contribution of the newly born cells. In order to be able to distinguish new from old myelin, Dr. Belegu and colleagues designed and bred a line of transgenic mice. See Awards W81XWH-09-2-0186 (McDonald) and W81X-10-2-0182 (McDonald). These mice were designated MBP_MBP-CTRN_MBP-RFP. Myelin basic protein (MBP) was fused genetically with the reporter molecule citrine (CTRN); thus mature myelinating oligodendrocytes and their myelin will fluoresce green under appropriate illumination. The theory was that when recombination was initiated after SCI and at the start of FES, the DNA for MBP-CTRN will be excised and the MBP-RFP (red fluorescent protein) fusion protein will be expressed in new myelin from mature oligodendrocytes. Old myelin will therefore be green and new myelin will be red. The amount of new red myelin can be assayed and possible enhancement by FES determined by comparing samples from sham animals and FES animals.

Of course any remyelination, whether from old or new oligodendrocytes is important, but the particular goal of this study was to evaluate the birth and contribution of new oligodendrocytes after FES.

In addition to work with transgenic animals, Dr. Belegu attempted to analyze remyelination (from old and new oligodendrocytes) and to microscopically evaluate features of functional myelin from spinal cord samples obtained from sham and FES mice from Aim 1 Experiments 1 and 2 (subacute and chronic SCI and subsequent FES). Samples of cord were fixed and embedded in plastic as for electron microscopy (EM). Semi-thin sections were cut and stained with toluidine blue to evaluate myelin at the light microscopic level by measuring G ratios and evaluating compaction of myelin sheaths surrounding axons cut in cross section. Plans were made to cut ultra-thin sections for similar analysis at the EM level.

Year 1 SA 2 Activities and Accomplishments
1. Most activities for this year focused on breeding and evaluating genotype and cellular and myelin phenotype in the transgenic mice. The goal was to establish a stable colony of homozygous MBP_MBP-CTRN-MBP-RFP mice to be used in SCI/FES experiments.
2. The distribution of the MBP-CTRN fusion protein was examined in uninjured heterozygous MBP_MBP-CTRN_MBP-RFP animals (before removing the neo selection cassette) using immunofluorescence. See Figure 13.
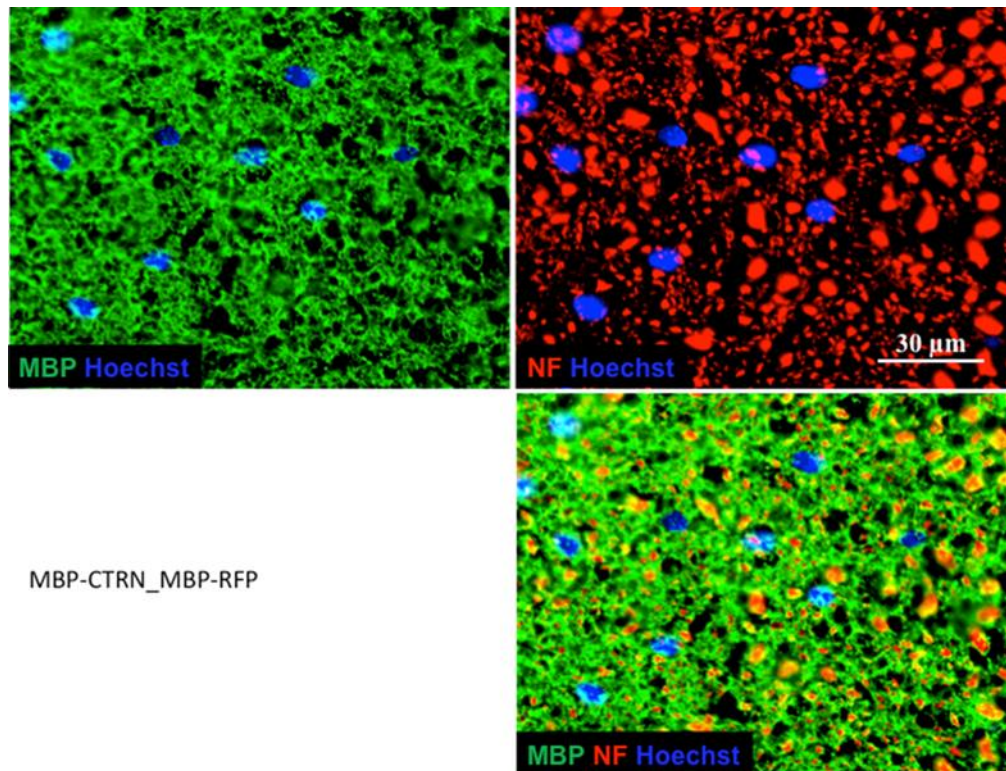
Figure 13. Transgenic MBP-CTRN Fluoresces Green in a Distribution Consistent with that of Wild Type MBP

Expression of the MBP-CTRN fusion protein in the thoracic level of the spinal cord of heterozygote MBP_MBP-CTRN_MBP-RFP mice. Red NF (neurofilament) immunoreactivity labels axons mostly cut in cross-section. Green immunofluorescence shows the distribution of myelin.

3. Breeding:
   a. Heterozygous MBP_MBP-CTRN_MBP-RFP mice were crossed with B6.129S4-Gt(ROSA)26Sortm2(FLP*)Sor/J (FLP*) to remove the neo selection cassette.
   b. Progeny from these matings, heterozygous for MBP_MBP-CTRN_MBP-RFP without the neo cassette were mated in order to obtain homozygous MBP_MBP-CTRN_MBP-RFP mice.

4. Genotyping and Phenotype Analysis (Microscopy and Gait Analysis):
   a. Dr. Belegu contracted with Transnet Inc. to develop qPCR genotyping assays for elements shown in Figure 14 below. Figure 14 also shows that the transgenic MBP portion of the MBP-CTRN fusion protein reacts immunochemically with antibodies to MBP indicating that it was has not been structurally modified during the breeding process. In addition, the MBP and CTRN components of the fusion protein were spatially co-localized as shown in panel C.

MBP (tg)

Citrine (tg)

Normal function as assessed by:
Catwalk, Gridwalk
No BMS
No sensory data

Transnet assay for:
Citrine (het versus hom)
RFP (het versus hom)
MBP endogenous (het versus hom) – non-transgenic element
Neo cassette (het versus hom)
FLPase (het versus hom)
Cre-ER (het versus hom)

+ DAPI

Figure 14. Expression of tgMBP and CTRN in Mouse Spinal Cord

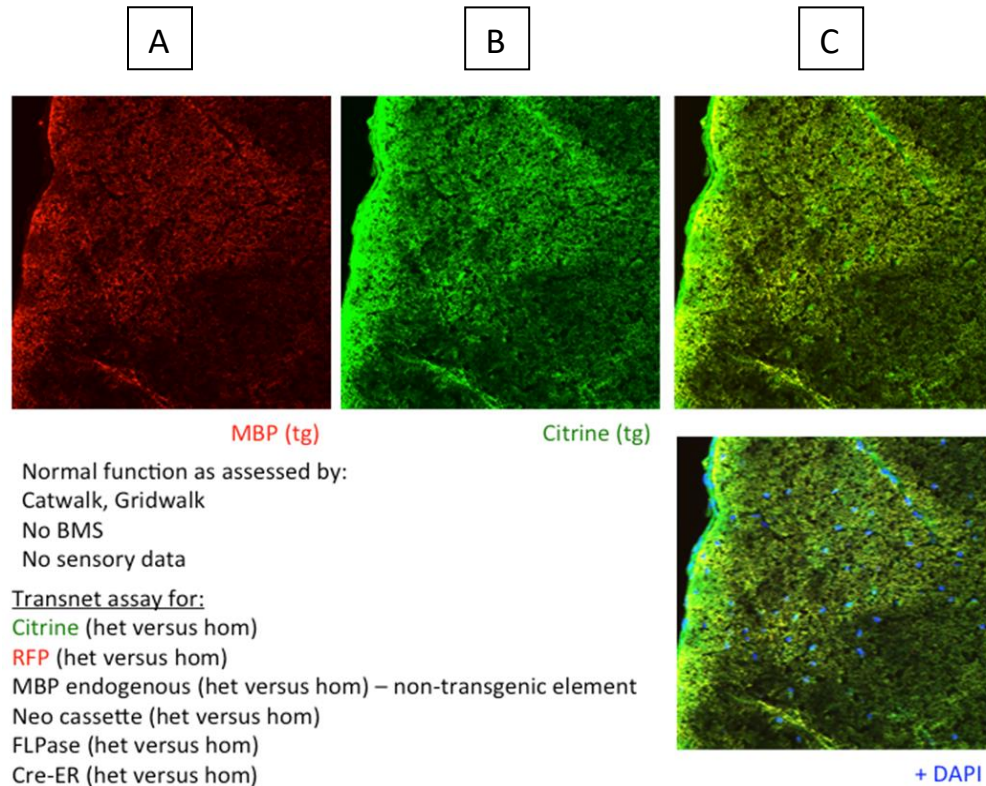Expression of the MBP and citrine in the transgenic mice. At the time of this report the genotype of this animal (heterozygous or homozygous for MBP-CTRN_MBP-RFP) was not known. tg=transgenic

Year 2 SA 2 Activities and Accomplishments
1. Breeding and genotyping:
    a. These activities continued during the early part of Year 2 in the attempt to obtain homozygous MBP_MBP-CTRN_MBP-RFP mice without the neo selection cassette. Unfortunately during the crosses, the transgene was lost and the loss verified by genotyping for CTRN, RFP and neo cassette. New founder mice for the transgene were ordered and bred.
    b. Homozygous mice were obtained during breeding but had a "shiverer" phenotype that developed soon after birth. The animals died in early adulthood. The actual shiverer mutant mouse is well known and has a genetic mutation causing dysmyelination. Myelin is present but not wrapped correctly around the axon causing major dysfunction in neurological function and early death. The shivering phenotype observed in bred mice in this experiment eliminated these mice from use in SCI/FES experiments. The ultrastructural poperties of the homogygous (shivering phenotype) myelin was not determined although samples from the spinal cord and brain were taken from animals perfused for electron microscopy.
    c. Figure 15 below shows that heterozygous mice express CTRN positive green myelin. Genotyping of the heterozygotes showed that they were positive for the RFP gene

and the endogenous MBP gene. But homozygous MBP_MBP-CTRN_RFP transgenic mice with the shivering phenotype were positive for the RFP gene but not the endogenous MBP gene.
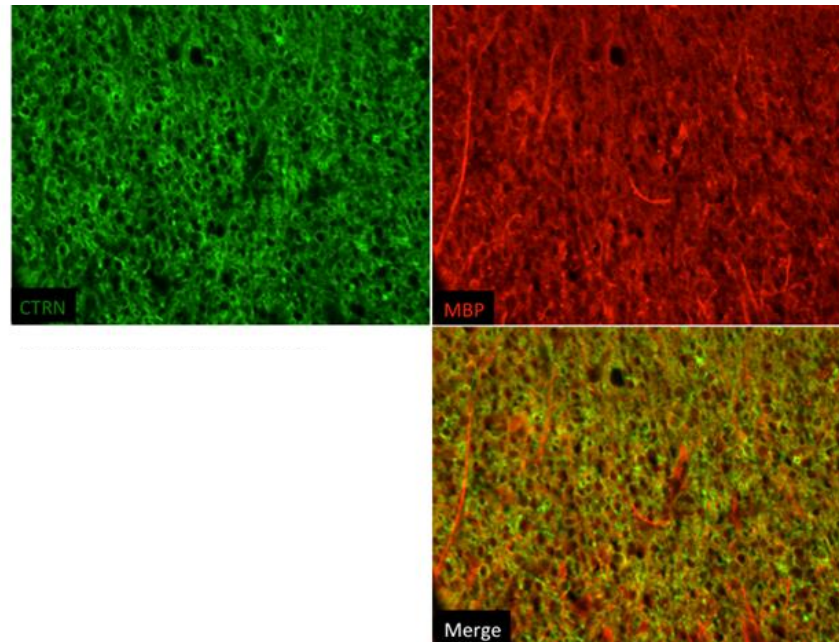

Figure 15. Heterozygous MBP_MBP-CTRN_RFP Transgenic Mice Have (CTRN positive) Myelin

    d. At the end of Year 2, work on the transgenic mice described for SA 2 ceased and efforts were put into analyzing myelin structure in cords from animals in Aim 1 Experiments 1 and 2. All animals in these experiments were given a mild to moderate contusive spinal cord injury and at six days or four weeks after injury and were randomly placed into either the sham group or the FES group. Sham animals were implanted with FES electrodes (See discussion in Aim 1) but were not stimulated. The FES period was four weeks. Some animals from these experiments were perfused with both paraformaldehyde and glutaraldehyde for EM processing and embedding in resin. Samples from the injury epicenter and 1, 3, and 5mm rostral and caudal to it were taken for resin embedding.

2. Myelin Analysis:
    a. Semithin slices (0.5μ and 0.1μ) of the injured thoracic spinal cord were stained with toluidine blue. See Figure 16 below. Examination reveals that the demyelination of the cord in specific tracts (e.g. the corticospinal tract as seen in panel A and bounded by the box) extends up to 5-mm rostral from the injury epicenter. However, even in areas with preserved myelination (panel B), at the 0.5μ thickness the investigators were not able to measure G-ratios reliably. Arrows point to two of many myelinated axons in panel B. In toluidine blue stained sections, axons are pale and unstained and the myelin is stained dark blue. In a normally myelinated axon, the pale axon was surrounded by a close and compactly wound series of myelin sheaths. The G-ratio is calculated as the diameter of the axon alone divided by the diameter of the axon plus myelin. G-ratios in normal mouse tissue are approximately .78 and G-ratios of remyelinated axons are often higher (e.g. .82 in Powers et al, 2015)

indicating thinner myelin after remyelination. Axon thickness in the mouse spinal cord can be <1μ. It is very difficult to obtain reliable measures of diameters and calculate G-ratios in CNS axons even at 100X using light microscopy. EM is usually required and was planned for this project but not completed.
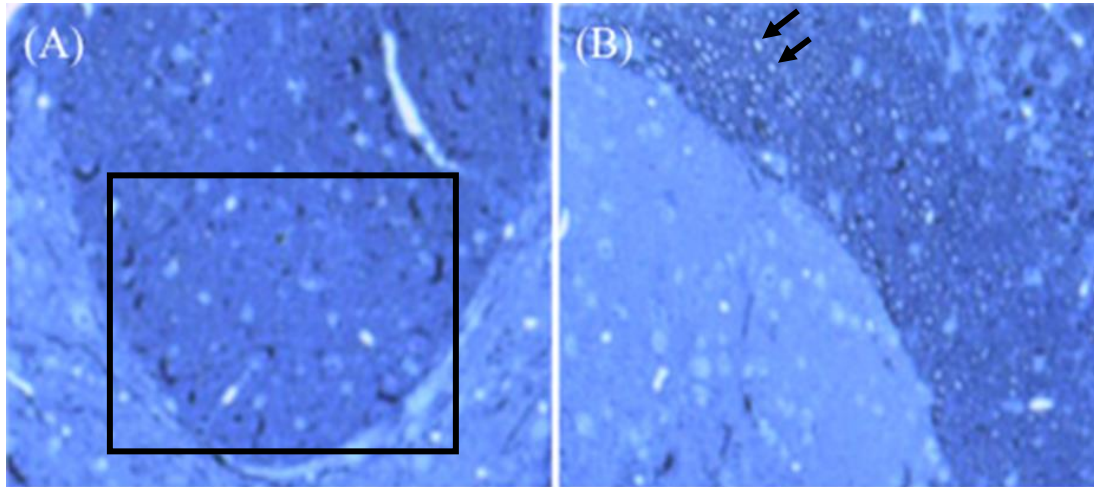
Figure 16. Demyelinated and Myelinated Axons in Toluidine Blue Stained Semi-thin Sections

Summary of Specific Aim 2 Years 1-3
1. Transgenic: Results from work with transgenic mice in this Aim were disappointing. Initial breeding results and myelin analysis from heterozygous MBP_MBP-CTRN-MBP-RFP mice showed normal immunoreactivity and distribution. However, loss of the transgene in the first cohort of mice delayed further work until new mice were obtained. Even more disappointing, mice homozygous for the transgene displayed an abnormal, "shivering" phenotype, making them unsuitable for SCI/FES experiments.
2. Myelin analysis in animals from Aim 1 Experiments 1 and 2. Appropriate samples were collected, embedded, sectioned and stained for light microscopy and G-ratio calculation. However, technical problems with the light microscopy were not conquered and electron microscopy was not done before the end of the period of performance (POP).

<u>Specific Aim 3</u>
Determine if functional electrical stimulation in a mouse model of chronic SCI induces cortical plasticity as measured by resting state functional magnetic resonance imaging (rs-fMRI) (Months 13-24).
<u>Hypothesis:</u> FES will induce cortical plasticity in mice with chronic SCI.

<u>General Comments</u>
Resting state functional magnetic resonance imaging (rs-fMRI) has emerged as an effective tool to examine functional connectivity and plasticity of connections in humans and in animal models of brain injury and SCI. fMRI has traditionally been associated with regional changes in CNS BOLD (blood oxygen level dependent) contrast signal during performance of specific tasks or upon sensory stimulation while in the scanner. But degrees of injury in humans vary considerably from person to person and affect ability to perform tasks or respond to sensory stimulation. Rs-fMRI measures spontaneous fluctuations in BOLD signal **without** task performance. It is likely that rs-fMRI data can be used to monitor effects of therapeutic interventions such as FES on CNS function. It offers the advantage that one scanning protocol and analysis approach can be used for many individuals regardless of ability to perform tasks. This imaging approach has both research and clinical promise.

Performing MRI scanning on a mouse, especially a SCI mouse is challenging. They are small animals; anesthesia and handling are difficult especially when working with compromised animals. But as said earlier in this report, mice are becoming the rodent of choice for CNS disease and injury experiments. The work described for SA 3 proposed to 1) establish scanning and analysis protocols for rs-fMRI in anesthetized, injured mice and 2) correlate changes in and between network functional connectivity (BNC) during recovery from injury with or without application of FES.

<u>Year 1 SA 3 Activities and Accomplishments</u>
1. Animal Protocol:
   a. As expected, Dr. Belegu and his associates spent the first year, preparing and submitting animal protocols in effort to gain approval from three research animal care and use committees: 1) The High-Field Preclinical MRI Facility of the F.M. Kirby Research Center (Kirby Center) located at Kennedy Krieger Institute 2) The Johns Hopkins University Animal Care and Use Committee and 3) ACURO
   b. At the end of Year 1, the Kirby Center approved data acquisition sequences (scanning protocol) and data analysis methods specifically whole brain seed correlation analysis and interhemispheric FC (functional connectivity) evaluated with a pairwise seed analysis. The investigators were advised to add metetomidine to the anesthesia protocol.

<u>Year 2 SA 3 Activities and Accomplishments</u>
1. Animal protocols continued to move through the three tier approval process (see Year 1)

<u>Year 3 SA 3 Activities and Accomplishments</u>
1. Upon advice from colleagues in the Kirby Center, Dr. Belegu began discussions with the FES electrode manufacturer (PlasticOne Inc) on customizing paramagnetic electrodes (made with silver instead of stainless steel) for use in the MR scanner. Late in Year 3, Dr. Belegu was able to obtain the silver MRI compatible electrodes.

2. Final modifications were made to the animal protocol and submitted for approval. Highlights from the modified animal protocol are included here.

"Mice will be initially anesthetized within a transparent anesthetic induction-chamber (Stoelting Co., Illinois, USA)] with isoflurane (2%) delivered from a precision vaporizer in oxygen-enriched air, monitored visually until respiration slows, and the righting reflex disappears in about 90 seconds. Mice will receive an i.p. injection of 0.005-0.01 mg/kg dexmedetomidine (Zoetis). Mice will then be placed into an MRI compatible holder, secured with bite bar and ear bars. A custom-made nose cone will be used to deliver isoflurane mixed in oxygen-enriched air. Exhaled gas from the animals will be actively vacuumed away from the nose cone via a building vacuum line. The flow rate of the vacuum line will be maintained at the same level across animals and will be monitored. A continuous infusion of medetomidine (0.005-0.01 mg/kg/hr, SC) will be started through a syringe needle tipped infusion line that will be secured to the dorsal back skin with a single suture. Isoflurane concentration will gradually be reduced to 0.5% and will be maintained at this level for the duration of the scans.

During the MRI scans, multiple parameters will be monitored to ensure stable physiological state and adequate depth of anesthesia. Rectal temperature will be monitored, and animals will be maintained at 37 ± 1°C body temperature by a temperature-controlled water-heating pad. Continuous, dynamic, noninvasive measurements of arterial blood oxygen saturation level and heart rate (MouseOx Pulse Oximeter, STARR Life Sciences Corp, Oakmont, PA) and respiration rate (Small Animal Monitoring and Gating System, SA Instruments, Inc., NY) will be monitored. Oxygen concentration in the anesthetic gas mixture can be increased to maintain oxygenation saturation level to above 95%. Under the dexmedetomidine infusion/low isoflurane concentration anesthetic regime, mouse normal respiration rate is approximately 90-100 breaths per minute, and heart rate is about 340-370 beats per minute. If the cardiac rate rises to ~380 beats/min and/or respiration rate rises to 100 breaths/min, isoflurane concentration will be increased slightly to deepen anesthesia accordingly. The goal will be to maintain an optimum dose regime so that we can detect resting state fMRI signal and brain network activity in these anesthetized animals.

At the end of each fMRI scan, topical Marcaine will be applied to where infusion needle was inserted. The ear bar and mouth bar will be removed from the animal while the animal remains on the heating pad. Atipamezole (0.1 mg/kg, IP) will be injected to antagonize the effect of dexmedetomidine. The animal typically will fully recover from anesthesia within 5-10 minutes and can then be returned to its home cage and the housing room."

Summary Aim 3 Years 1-3
Unfortunately, no fMRI data was collected from SCI/FES mice during the POP. Final regulatory approvals were not received until close to the end of the Award.

References
Becker D, Gary DS, Rosenzweig ES, Grill WM, McDonald JW. Functional Electrical Stimulation Helps Replenish Progenitor Cells in the Injured Spinal Cord of Adult Rats. Exp Neurol (2010) 222:211-218. PMCID: PMC2834811

Tatem KS, Quinn JL, Phadke A, Yu Q, Gordish-Dressman H, Nagaraju K. Behavioral and Locomotor Measurements Using an Open Field Activity Monitoring System for Skeletal Muscle Diseases. J Vis Exp (2014) 91:51785. PMCID: PMCC4672952

Powers BE, Sellers DL, Lovelett EA, Cheung W, Aalami S, Zapertov N, Maris DO. Remyelination reporter reveals prolonged refinement of spontaneously regenerated myelin. PNAS (2013) 110:4075-4080. PMCID: PMC3593891.

What opportunities for training and professional development has the project provided?
Nothing to report.

How were the results disseminated to communities of interest?
Nothing to Report.

What do you plan to do during the next reporting period to accomplish the goals?
Nothing to report. The period of performance has ended.

IMPACT

What was the impact on the development of the principal discipline(s) of the project?
FES is a clinical intervention in patients with SCI and myelination disorders such as multiple sclerosis. The mechanisms through which FES generates neurological recovery remain unclear. Development of a model for induction of FES in mice will shed light into such mechanisms. Our methodology is similar to what is used in the clinic to treat SCI patients. While we have focused on remyelination as a possible mechanism for such recovery other mechanisms could play a role.

The PI and his colleagues developed a reliable mouse model of moderate contusion SCI and subsequent FES. They showed that FES induces proliferation of cells including mature oligodendrocytes in and near the injury epicenter. In addition, FES was shown to improve motor function, both gross and fine in a chronic model of mouse SCI

What was the impact on other disciplines?
The methods and aims presented here are applicable to any disorder that can be altered through activity-based interventions.

What was the impact on technology transfer?
Nothing to report.

What was the impact on society beyond science and technology?
FES has shown to alter the life of SCI patients by enabling them to be involved in activities that promote neurological recovery and mental well-being. We hope that our work will continue to inspire SCI patients to maintain an active lifestyle.

CHANGES/PROBLEMS

Changes in approach and reasons for change.
Nothing to report.

Actual or anticipated problems or delays and actions or plans to resolve them
The problems we have faced during this project have been technical in nature. We are yet to complete the G-ratio analysis, which is currently being done in thinner semithin spinal cord

slices. A complete electron microscope analysis was initiated but not completed in the brains of mice that were treated with FES after SCI as well as MBP_MBP-CTRN_RFP transgenic mice. Completion of Specific Aim 3, resting-state fMRI analysis was not completed due to problems with physiological stabilization of injured, anesthetized animals.

Changes that had a significant impact on expenditures.
We previously requested and reported purchasing a high-speed camera for calcium imaging and added the camera to an inverted Olympus fluorescent microscope. But, the cost of this equipment was allocated to Institute funds instead of the grant. Additionally, the Neurolucida microscopic image analysis software and the required motorized microscope stage were not purchased.

Significant changes in use or care of human subjects, vertebrate animals, biohazards, and/or select agents.
Nothing to report.

Significant changes in use or care of human subjects.
Nothing to report.

Significant changes in use or care of vertebrate animals.
Nothing to report.

Significant changes in use of biohazards and/or select agents.
Nothing to report.

PRODUCTS

Publications, conference papers, and presentations.
Nothing to report.

Journal publications.
Li Q, Houdayer T, Liu S, **Belegu V**. Induced neural activity promotes an oligodendroglia regenerative response in the injured spinal cord and improves motor function after spinal cord injury. J Neurotrauma. 2017 Dec 15; 34(24):3351-61. PMID: 28474539
Acknowledgement of federal support? – Yes
The experiments reported in this publication were done in rats.

Choe AS, Sadowsky CL, Smith SA, van Zijl PCM, Pekar JJ, **Belegu V**. Subject-specific regional measures of water diffusion are associated with impairment in chronic spinal cord injury. Neuroradiology. 2017 Aug; 59(8):747-758. PMID: 28597208
Acknowledgment of federal support? – Yes

Pan B, Ao H, Liu S, Xu Y, McDonald JW, **Belegu V**. Spinal cord organogenesis model reveals role of Flk1+ cells in self-organization of neural progenitor cells into complex spinal cord tissue. Submitted to: Stem Cell Research in 2017

Choe AS, Jones CK, Joel SE, Muschelli J, Belegu V, Caffo BS, Lindquist MA, van Zijl PC, Pekar JJ. Reproducibility and Temporal Structure in Weekly Resting-State fMRI over a Period of 3.5 Years. PLoS One. 2015 Oct; 10(10):e0140134. PMID: 26517540
Acknowledgement of federal support? – Yes

Books or other non-periodical, one-time publications.
Nothing to report.

Other publications, conference papers, and presentations.
Nothing to report.

Website(s) or other Internet site(s)
Nothing to report.

Technologies or techniques.
Nothing to report.

Inventions, patent applications, and/or licenses.
Nothing to report.

Other Products.
To date we have generated transgenic mouse lines that promise to be transformative in the study of oligodendrocytes and myelination during development and in various pathologies that are pertinent to the healthcare of military personnel.

PARTICIPANTS & OTHER COLLABORATING ORGANIZATIONS

What individuals have worked on the project?

Name:	Visar Belegu, PhD
Project Role:	PI
Researcher Identifier (e.g. ORCID ID):	NA
Nearest person month worked:	10.2
Contribution to Project:	Dr. Belegu has supervised all the work performed in this project. In addition, Dr. Belegu has performed SCI surgeries, electrode implantations, FES stimulation, and neurological assays. Dr. Belegu has also performed MRI imaging for Specific Aim 3.

Name:	Su Liu, PhD
Project Role:	Key Personnel
Researcher Identifier (e.g. ORCID ID):	NA
Nearest person month worked:	10.2
Contribution to Project:	Dr. Liu has assisted Dr. Belegu in performing SCI surgeries, electrode implantation. In addition, she has performed the electrical stimulations, perfusions, staining for animals in Specific Aim 1 and 2. She has also performed electrical stimulation for animals in Specific Aim 3.

Has there been a change in the active other support of the PD/PI(s) or senior/key personnel since the last reporting period?
Nothing to report.

What other organizations were involved as partners?
Nothing to report.

SPECIAL REPORTING REQUIREMENTS

Quad Chart on following page

Advanced Restoration Therapies in Spinal Cord Injury

13211006
W81XWH-14-1-0069

PI: Visar Belegu, PhD   **Org:** Hugo W. Moser Research Institute at Kennedy Krieger, Inc.   **Award Amount:** $1,998,495.11

Study/Product Aim(s)

• SPECIFIC AIM 1: Determine if functional electrical stimulation (FES) in a mouse model of chronic spinal cord injury (SCI) induces proliferation and differentiation of genetically labeled oligodendrocyte progenitor cells (OPCs)
• SPECIFIC AIM 2: Determine if FES induces remyelination by mature oligodendrocytes in a mouse model of chronic SCI
• SPECIFIC AIM 3: Determine if FES in a mouse model of chronic SCI induces cortical plasticity as measured by resting state functional magnetic resonance imaging (rs-fMRI)

Approach

We aim to investigate the role of functional electrical stimulation in generating neurological recovery following spinal cord injury. Specifically, we will use transgenic mice to investigate if such an effect is mediated through cells of the oligodendrocyte lineage.
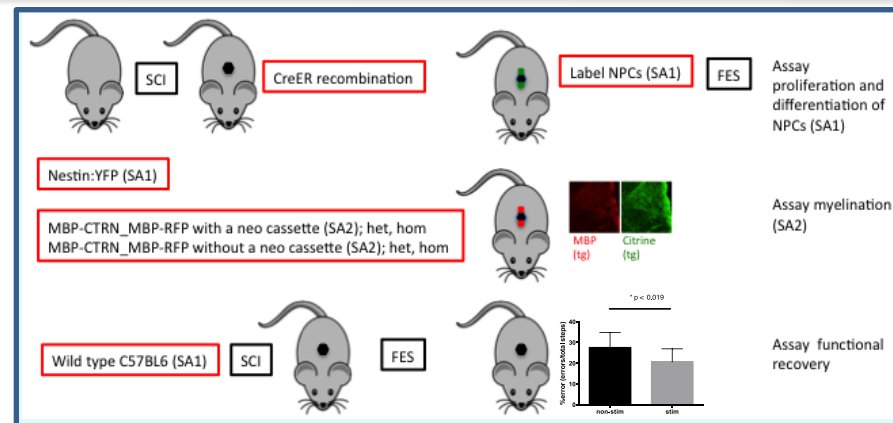
Accomplishments: (1) FES elicits a mitogenic response in subchronic stages of SCI. (2) FES induces a complex motor function recovery in subchronic and chronic stages of SCI. (3) FES increases number of oligodendrocytes in chronic stages of SCI.

Timeline and Cost

Activities	Year	1	2	3
Determine if FES induces proliferation & differentiation of OPCs		▓▓▓	▓▓▓	
Determine if FES induces remyelination by mature oligodentrocytes		▓▓▓	▓▓▓	
Determine if FES induces cortical plasticity				▓▓▓
Estimated Budget ($K)		$639K	$782.7K	$576.8K

Updated: 05/13/2018

Goals/Milestones

Y1 Goals – System demonstration
☑ Obtain regulatory approval for animal work from Johns Hopkins IACUC and USAMRMC ACURO.
☑ Initiate generation of transgenic animals.
☑ Initiate and completed SCI, and FES implantation, and electrical stimulation for two sets of experiments.
☑ Develop task-activated fMRI sequences and data processing pipeline.

Y2 Goals – System validation
☑ Complete the analysis on the effects of FES in proliferation and differentiation of spinal cord progenitor stem cells.
☐ Complete the analysis on the effects of FES in myelination.
☑ Complete the analysis on the effects of FES in neurological recovery.

Comments/Challenges/Issues/Concerns
Technical issues delayed the analysis on myelination **Budget Expenditure to Date**
Projected Expenditure: $1,998,495.11
Actual Expenditure: $1,998,495.00

<u>APPENDICES</u>

Induced Neural Activity Promotes an Oligodendroglia Regenerative Response in the Injured Spinal Cord and Improves Motor Function after Spinal Cord Injury

Qun Li,[1] Thierry Houdayer,[1] Su Liu,[1] and Visar Belegu[1–3]

Abstract

Myelination in the central nervous system (CNS) is a dynamic process that includes birth of oligodendrocyte progenitor cells (OPCs), their differentiation into oligodendrocytes, and ensheathment of axons. Regulation of myelination by neuronal activity has emerged as a new mechanism of CNS plasticity. Activity-dependent myelination has been shown to regulate sensory, motor, and cognitive functions. In this work, we aimed to employ this mechanism of CNS plasticity by utilizing induced neuronal activity to promote remyelination and functional recovery in a subchronic model of spinal cord injury (SCI). We used a mild contusive SCI at T10, which demyelinates surviving axons of the dorsal corticospinal tract (dCST), to investigate the effects of induced neuronal activity on oligodendrogenesis, remyelination, and motor function after SCI. Neuronal activity was induced through epidural electrodes that were implanted over the primary motor (M1) cortex. Induced neuronal activity increased the number of proliferating OPCs. Additionally, induced neuronal activity in the subchronic stages of SCI increased the number of oligodendrocytes, and enhanced myelin basic protein (MBP) expression and myelin sheath formation in dCST. The oligodendroglia regenerative response could have been mediated by axon-OPC synapses, the number of which increased after induced neuronal activity. Further, M1-induced neuronal activation promoted recovery of hindlimb motor function after SCI. Our work is a proof of principle demonstration that epidural electrical stimulation as a mode of inducing neuronal activity throughout white matter tracts of the CNS could be used to promote remyelination and functional recovery after CNS injuries and demyelination disorders.

Keywords: axon-OPC synapse; induced neuronal activation; motor function; remyelination; SCI

Introduction

MYELIN SHEATHS are formed by oligodendrocytes, and enable fast propagation of action potentials in the mammalian central nervous system (CNS). Proper myelination is necessary for integrated motor and sensory function as well as behavior and cognitive function. Myelination is a dynamic process in which oligodendrocyte progenitor cells (OPCs) proliferate and differentiate, continuously remodeling myelin.[1] Endogenous neuronal activity-dependent remodeling of myelin in the adult CNS is emerging as a new mechanism of CNS plasticity.[2] Dependency of OPC proliferation on neuronal electrical activity was first shown in the optic nerve.[3] Elegant studies that genetically block generation of new oligodendrocytes without effecting preexisting oligodendrocytes or myelin showed that neuronal-activity-dependent generation of new oligodendrocytes and myelin remodeling is important for learning motor skills,[4] whereas, lack of activity induced by social isolation impaired myelination in the prefrontal

cortex.[5] Remyelination in multiple sclerosis-like lesions is also dependent on neuronal activity. In ethidium bromide (EB) induced demyelination lesions, blocking of neuronal activity reduces levels of remyelination where the number of OPCs is increased while the number of oligodendrocytes is decreased.[6] In these lesions, neuronal activity regulates remyelination partially through neuronal glutamate vesicular release, and α-amino-3-hydroxy-5-methyl-4-isoxazolepropionic acid (AMPA) receptors in OPCs. However, the potential clinical benefits of neuronal activity-dependent remyelination have not been reached.

In the injured spinal cord, demyelination occurs as a result of oligodendrocyte death.[7] Spontaneous remyelination occurs even in chronic stages of spinal cord injury (SCI),[8] but it is insufficient to prevent long-term neurological disability. Therefore, augmenting the intrinsic remyelination response remains an important therapeutic direction for treatment of SCI and other myelin-related disorders.[9] Augmentation of oligodendrogenesis that leads to myelin remodeling by modulation of neuronal activity, where neuronal

---

[1]The International Center for Spinal Cord Injury, Hugo W. Moser Research Institute at Kennedy Krieger, Baltimore, Maryland.
[2]Department of Neurology, [3]Department of Pathology, Johns Hopkins University School of Medicine, Baltimore, Maryland.

Page | 29

activation was induced through electrical stimulation, was first shown in an *in vitro* model.[10] Induction of activity through electrical stimulation of the medullary pyramid increased oligodendrogenesis in the dorsal corticospinal tract (dCST) throughout the spinal cord.[11] In addition, optogenentic activation of M2 layer V projection neurons promoted oligodendrogenesis and remodeled myelin in subcortical white matter tracts; moreover, this mode of induced activation was accompanied by changes in motor function.[12]

Here, we induced neuronal activity through electrical stimulation of the M1 cortex after a mild thoracic contusion SCI that spared but demyelinated dCST axons. We show that induced neuronal activation in subchronic SCI promotes oligodendrogenesis and remyelination, and generates motor function recovery. We provide a novel strategy for promoting remyelination in CNS injury and other demyelination disorders.

Methods

Animals and experimental timeline

Twenty-seven female Sprague–Dawley rats (250 ± 25 g) were used. The Johns Hopkins University Institutional Animal Care and Use Committee approved all the procedures performed in this study. Twenty-four animals were divided into stimulated and sham-stimulated cohorts ($n = 12$ per cohort). Three additional rats were used to confirm the severity of the mild SCI model, primarily showing that it causes demyelination in the injury epicenter while preserving dCST axons (one was naïve; one underwent an SCI; one underwent an SCI and received an injection of biotinylated dextran amine [BDA]). Day 0 denotes the day that animals received the SCI. On day 28, BDA was injected into the M1 cortex, and electrodes were implanted over the same region. Electrical stimulation was performed daily starting on day 28 and continued until the experimental end-point on day 49. On days 42–49, 5-bromo-2'-deoxyuridine (BrdU, Roche) was administered daily. All animals were euthanized at day 49 (Fig. 1).

Mild contusive SCI

Animals were anesthetized with ketamine/medetomidine cocktail (75:0.5 mg/kg), and a dorsal laminectomy was performed. A midline incision was made, and the paravertebral muscles were dissected to expose the spinal column at the level of T9–T11. Clamping the T9 and T11 spinous processes stabilized vertebral column. The T10 dorsal lamina was then removed. The dorsal surface of the spinal cord at T10 with intact dura was exposed, and hit with a 40 kdyn force using an Infinite Horizon Impactor (Precision System). Following the impact, muscles were sutured, and the skin was stapled. Animals received intramuscular (i.m.) injections of 0.5 mL atipamezole (Antisedan, Pfizer), and were kept in a 37°C incubator until they recovered from anesthesia. Subsequently,

animals were hydrated through subcutaneous (s.c.) injections of 10 mL saline, and were administered 0.12 mg/kg Enrofloxacin (Baytril, Bayer) i.m. for 3 consecutive days. Bladders of the rats were expressed manually three times daily until reflex bladder emptying was established, which occurred the following day.

Anterograde tracing of CST

On day 28, anterograde tracer BDA (Molecular Probes) was injected into the cortex to label the CST. Briefly, animals were anesthetized again as described, and the head was fixed in a stereotactic frame (Kopf Instruments). Unilateral craniotomy was performed over the hindlimb representative area of the M1 cortex, and the intact dura was exposed. The glass pipette (tip diameter: 20 μm) containing 5 μL 10% BDA in saline was lowered from the surface of the dura to a depth of 1 mm (cortical layer V). BDA was iontophoresed for 20 min (7 sec on, 7 sec off; 5 μA). Four injections were made within the lateral portion of the hindlimb representation. After injections were completed, we waited for 2 min before removing the pipette.

Electrode implantation and electrical stimulation

Immediately after BDA injection, animals received electrode implantation as previously described.[13] Two 127 μm diameter stainless steel electrodes (MS333/1-A, Plastics One) were bent into an "L" shape, and the deinsulated bottom of the "L" was placed over the dura of the hindlimb representative and the BDA injection area (1.5 mm apart). To confirm proper placement of the electrodes, we stimulated the M1 cortex to provoke a motor response in the contralateral hindlimb. A constant current stimulator (Neopraxis) was used to deliver trains of stimuli (190 msec on, 1500 msec off; 1.0–1.5 mA; 200 Hz). Once proper placement of electrodes was confirmed, electrodes were secured with dental acrylic cement supported by three microscrews (Small Parts). The skin on the head was subsequently sutured.

Staring on day 28, animals were stimulated for 4 h daily for 3 weeks (Fig. 1). The connector on the head of the animals that contained the implanted electrode was attached to a commutator (Plastics One) mounted to the top of the cage, and trains of stimuli (described previously) were applied, to provoke a motor response limited to the hindlimb that was contralateral to stimulation. Animals were able to eat, drink, and walk during the stimulation. Animals did not paw at their heads or show signs of pain or distress. On the days when both behavior testing and stimulation were performed, behavior testing was done first. Sham-stimulated animals received electrode implantation only but were not stimulated.

BrdU administration

BrdU was dissolved in saline (0.1M) with a brief ultrasonic treatment at 37°C. During days 42–49, BrdU was administered
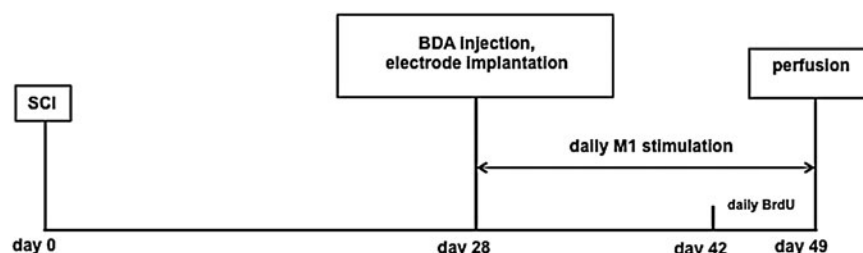
FIG. 1. Experimental timeline. Animals received mild contusive spinal cord injury (SCI) on day 0. Biotinylated dextran amine (BDA) was injected unilaterally in the M1 cortex, and electrodes were implanted over M1 on day 28. Electrical stimulation was performed for 4 h daily from day 28 to day 49. During the last week of stimulation (days 42–49), 5-bromo-2'-deoxyuridine (BrdU) (50 mg/kg) was administered intraperitonally (i.p.) daily. All animals were euthanized at day 49.

through intraperitoneal (i.p.) injections at a 50 mg/kg concentration. The last injection was administered on day 49, 3 h before the animals were perfused (Fig. 1).

Tissue processing, epon embedding, and anatomical staining

Three animals were perfused with 2%-glutaraldehyde and 2%-paraformaldehyde in phosphate buffered saline (PBS) on day 49. Spinal cords were dissected, and 1 mm blocks at T10 (injury epicenter, the black segment in Fig. 2) from the naïve (Fig. 3A,B) and SCI only (Fig. 3 C,D) animals were cut, and post-fixed overnight in the same fixation solution. The blocks were exposed to 1% OsO4 for 1 h, stained in 0.5% uranyl acetate overnight, and dehydrated in a series of alcohols (15 min each) followed by propylene oxide for 3 h. After being infiltrated with a 1:1 mixture of propylene oxide and EMBed-812 embedding resin (Electron Microscopy Sciences) for 3 h, the blocks were embedded with same resin at 60°C overnight. Transverse semi-thin sections were cut on a microtome at 1 μm thickness and stained with 1% Toluidine blue. The semi-thin sections were analyzed with a light microscope (Zeiss ApoTome) (Fig. 3A–D).

The animal that received both SCI and BDA injections (Fig. 3F, G) underwent the same procedures for perfusion, post-fixation, and dissection as described. However, here, the 1 mm block from the injury epicenter at T10 (Fig. 2) was first sectioned at 60 μm using a vibratome. Sections were incubated in 1% avidin-biotin complex (ABC) reagent (Vector Laboratories) for 1 h at room temperature. After rinsing twice in PBS, the tissue was incubated with the chromogen (diaminobenzidine [DAB]) for 6–10 min in: 1 DAB tablet (10 mg; Sigma) plus 0.01% H_2O_2 in 15 mL PBS. After the dehydration and osmium fixation procedures, sections were flat-embedded in EMBed-812 resin between two sheets of Aclar in 60°C overnight. The plastic sections were dissected, and the area of dCST was trimmed and affixed on blank beam capsules. Tissue was further micro-sectioned in 0.5 μm slices, and stained with toluidine blue (Fig. 3F). L2 spinal cord tissue caudal from the injury epicenter (shadowed segment in Fig. 2) from the same animal was freeze-sectioned at 40 μm, stained with Cy2-streptavidin, and imaged with an Olympus BX61 fluorescence microscope (Fig. 3G).

Immunohistochemistry (IHC)

Twelve experimental animals (six stimulated and six sham-stimulated) were used for IHC. On day 49, animals were perfused with 4% paraformaldehyde in 0.1M PBS, and spinal cords were dissected. For each animal we cut six blocks of 1 mm long spinal cord tissue; specifically, these blocks were cut 3 mm, 6 mm, and 9 mm rostral from the injury epicenter, and 3 mm, 6 mm, and 9 mm caudal from injury epicenter (gray segments in Fig. 2). Blocks were post-fixed at 4°C overnight, then transferred into 20% sucrose solution until the tissue sank to bottom of the vials. The spinal cords were freeze-cut transversely in 40 μm sections. For each spinal cord block (1 mm in length), ∼24–25 sections were collected and they were divided into four groups (usually six sections/group) in a rotating order. These four groups of tissue sections were immunostained for: (1) neural/glial antigen (NG2)/BrdU/BDA; (2) APC-CC1/BDA; (3) MBP/neurofilament (NF); and (4) NG2/synaptophysin/BDA. For BrdU staining, sections were pretreated with 2N HCl to denature DNA (37°C; 45 min), and with two 15 min borate buffer treatments (pH 8.5) to neutralize the HCl. Following blocking for 60 min in 10% normal goat serum (NGS) and 0.1% triton X-100 in PBS, sections were incubated in primary antibodies at 4°C for 48 h. Primary antibodies used in this study were: mouse anti-BrdU (1:600; Serotec), rabbit anti-NG2 (1:200; Chemicon), mouse anti-APC-CC1 (1:400; Oncogene), rabbit anti-MBP (1:1000; Millipore), mouse anti-NF (1:1000; Abcam), and mouse anti-synaptophysin (1:400; Chemicon). After three 10 min washes in PBS, sections were incubated with the following secondary antibodies: Alexa 488 conjugated goat anti-rabbit IgG (1:200; Life technologies) and Cy3 conjugated goat anti-mouse IgG (1:200; Jackson labs) or Alexa 488-goat anti-mouse IgG (1:200; Life technologies) at room temperature for 2 h. Cy3- or Cy5-conjugated streptavidin (1:1000: Jackson labs) was mixed with secondary antibodies to stain BDA-labeled CST axons. Sections were mounted onto slides, air-dried, cover-slipped, and observed with an Olympus BX61fluorescence microscope.[11]

Cell counting

BrdU$^+$/NG2$^+$ and APC-CC1$^+$ cells within the dCST area were counted using ImageJ. The criteria for counting proliferating OPCs were for a cell to have BrdU$^+$ nuclei and NG2$^+$ cytoplasm (Fig. 4B,

Injury Epicenter - T10

1 mm

Rostral

Caudal

R-9mm R-6mm R-3mm   C-3mm C-6mm C-9mm   L2

■ - Injury epicenter; labeling of myelin (toluidine blue), and BDA$^+$ axons

▒ - L2 spinal cord; labeling of BDA$^+$ axons

▓ - Rostral and caudal segments; labeling of cells from the oligodendrocyte lineage and BDA$^+$ axons
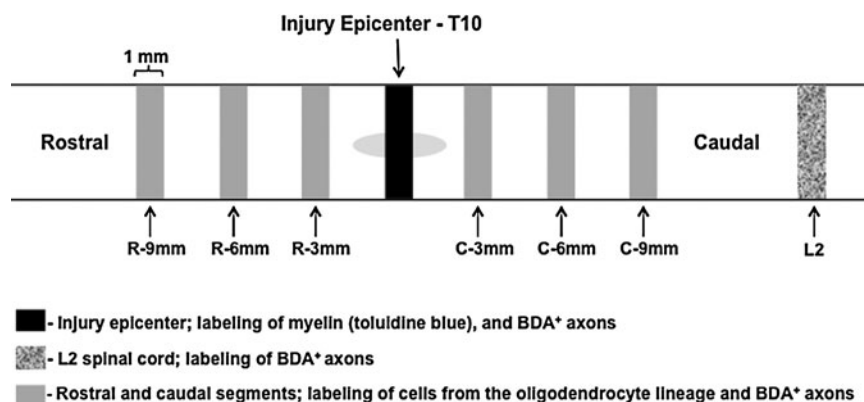
FIG. 2. Schematic diagram of tissue sampling. After perfusion at day 49, spinal cords were dissected and cut into 1 mm segments for morphological analysis. In three animals (naïve; spinal cord injury [SCI] only; SCI and biotinylated dextran amine [BDA] injection), tissue from the epicenter of the lesion (T10) was processed for epon embedding and stained with Toluidine blue (black segment; for sample images see Fig. 3A–F). A 1 mm segment at L2 from the animal that received SCI and BDA injection was further cut into 40 μm sections and stained with Cy2-streptavidin to detect BDA-labeled dorsal corticospinal tract (dCST) axons (shadowed segment; for sample images see Fig. 3G). For the experimental animals (six stimulated and six sham animals), 1 mm segments located 3 mm, 6 mm, and 9 mm rostral and caudal from the lesion epicenter were further cut into 40 μm sections and immunostained (gray segments).
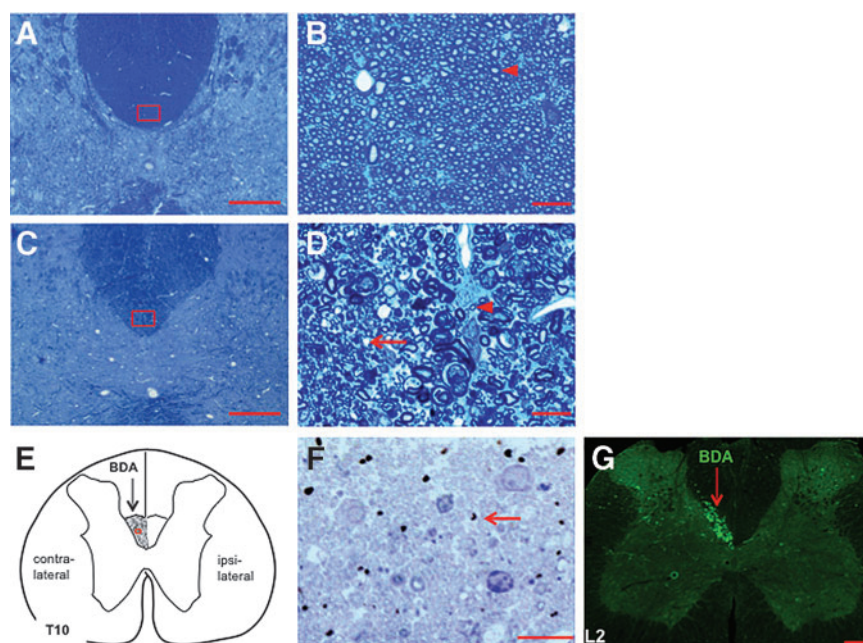
FIG. 3. Mild contusion at T10 causes demyelination of surviving axons in the dorsal corticospinal tract (dCST) of injured spinal cord. **(A)** Low power image from a 1 μm Toluidine blue stained T10 spinal cord section in a naïve animal showing the gray–white matter border in the dorsal spinal cord (red box indicated the area of the dCST imaged in panel B). **(B)** High power image from within the dCST at T10 in the spinal cord of a naïve animal showing normal myelin (red arrowhead points to a normal myelin sheath within the dCST at T10). **(C)** Low power image from a 1 μm toluidine blue stained T10 spinal cord section in an animal that received a mild spinal cord injury (SCI). The mild SCI does not create a contusive cyst at the injury epicenter nor does it perturb the gray–white matter border; in addition, no glial scar creating a border between the injured and uninjured areas was seen in low power images (red box indicates the area of the dCST imaged in panel D. **(D)** High power image from within the dCST at T10 in the spinal cord in an animal that received a mild SCI. In the subchronic stage of mild SCI, many myelin sheaths became swollen and degenerate, resulting in partial demyelination within the dCST (red arrow indicates a demyelinated axon whereas the red arrowhead indicates a spared myelin sheath). **(E)** Diagram of the spinal cord at T10. Shadowed area is the dCST. Red box indicates area imaged in panel F. **(F)** Image from a semithin (0.5 μm) T10 spinal cord section of an animal that received SCI and biotinylated dextran amine (BDA) injections. The section was reacted with avidin-biotin complex (ABC)-diaminobenzidine (DAB) and counterstained with Toluidine blue. Surviving demyelinated axons are labeled within the dCST (brown-colored granules; arrow) at SCI epicenter. **(G)** Cy2-streptavidin-stained L2 section (40 μm) from the same animal imaged in panel F. BDA+ axons (arrow) indicate that despite the demyelination at the SCI epicenter, the majority of dCST axons caudal from the SCI survived. Scale bar in panels **A, C,** and **G** is 200 μm; in panels **B, D,** and **F** it is 10 μm.

C). Mature oligodendrocytes were counted for cells that had APC-CC1-labeled cell bodies (Fig. 5B,C). Images of the dCST area from all the immunostained transverse sections were taken at 40× magnification on an Olympus BX61 fluorescence microscope. Images were opened and initialized in ImageJ. The dCST was outlined using the "Freehand Selection" tool. The contralateral dCST was identified by the presence of BDA-labeled axons, whereas the symmetric area across the midline was identified as the ipsilateral dCST (Figs. 4A and 5A). The "Cell Counter" tool was then used to count each immune-labeled cell, with which each counted cell is marked preventing the same cell from being counted twice. The program recorded the number of counted cells for each section automatically. In each 1 mm spinal cord segment the total number of labeled cells from six 40 μm sections were added and divided by 6 (the number of sections per each segment). In Figure 4, because of the low number of proliferating OPCs within the dCST in one section, we averaged the number of BrdU+/NG2+ cells from all six 1 mm spinal cord segments. The average number of BrdU+/NG2+ cells within dCST per 40 μm section ± SEM was compared for four groups as described under *Data analysis and statistics* (Fig. 4D). In Figure 5, because the number of labeled oligodendrocytes was higher, in addition to comparing the average number of labeled oligodendrocytes in all six, 1 mm spinal cord segments for four experimental groups (Fig. 5D), we compared the average number of labeled oligodendrocytes within the contralateral dCST per 40 μm section ± SEM in the rostral (R-3mm, R-6mm, and R-

9mm) versus caudal (C-3mm, C-6mm, and C-9mm) segments of the spinal cords. (Fig. 5E).

Western blotting

Twelve animals (n = 6 per group) were quickly perfused with cold saline on day 49. A 10 mm long spinal cord section centered at the injury epicenter (R-5-mm to C-5-mm) was removed, and put on dry ice. Spinal cord tissue was separated along the midline into the ipsilateral half and the contralateral half. Each half was cut into the ventral and dorsal part. The dorsal spinal cord tissue was then lysed in RIPA buffer (Sigma). Samples were prepared in denaturing sample buffer (Bio-Rad), run on 4–15% Tris-HCl SDS polyacrylamide gels (Bio-Rad), and transferred to PVDF-membranes (Bio-Rad). Blots were probed with anti-MBP (Oncogene) and anti-β-actin antibodies. Blots were visualized using SuperSignal chemiluminescence kits (Pierce Biotechnology), and images were acquired and quantitated using FluorChem Q (AlphaInnotech) (Fig. 6A).

Quantitative image analysis

Mean fluorescence intensities for NF+ axons and MBP+ myelin sheaths within the dCST were obtained by using Slide Book 5.0 (Olympus) (Fig. 6B–J). Images of the dCST area from NF- and MBP-immunostained transverse sections were also taken at 40× magnification on an Olympus BX61 fluorescence microscope. For
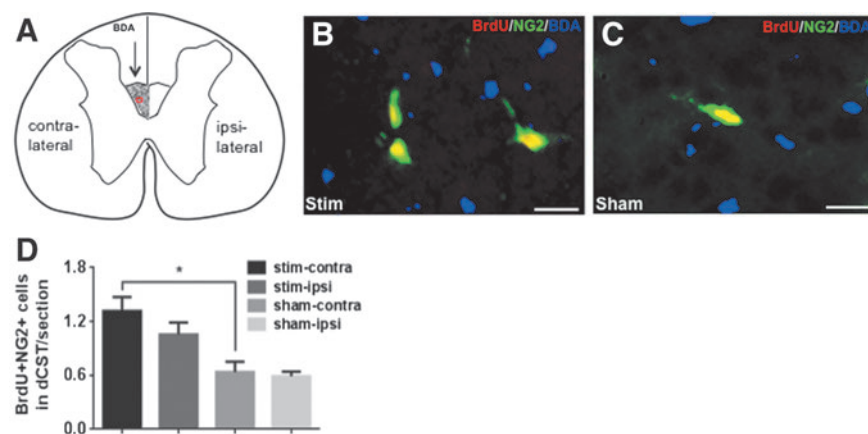
FIG. 4. Induced neuronal activity elicits oligodendrocyte progenitor cells' (OPCs') mitogenic response in the dorsal corticospinal tract (dCST) in subchronic spinal cord injury (SCI). **(A)** Diagram of spinal cord showing biotinylated dextran amine (BDA)-labeled contralateral and unlabeled ipsilateral sides with regard to induction of neuronal activity in the M1 cortex. The contralateral dCST was identified by the presence of BDA-labeled axons (shadowed area), and the symmetric area across the midline identified the ipsilateral dCST. All cell counts were performed within the dCST as described in the Methods section. Briefly, 5-bromo-2'-deoxyuridine (BrdU)[+]/neural/glial antigen (NG2)[+] cells (proliferating OPCs) were labeled using the Cell Count tool in ImageJ to prevent the same cells from being counted more then once; the number of labeled cells for each section was automatically recorded. The red box in the dCST represents areas imaged in panels B and C. **(B, C)** Representative images from R-3 mm spinal cord segments show distribution of BrdU[+]/NG2^{+}-proliferating OPCs in the contralateral dCST (with BDA[+] axons) in stimulated **(B)** and sham-stimulated **(C)** animals. **(D)** Total BrdU[+]/NG2^{+} cells in the dCST ($n = 6$ per group). The number of proliferating OPCs/section was averaged from R-3mm, R-6mm, R-9mm, C-3mm, C-6mm, and C-9mm spinal cord segments. More BrdU[+]/NG2^{+} cells were seen in stim-contralateral **(B)** than in sham-contralateral dCST **(C)**. One way analysis of variance (ANOVA) analysis was conducted for data in panel D with significance indicated as *$p < 0.05$. Errors bars indicate SEM. Scale bar in panels B and C is 10 μm.
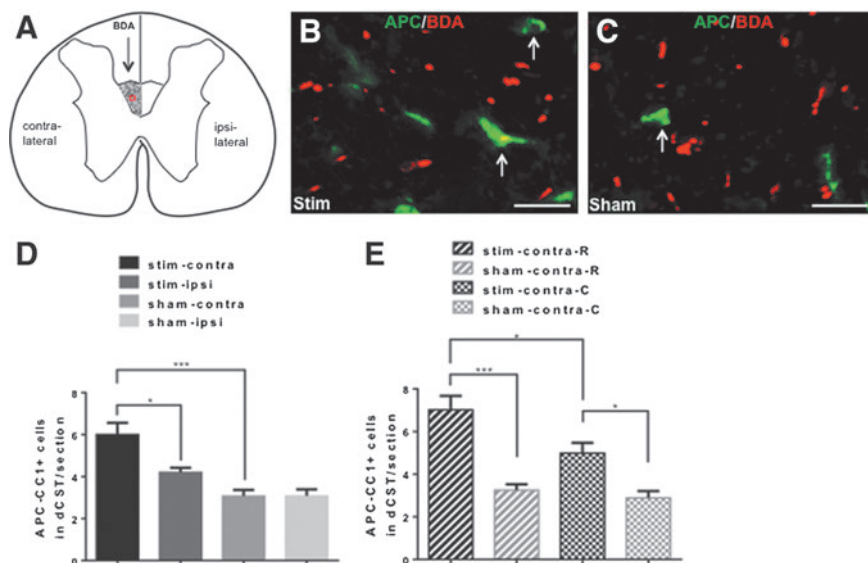

FIG. 5. Induced neuronal activation increases oligodendrogenesis in the dorsal corticospinal tract (dCST) in subchronic spinal cord injury (SCI). **(A)** Diagram of spinal cord showing biotinylated dextran amine (BDA)-labeled contralateral and unlabeled ipsilateral sides with regard to induction of neuronal activity in the M1 cortex. Shadowed area is the contralateral dCST, and the red box represents areas imaged in panels B and C. **(B, C)**. Representative images from R-3 mm spinal cord segments show distribution of APC-CC1^{+} mature oligodendrocytes (arrows) in contralateral dCST (with BDA[+] axons) in stimulated **(B)** and sham-stimulated **(C)** animals. **(D)** Total number of oligodendrocytes in spinal cord dCST ($n = 6$ per group). Cell counting method is the same as described Figure 4. The number of oligodendrocyte/section was averaged from R-3 mm, R-6 mm, R-9 mm, C-3 mm, C-6 mm, and C-9 mm spinal cord segments. Higher numbers of oligodendrocytes were seen in stim-contralateral dCST than in stim-ipsilateral and sham-contralateral dCST. **(E)** Total number of oligodendrocytes in the rostral (R) and caudal (C) contralateral dCST ($n = 6$ per group). The number of oligodendrocyte/section within the R- (R-3 mm, R-6 mm, R-9 mm) and C segments (C-3 mm, C-6 mm, and C-9 mm) of the contralateral dCST was compared between stimulated and sham-stimulated animals. Although M1-induced neuronal activity generates a higher number of oligodendrocytes in R rather than in C segments of the dCST in stimulated animals, the number of oligodendrocytes within both of these segments was higher than in their respective sham-stimulated controls. One way analysis of variance (ANOVA) was conducted with significance indicated as *$p < 0.05$, ***$p < 0.001$. Errors bars indicate SEM. Scale bar in panels B and C is 20 μm.
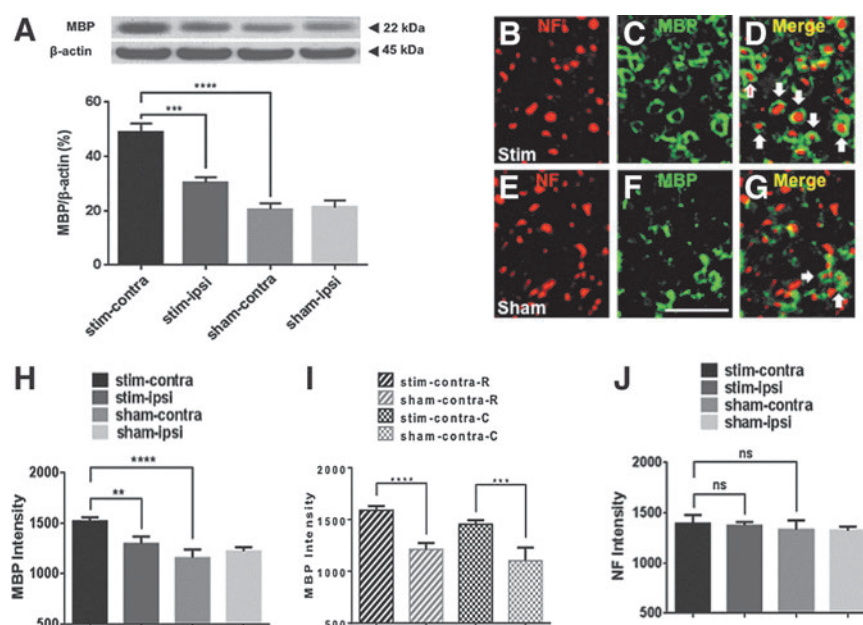
Page | 33

FIG. 6. Induced neuronal activation increases remyelination in the dorsal corticospinal tract (dCST) in subchronic spinal cord injury (SCI). **(A)** Western blotting data. Myelin basic protein (MBP) levels normalized to β-actin expression in injured spinal cord ($n = 6$ per group); expression of MBP in the stim-contralateral dorsal spinal cord was upregulated by induced neuronal activation as compared with stim-ipsilateral and sham-contralateral dorsal spinal cord. **(B–G)** Representative images from R-3 mm spinal cord segments showing MBP$^+$ sheaths myelinating neurofilament (NF)$^+$ axons in the contralateral dCST of stimulated animals **(B–D)** and sham-stimulated animals **(E–G)** ($n = 6$ per group; arrows indicate myelinating sheaths that surround axons). **(H)** Fluorescent intensity of MBP$^+$ sheaths/ section was averaged from R-3 mm, R-6 mm, R-9 mm, C-3 mm, C-6 mm, and C-9 mm spinal cord segments. Fluorescence intensity of MBP$^+$ sheaths in the stim-contralateral dCST was higher than in the stim-ipsilateral and sham-contralateral dCST. **(I)** Fluorescence intensity of MBP$^+$ sheaths in the rostral and caudal contralateral dCST. M1-induced neuronal activity elicited remyelination in both rostral and caudal segments of the spinal cord dCST as compared with their respective controls. **(J)** Fluorescent intensity of NF$^+$ axons/ section was averaged from R-3 mm, R-6 mm, R-9 mm, C-3 mm, C-6 mm, and C-9 mm spinal cord segments. Fluorescence intensity of NF$^+$ axons in the spinal cord dCST of four experimental groups did not differ. One way analysis of variance (ANOVA) was conducted with significance indicated as $**p < 0.01$, $***p < 0.001$, $****p < 0.0001$. Errors bars indicate SEM. Scale bar in panels B–G is 4 μm.

quantification, images were opened in Slidebook 5.0. The mean fluorescence intensities from a region of interest (ROI) that covered the dCST were obtained for each channel separately using the Intensity Statistics function within the Statistics menu. In Figure 6, mean fluorescence intensities are reported per section as well; therefore, the same averaging across rostral and caudal regions as reported for cell counting of oligodendrocytes was repeated here (Fig. 6H–J).

Confocal microscopy and axon-OPC synapse counting

Confocal microscopy (Olympus FluoView1000) was used to image axon-OPC synapses within the dCST. The criterion for axon-OPC synapses were that within a 1 μm optical image, BDA$^+$ dCST axons had to colocalize with synaptophysin, and this double-labeled component had to be adjacent to the cell body or proximal process of a NG2$^+$ OPC (Fig. 7A–D). Axon-OPC synapses were counted in the contralateral side of stimulated and sham animals (Fig. 7E). The counting for synapses from 1 μm optical images of the dCST was done using ImageJ as described.

Hindlimb motor function assay

Grid-walk assay was performed weekly from day 28 to day 49. Animals were pre-trained for 3 days before the first testing day. Animals were required to run two round trips across a 120 cm horizontal ladder beam that had 40 irregularly spaced (1–3 mm) metal bars (0.8 cm diameter). All hindlimb steps were videotaped, and analyzed in slow motion. The criteria for a correct step were that all digits held the bar and that the animal placed the palm of the paw directly onto the bar.

Steps with slips and misplacements were incorrect steps. The correct-step rate was calculated as number of correct steps over number of total steps. The data from all time points were normalized to the pre-stimulation (day 28) correct-step rate. Therefore, the normalized correct-step rate was calculated as the correct-step rate at a particular time point over the correct-step rate on day 28 times 100% (Fig. 8).

Statistical analysis

Data were analyzed from the following groups: (1) stim-contralateral (stim-contra), contralateral to the implanted electrode in stimulated animals; (2) stim-ipsilateral (stim-ipsi), ipsilateral to the implanted electrode in stimulated animals; (3) sham-contralateral (sham-contra), contralateral to the implanted electrode in sham-stimulated animals, and (4) sham-ipsilateral (sham-ipsi), ipsilateral to the implanted electrode in sham-stimulated animals. Comparisons were made between stim-contra and sham-contra, or between stim-contra and stim-ipsi. IHC and Western blot data were analyzed using one way analysis of variance (ANOVA); grid-walk assay data were analyzed with two-way ANOVA. The t test was used for comparison of axon-OPC synapses.

Results

Mild SCI causes demyelination within the dCST at the injury epicenter, but preserves dCST axons

We aimed to determine if induced neuronal activation affected oligodendrogenesis in the spinal cord after SCI. However, current
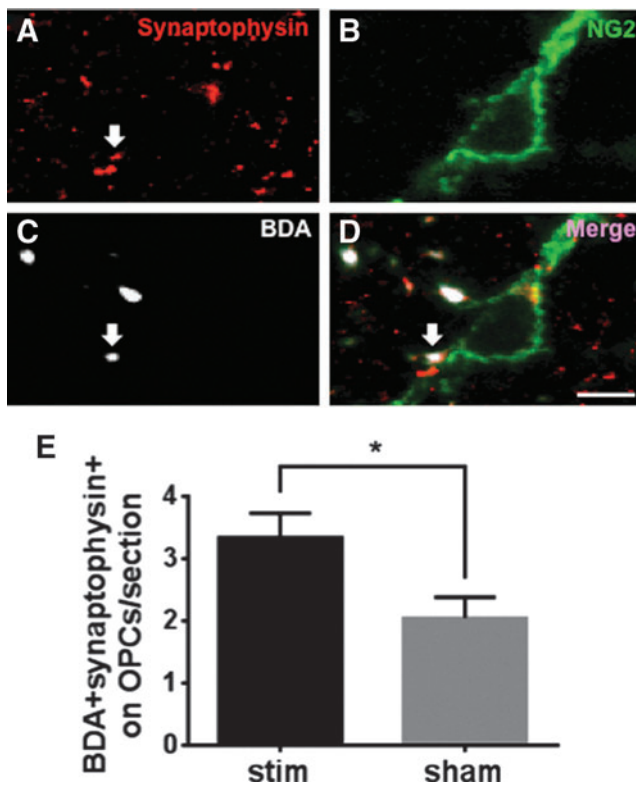
FIG. 7. Induced neuronal activity promotes formation of axon-oligodendrocyte progenitor cell (OPC) synapses in the contralateral dorsal corticospinal tract (dCST) in subchronic spinal cord injury (SCI). (A–D). Representative confocal images from the contralateral dCST of an R-3 mm spinal cord segment showing a biotinylated dextran amine (BDA)$^+$/synaptophysin$^+$ pre-synaptic component synapsing on an neural/glial antigen (NG)2$^+$ OPC (arrow; axon-OPC synapse). (E) Total number of axon-OPC synapses in spinal cord contralateral dCST ($n=6$ per group). We counted axon-OPC synapses using the same method as the one described for cell counting in Figures 4 and 5. The number of axon-OPC synapses/section was averaged from R-3 mm, R-6 mm, R-9 mm, C-3 mm, C-6 mm, and C-9 mm spinal cord segments. The number of axon-OPC synapses increases after induced neuronal activation. t-test was performed for data in panel E with significance indicated as *$p < 0.05$. Errors bars indicate SEM. Scale bar in panels A–D is 5 μm.
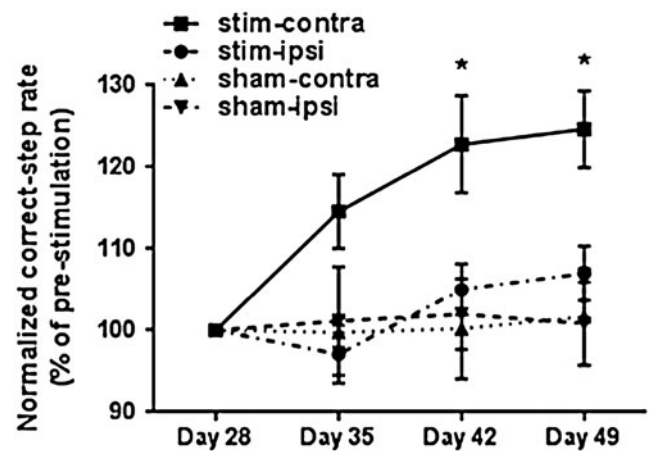

FIG. 8. Induction of neuronal activation through the M1 cortex in subchronic spinal cord injury (SCI) improves hindlimb motor function. Hindlimb motor function was assessed weekly after induction of neuronal activation using a grid-walk assay. The normalized correct-step rate represents the correct-step rate (number of correct steps over number of total steps) from all time points normalized to the pre-stimulation rate (day 28). Note that the normalized correct-step rate in the stim-contralateral hindlimb was significantly higher on days 42 and 49 than that in the stim-ipsilateral hindlimb and both hindlimbs of sham-stimulated animals. Two way analysis of variance (ANOVA) was conducted with significance indicated as *$p < 0.05$; errors bars indicate SEM.

M1-induced neuronal activity promotes proliferation of OPCs, oligodendrogenesis, and remyelination in subchronic SCI

Toward the aim of determining if induced neuronal activation affected oligodendrogenesis after SCI, we induced neuronal activation through electrical stimulation of the M1 cortex in a subchronic model of mild contusive SCI at T10 (experimental timeline is described in Fig. 1). Four weeks after SCI, we implanted unilateral electrodes over the M1 cortex and induced neuronal activation through electrical stimulation for a period of 3 weeks. In the last week of stimulation, BrdU was injected to label proliferating cells (Fig. 1). All animals were euthanized on day 49, and effects on oligodendrogenesis were analyzed in spinal cord transverse sections that were cut 3 mm, 6 mm, and 9 mm rostral and caudal from the lesion epicenter (Fig. 2). First, we examined proliferation of OPCs in the dCST after stimulation by counting BrdU$^+$/NG2$^+$ cells (proliferating OPCs) using ImageJ (Fig. 4). The contralateral dCST was identified by the presence of BDA-labeled axons, and the symmetric area across the midline represented the ipsilateral dCST (Fig. 4A). We counted 0–4 proliferating OPCs within the dCST in each 40 μm section (Fig. 4B,C); therefore, the number of proliferating OPCs from all the sections was averaged. The number of proliferating OPCs was higher in stim-contra dCST than in sham-contra dCST ($p < 0.05$). In stim-ipsi dCST, the trend for proliferating OPCs was higher than in sham-ipsi dCST, and lower than in stim-contra; however, these differences did not reach statistical significance (Fig. 4D). These data show that in subchronic SCI, induced neuronal activity promotes proliferation of OPCs.

Next, we wanted to determine if the increased proliferation of OPCs that was generated by induced neuronal activity leads to a higher number of oligodendrocytes (APC-CC1$^+$ cells; Fig. 5). Cell counting was also performed with ImageJ in dCST from the

rodent models of SCI induce loss of oligodendrocytes and axons and cause a contusive cyst at the injury epicenter. Therefore, for this study, we utilized a mild model of SCI that was inflicted by a 40 kdyn impact at T10. In the subchronic stage (49 days after injury; Fig. 1), the mild contusive SCI did not create a contusive cyst at the injury epicenter, and there was no scar tissue surrounding the injured tissue at the epicenter of the lesion (Fig. 3A and C). This mild contusive SCI did result in partial demyelination of dCST axons at the lesion epicenter (Fig. 3B and D). To assess axonal preservation of the dCST axons that project to the contralateral spinal cord, on day 28 we injected BDA unilaterally into the M1 cortex. Three weeks after injection, surviving BDA-labeled axons within the dCST were seen at the epicenter of the SCI (Fig. 3F). Despite demyelination within the dCST at the SCI epicenter, BDA-labeled axons survived caudal (L2) from the T10 injury (Figs. 2 and 3G). These data established a mild thoracic contusive SCI as a good model to study potential effects of induced neuronal activity on oligodendrogenesis and remyelination in the injured spinal cord.

transverse section. Using Image J, we counted 1–12 oligodendrocytes within the dCST in each 40 μm section (representative images in Fig. 5B, C). The number of oligodendrocytes in the stim-contra dCST was higher than in sham-contra ($p < 0.001$) and stim-ipsi ($p < 0.05$) dCST, and there was no difference between sham-contra and sham-ipsi dCST (Fig. 5D). Within the stim-contra dCST, the number of oligodendrocytes in segments rostral from the SCI epicenter was higher than in caudal segments ($p < 0.05$). The number of oligodendrocytes in rostral stim-contra dCST was also higher than that in rostral sham-contra dCST ($p < 0.001$). However, this affect of neuronal activity was not restricted to the rostral region, as the number of oligodendrocytes in caudal stim-contra dCST was higher than that in caudal sham-contra dCST ($p < 0.05$). In sham animals, the number of oligodendrocytes did not differ between the rostral and caudal dCST (Fig. 5E). These data show that in subchronic SCI, induced neuronal activity promotes oligodendrogenesis.

To determine if the increase in oligodendrocytes resulted in re-myelination of demyelinated dCST axons, we first assessed total MBP protein levels in the injured dorsal spinal cord following induced neuronal activation using Western blotting. MBP protein levels were higher in the stim-contra dorsal spinal cord than in the same region in stim-ipsi ($p < 0.001$) and sham-contra dorsal spinal cord ($p < 0.0001$). MBP protein levels did not differ between the dorsal sham-contra and sham-ipsi (Fig. 6A). To further examine the status of myelination within the dCST following induced neuronal activation, we assessed MBP$^+$ sheath formation by immunofluorescence (representative images are presented in Fig. 6C, D, F, and G).[13] MBP$^+$ sheath formation was increased in stim-contra dCST compared with sham-contra dCST ($p < 0.0001$) and stim-ipsi dCST ($p < 0.01$), and it did not differ between the sham-contra and sham-ipsi dCST (Fig. 6H). Both rostral and caudal segments of stim-contra dCST had more MBP$^+$ sheaths than the rostral ($p < 0.0001$) and caudal ($p < 0.001$) dCST, respectively, of sham-stimulated animals. However, within the stim-dCST there was no difference in MBP$^+$ sheath formation in rostral and caudal regions (Fig. 6I). Therefore, MBP$^+$ sheath formation corresponds to the number of oligodendrocytes as long as a critical number of oligodendrocytes is reached. The possibility that the increase in MBP$^+$ sheaths in response to electrical stimulation of M1 cortex occurs as a result of a higher loss of axons in sham-stimulated animals or because of myelination of regenerated axons of the dCST remains, considering that this form of stimulation has shown to induce axonal regeneration.[14–16] To account for these possibilities, we assessed the number of NF$^+$ axons by immunofluorescence (representative images are presented in Fig. 6B, E, D, and G).[13] However, we found that the fluorescent intensity of NF$^+$ axons within the dCST did not differ in the four experimental groups; therefore, differences in the number of axons are not responsible for the observed increase in remyelination. Taken together, these data indicate that in subchronic SCI, induced neuronal activity enhances remyelination of surviving axons.

M1-induced neuronal activity increases the number of axon-OPC synapses in subchronic SCI

Having established that induced neuronal activity promotes proliferation of OPCs, oligodendrogenesis, and remyelination in sub-chronically injured spinal cord, we aimed to determine a mechanism through which these effects are mediated. In EB-induced demyelination, endogenous neuronal activity within demyelinated axons promotes formation of generate *de novo* synapses

with OPCs, which go on to remyelinate.[6] Therefore, we examined if the number of axon-OPC synapses in the injured spinal cord changed in response to induced neuronal activity. Thus, we compared the number of axon-OPC synaptic interactions from stimulated animals versus sham-stimulated animals where we defined such synapses as direct contact between BDA$^+$/synaptophysin$^+$ axonal terminals and NG2$^+$ OPCs (representative images are presented in Fig. 7A–D). We found that the number of axon-OPC synapses in stim-contra dCST was higher than in sham-contra dCST ($p < 0.05$; Fig. 7E). These data show that in subchronic SCI, induced neuronal activity increases the number of axon-OPC synapses, indicating that the oligodendrocyte mitogenic response could be mediated through excitatory axon-OPC synapses.

M1 neuronal activity promotes recovery of motor function

Finally, we determined if neuronal activity induced through electrical stimulation of M1 cortex generated recovery of fine hindlimb motor function. Using a grid-walk assay, we compared the normalized correct-step rate (correct steps/total steps normalized to the pre-stimulation rate) of the contralateral and ipsilateral hindpaw in stimulated and sham-stimulated animals. This normalization step was done to account for the variability that could be introduced as a result of the difference in the SCI between each animal. We found that normalized correct-step rate for stim-contra hindlimbs significantly increased 2 weeks after stimulation (day 42) as compared with the stim-ipsi ($p < 0.05$), sham-contra ($p < 0.05$), and sham-ipsi ($p < 0.05$) hindlimbs. The increase persisted until the experimental end-point (day 49) ($p < 0.05$) (Fig. 8). These data demonstrate that in subchronic SCI, neuronal activity promotes recovery of motor function.

Discussion

This study demonstrates that neuronal activation induced through electrical stimulation of the M1 motor cortex elicits proliferation of OPCs in stimulated white matter tracts of the injured spinal cord, which in turn generates a higher number of oligodendrocytes and enhances remyelination within these tracts. Neuronal activation also increased the number of axon-OPC synapses in stimulated white matter tracts of the injured spinal cord. This increase in axon-OPC synapses indicates that such synapses could mediate these effects. The abovementioned effects in cells of the oligodendrocyte lineage and their interactions with axons are associated with an improvement in motor function. Collectively, our findings confirm that activity-dependent myelination is a mechanism of nervous system plasticity in the injured spinal cord. In addition, our work is proof of concept that neuronal activity induced through cortical stimulation is a valid therapeutic strategy for treatment of SCI and other demyelination disorders.

Evidence of continued remyelination after SCI has cast doubt on whether remyelination is a valid therapeutic target in treatment of SCI.[8,17] However, several lines of evidence confirm that remyelination is a feasible target for inducing neurological recovery after SCI. First, 3 months after SCI, evidence of *demyelination* and *dysmyelination* remain in the injured spinal cord both at the epicenter and distal from the injury.[8] *Demyelination* (lack of myelin) or *dysmyelination* (abnormal myelin) reduces efficacy of axonal signal transduction, and leads to axonal degeneration. Loss of oligodendrocytes is noted within the 1st h after SCI,[18] and persists for at least 3 weeks.[19,20] However, SCI also causes an oligodendroglia regenerative response, which consists of extensive proliferation

of OPCs,[8,21–24] and their differentiation into oligodendrocytes.[8,18,21,22] Partial *demyelination* and *dysmyelination* that persists 8 weeks after SCI is estimated to cause a 21% decrease in conduction velocity through remyelinated axons,[25] and such alterations in conduction velocities can lead to paralysis. Second, minimal sparing of myelinated axons is sufficient to restore locomotion. Survival of 5–10% of myelinated white matter axons concentrated towards the pial surface is sufficient to restore walking in cats after SCI.[26] Finally, interventions that enhance remyelination improve neurological function after SCI. Transplanted shiverer-derived neural progenitor cells (NPCs) survive in the injured spinal cord; generate neurons, astrocytes and oligodendrocytes; promote axonal growth; and prevent atrophy at an equal rate to that of wild type NPCs. However, the inability of shiverer-derived NPCs to form compact myelin because of a deletion of the myelin basic protein (MBP) gene renders them incapable of restoring motor function after transplantation in the injured spinal cord, whereas wildtype NSCs that form compact myelin are able to restore motor function.[27]

Myelination of axons in the CNS is necessary for integrated motor, sensory, and cognitive functions; this is a dynamic process that is regulated by endogenous neuronal activity. Activity-dependent myelination is emerging as a mechanism of CNS plasticity.[2] Experimentation in zebrafish highlights subtle differences in mechanisms through which endogenous neuronal activity regulates myelination in the spinal cord.[28,29] One study finds that neuronal activity-dependent synaptic release regulates myelination first by altering the number of OPCs, where induction of neuronal activity increases the number of OPCs whereas inhibition decreases the number of OPCs, and second, by increasing the initial formation of myelin sheaths, where myelin sheaths are defined as being >5 μm in length.[29] Another study, where the myelin sheath is not defined by size, finds that neuronal activity-dependent secretion regulates myelination by extending and stabilizing myelin sheaths formed on select axons rather then affecting the initial step of myelin sheath formation.[28] Interestingly, myelin sheaths form on inactive axons, but they are shorter in length; when activity of neighboring axons is suppressed, inhibition of sheath growth is relieved.[28] This suggests that desynchronized activity in axons (a characteristic of axonal tracts after SCI) can lead to dysmyelination, insufficient or structurally altered myelin formation.

Effects of induced neuronal activity on oligodendrogenesis and myelin remodeling are similar to the effects of endogenous neuronal activity, that is induction of neuronal activity through cortical stimulation promotes oligodendrogenesis and myelin remodeling in subcortical white matter tracks of the brain,[12] and in the uninjured spinal cord.[11] Our work illustrates that the effects of induced neuronal activation persist in the injured spinal cord, where we first noted an increase in OPC proliferation that surpassed the endogenous OPC proliferative response after SCI.[8] Interestingly, we observed a trend of increased proliferation of OPCs in the ipsilateral dCST, which was not stimulated. Such an observation can be explained by the introduction of activity through sprouting of CST tracts. The mild SCI model used in this study is designed to minimize axonal damage; however, some axonal damage can occur. Axonal outgrowth from damaged contralateral dCST axons, promoted by cortical stimulation, could be responsible for stimulation of OPC proliferation in the ipsilateral dCST, albeit at a lower rate. Concomitantly to the increase in proliferating OPCs, induced neuronal activity increases the number of oligodendrocytes and promotes remyelination within the injured spinal cord. The parallel increase in OPCs and oligodendrocytes described here and as

previously reported[11,12] is a subtle differences compared with endogenous neuronal activity, which depletes the number of OPCs as the number of oligodendrocytes increases.[6]

Mechanisms through which neuronal activity modulates oligodendrogenesis and myelination are under investigation. In our SCI model, induced neuronal activation increases axon-OPC synapses in the dCST, a white matter tract that is devoid of neuronal spines, dendrites, and somata. Induced neuronal activation has been reported to promote glutamate release in white matter tracts.[30] Axon-OPC synapses, which exhibit similar plasticity as neuronal synapses,[31] could mediate the effects of glutamate in OPCs. In EB-induced demyelination lesions, AMPA receptors in OPCs mediate effects of neuronal activity exerted through glutamate on OPC proliferation, differentiation, and remyelination.[6] Further work is needed to ascertain the role of axon-OPC synapses in activity-dependent regulation of oligodendrogenesis and remyelination, as these could be mediated by other mechanisms. For example, vesicular release at non-synaptic axon-OPC junctions can also induces myelination,[32] potentially through sodium-dependent glutamate transporters.[33] Additionally, *in vitro* AMPA receptors do not enhance myelin formation even though they upregulate differentiation of OPCs into oligodendrocytes in response to endogenous neuronal activity.[34] Further, in the presence of neuregulin and brain-derived neurotrophic factor (BDNF), it is *N*-methyl-D-aspartate (NMDA) receptors in OPCs that mediate neuronal activity-dependent effects of glutamate in enhancing remyelination.[35] In addition to neurotransmitter-mediated effects on myelination, active axons release a signal that stimulates astrocytes to release platelet-derived growth factor (PDGF), an OPC mitogen.[3] Therefore, it is possible that effects of neuronal activation on oligodendrogenesis and remyelination throughout development or in response to injury are exerted through different mechanisms. In the context of development or injury, induced and endogenous neuronal activity could act through different mechanisms.

Induced neuronal activity modulates motor function in uninjured animals, and pharmacological agents that block oligodendrogenesis inhibit such modulation.[12] Additionally, motor skill learning is hindered when OPC differentiation into oligodendrocytes is blocked.[4] In accordance with these reports, our work demonstrates that induced neuronal activation improves motor function in subchronic SCI. Specifically, we demonstrate that M1 induction of neuronal activity improves fine hindpaw motor function exclusively in the treated limb. Hindpaw motor function was assessed while the animals were not being stimulated, affirming that this mode of clinically applicable stimulation is therapeutic rather than neuroprosthetic.

In addition to improvements in oligodendrogenesis and remyelination, the stimulation paradigm described in the current study was previously shown to promote recovery of motor function after unilateral pyramidotomy that coincides with augmented sprouting of dCST.[15,16,36] However, regeneration of the CST axons alone might not be sufficient for recovery of motor function. Optogenetic activation of the CST terminals shows that SOX11-expressing regenerated CST axons form functional synapses in the newly innervated gray matter of the spinal cord, yet fail to improve motor function.[37] It is possible that the regenerated axons do not form a sufficient number of synapses to generate a functional output, or that the newly formed synapses are not properly targeted. However, a recent study in the visual system introduced the possibility that regenerated axons need to be myelinated to generate functional recovery.[38]

Conclusion

In conclusion, our work illustrates that epidural cortical stimulation is a valid therapeutic approach for treatment of patients with spinal cord injury. Cortical stimulation results in neuronal activation that induces axonal regeneration. In addition, our work has shown that neuronal activation also induces an oligodendroglial regenerative effect. The mechanism through which this occurs remains to be delineated; however, we show that this could occur through axon-OPC synapses. Other studies have shown that enhancement of remyelination or myelin remodeling through induced neuronal activation is a feasible therapeutic strategy in treatment of demyelination disorders such multiple sclerosis or enhancement of cognitive and motor functions.[4,6,12]

Acknowledgments

Author Disclosure Statement

No competing financial interests exist.

References

1. Young, K.M., Psachoulia, K., Tripathi, R.B., Dunn, S.J., Cossell, L., Attwell, D., Tohyama, K., and Richardson, W.D. (2013). Oligodendrocyte dynamics in the healthy adult CNS: evidence for myelin remodeling. Neuron 77, 873–885.
2. Fields, R.D. (2015). A new mechanism of nervous system plasticity: activity-dependent myelination. Nat. Rev. Neurosci. 16, 756–767.
3. Barres, B.A., and Raff, M.C. (1993). Proliferation of oligodendrocyte precursor cells depends on electrical activity in axons. Nature 361, 258–260.
4. McKenzie, I.A., Ohayon, D., Li, H., de Faria, J.P., Emery, B., Tohyama, K., and Richardson, W.D. (2014). Motor skill learning requires active central myelination. Science 346, 318–322.
5. Liu, J., Dietz, K., DeLoyht, J.M., Pedre, X., Kelkar, D., Kaur, J., Vialou, V., Lobo, M.K., Dietz, D.M., Nestler, E.J., Dupree, J., and Casaccia, P. (2012). Impaired adult myelination in the prefrontal cortex of socially isolated mice. Nat. Neurosci. 15, 1621–1623.
6. Gautier, H.O., Evans, K.A., Volbracht, K., James, R., Sitnikov, S., Lundgaard, I., James, F., LaoPeregrin, C., Reynolds, R., Franklin, R.J., and Karadottir, R.T. (2015). Neuronal activity regulates remyelination via glutamate signalling to oligodendrocyte progenitors. Nat. Commun. 6, 8518.
7. Alizadeh, A., Dyck, S.M., and Karimi-Abdolrezaee, S. (2015). Myelin damage and repair in pathologic CNS: challenges and prospects. Front. Mol. Neurosci. 8, 35.
8. Hesp, Z.C., Goldstein, E.Z., Miranda, C.J., Kaspar, B.K., and McTigue, D.M. (2015). Chronic oligodendrogenesis and remyelination after spinal cord injury in mice and rats. J. Neurosci. 35, 1274–1290.
9. Belegu, V., Oudega, M., Gary, D.S., and McDonald, J.W. (2007). Restoring function after spinal cord injury: promoting spontaneous regeneration with stem cells and activity-based therapies. Neurosurg. Clin. N. Am. 18, 143–168, xi.
10. Demerens, C., Stankoff, B., Logak, M., Anglade, P., Allinquant, B., Couraud, F., Zalc, B., and Lubetzki, C. (1996). Induction of myelination in the central nervous system by electrical activity. Proc. Natl. Acad. Sci. U. S. A. 93, 9887–9892.
11. Li, Q., Brus-Ramer, M., Martin, J.H., and McDonald, J.W. (2010). Electrical stimulation of the medullary pyramid promotes proliferation and differentiation of oligodendrocyte progenitor cells in the corticospinal tract of the adult rat. Neurosci. Lett. 479, 128–133.
12. Gibson, E.M., Purger, D., Mount, C.W., Goldstein, A.K., Lin, G.L., Wood, L.S., Inema, I., Miller, S.E., Bieri, G., Zuchero, J.B., Barres, B.A., Woo, P.J., Vogel, H., and Monje, M. (2014). Neuronal activity promotes oligodendrogenesis and adaptive myelination in the mammalian brain. Science 344, 1252304.
13. Carmel, J.B., Berrol, L.J., Brus-Ramer, M., and Martin, J.H. (2010). Chronic electrical stimulation of the intact corticospinal system after unilateral injury restores skilled locomotor control and promotes spinal axon outgrowth. J. Neurosci. 30, 10918–10926.
14. Talbott, J.F., Nout–Lomas, Y.S., Wendland, M.F., Mukherjee, P., Huie, J.R., Hess, C.P., Mabray, M.C., Bresnahan, J.C., and Beattie, M.S. (2016). Diffusion-weighted magnetic resonance imaging characterization of white matter injury produced by axon-sparing demyelination and severe contusion spinal cord injury in rats. J. Neurotrauma 33, 929–942.
15. Brus-Ramer, M., Carmel, J.B., Chakrabarty, S., and Martin, J.H. (2007). Electrical stimulation of spared corticospinal axons augments connections with ipsilateral spinal motor circuits after injury. J. Neurosci. 27, 13793–13801.
16. Carmel, J.B., Kimura, H., Berrol, L.J., and Martin, J.H. (2013). Motor cortex electrical stimulation promotes axon outgrowth to brain stem and spinal targets that control the forelimb impaired by unilateral corticospinal injury. Eur. J. Neurosci. 37, 1090–1102.
17. Carmel, J.B., and Martin, J.H. (2014). Motor cortex electrical stimulation augments sprouting of the corticospinal tract and promotes recovery of motor function. Front. Integr. Neurosci. 8, 51.
18. Powers, B.E., Sellers, D.L., Lovelett, E.A., Cheung, W., Aalami, S.P., Zapertov, N., Maris, D.O., and Horner, P.J. (2013). Remyelination reporter reveals prolonged refinement of spontaneously regenerated myelin. Proc. Natl. Acad. Sci. U. S. A. 110, 4075–4080.
19. Zai, L.J., and Wrathall, J.R. (2005). Cell proliferation and replacement following contusive spinal cord injury. Glia 50, 247–257.
20. Crowe, M.J., Bresnahan, J.C., Shuman, S.L., Masters, J.N., and Beattie, M.S. (1997). Apoptosis and delayed degeneration after spinal cord injury in rats and monkeys. Nat. Med. 3, 73–76.
21. Grossman, S.D., Rosenberg, L.J., and Wrathall, J.R. (2001). Temporal-spatial pattern of acute neuronal and glial loss after spinal cord contusion. Exp. Neurol. 168, 273–282.
22. Horky, L.L., Galimi, F., Gage, F.H., and Horner, P.J. (2006). Fate of endogenous stem/progenitor cells following spinal cord injury. J. Comp. Neurol. 498, 525–538.
23. Lytle, J.M., and Wrathall, J.R. (2007). Glial cell loss, proliferation and replacement in the contused murine spinal cord. Eur. J. Neurosci. 25, 1711–1724.
24. McTigue, D.M., Wei, P., and Stokes, B.T. (2001). Proliferation of NG2-positive cells and altered oligodendrocyte numbers in the contused rat spinal cord. J. Neurosci. 21, 3392–3400.
25. Rabchevsky, A.G., Sullivan, P.G., and Scheff, S.W. (2007). Temporal–spatial dynamics in oligodendrocyte and glial progenitor cell numbers throughout ventrolateral white matter following contusion spinal cord injury. Glia 55, 831–843.
26. Lasiene, J., Shupe, L., Perlmutter, S., and Horner, P. (2008). No evidence for chronic demyelination in spared axons after spinal cord injury in a mouse. J. Neurosci. 28, 3887–3896.
27. Blight, A.R. (1983). Cellular morphology of chronic spinal cord injury in the cat: analysis of myelinated axons by line-sampling. Neuroscience 10, 521–543.
28. Yasuda, A., Tsuji, O., Shibata, S., Nori, S., Takano, M., Kobayashi, Y., Takahashi, Y., Fujiyoshi, K., Hara, C.M., Miyawaki, A., Okano, H.J., Toyama, Y., Nakamura, M., and Okano, H. (2011). Significance of remyelination by neural stem/progenitor cells transplanted into the injured spinal cord. Stem Cells 29, 1983–1994.
29. Hines, J.H., Ravanelli, A.M., Schwindt, R., Scott, E.K., and Appel, B. (2015). Neuronal activity biases axon selection for myelination in vivo. Nat. Neurosci. 18, 683–689.
30. Mensch, S., Baraban, M., Almeida, R., Czopka, T., Ausborn, J., El Manira, A., and Lyons, D.A. (2015). Synaptic vesicle release regulates myelin sheath number of individual oligodendrocytes in vivo. Nat. Neurosci. 18, 628–630.
31. Kukley, M., Capetillo–Zarate, E., and Dietrich, D. (2007). Vesicular glutamate release from axons in white matter. Nat. Neurosci. 10, 311–320.
32. Paukert, M., and Bergles, D.E. (2006). Synaptic communication between neurons and NG2+ cells. Curr. Opin. Neurobiol. 16, 515–521.
33. Wake, H., Ortiz, F.C., Woo, D.H., Lee, P.R., Angulo, M.C., and Fields, R.D. (2015). Nonsynaptic junctions on myelinating glia promote preferential myelination of electrically active axons. Nat. Commun. 6, 7844.

34. Martinez-Lozada, Z., Waggener, C.T., Kim, K., Zou, S., Knapp, P.E., Hayashi, Y., Ortega, A., and Fuss, B. (2014). Activation of sodium-dependent glutamate transporters regulates the morphological aspects of oligodendrocyte maturation via signaling through calcium/calmodulin-dependent kinase IIbeta's actin-binding/-stabilizing domain. Glia 62, 1543–1558.

35. Fannon, J., Tarmier, W., and Fulton, D. (2015). Neuronal activity and AMPA-type glutamate receptor activation regulates the morphological development of oligodendrocyte precursor cells. Glia 63, 1021–1035.

36. Lundgaard, I., Luzhynskaya, A., Stockley, J.H., Wang, Z., Evans, K.A., Swire, M., Volbracht, K., Gautier, H.O., Franklin, R.J., Charles, F.-C., Attwell, D., and Karadottir, R.T. (2013). Neuregulin and BDNF induce a switch to NMDA receptor-dependent myelination by oligodendrocytes. PLoS Biol. 11, e1001743.

37. Carmel, J.B., Kimura, H., and Martin, J.H. (2014). Electrical stimulation of motor cortex in the uninjured hemisphere after chronic unilateral injury promotes recovery of skilled locomotion through ipsilateral control. J. Neurosci. 34, 462–466.

38. Jayaprakash, N., Wang, Z., Hoeynck, B., Krueger, N., Kramer, A., Balle, E., Wheeler, D.S., Wheeler, R.A., and Blackmore, M.G. (2016). Optogenetic interrogation of functional synapse formation by corticospinal tract axons in the injured spinal cord. J. Neurosci. 36, 5877–5890.

39. Bei, F., Lee, H.H., Liu, X., Gunner, G., Jin, H., Ma, L., Wang, C., Hou, L., Hensch, T.K., Frank, E., Sanes, J.R., Chen, C., Fagiolini, M., and He, Z. (2016). Restoration of visual function by enhancing conduction in regenerated axons. cell 164, 219–232.

Address correspondence to:
Visar Belegu, PhD
The International Center for Spinal Cord Injury
Hugo W. Moser Research Institute at Kennedy Krieger
Baltimore, MD 21205

E-mail: belegu@kennedykrieger.org

CrossMark

DIAGNOSTIC NEURORADIOLOGY

Subject-specific regional measures of water diffusion are associated with impairment in chronic spinal cord injury

Ann S. Choe[1,2] · Cristina L. Sadowsky[3,4] · Seth A. Smith[5,6] · Peter C. M. van Zijl[1,2] · James J. Pekar[1,2] · Visar Belegu[3,7]

Abstract

Purpose We aimed to identify non-invasive imaging parameters that can serve as biomarkers for the integrity of the spinal cord, which is paramount to neurological function. Diffusion tensor imaging (DTI) indices are sensitive to axonal and myelin damage, and have strong potential to serve as such biomarkers. However, averaging DTI indices over large regions of interest (ROIs), a common approach to analyzing the images of injured spinal cord, leads to loss of subject-specific information. We investigated if DTI-tractography-driven, subject-specific demarcation approach can yield measures that are more specific to impairment.

Methods In 18 individuals with chronic spinal cord injury (SCI), subject-specific demarcation of the injury region was performed using DTI tractography, which yielded three regions relative to injury (RRI; regions superior to, at, and below injury epicenter). DTI indices averaged over each RRI were correlated with measures of residual motor and sensory function, obtained using the International Standard of Neurological Classification for Spinal Cord Injury (ISNCSCI).

Results Total ISNCSCI score (ISNCSCI-tot; sum of ISNCSCI motor and sensory scores) was significantly ($p < 0.05$) correlated with fractional anisotropy and axial and radial diffusivities. ISNCSCI-tot showed strongest correlation with indices measured from the region inferior to the injury epicenter (IRRI), the degree of which exceeded that of those measured from the entire cervical cord—suggesting contribution from Wallerian degeneration.

Conclusion DTI tractography-driven, subject-specific injury demarcation approach provided measures that were more specific to impairment. Notably, DTI indices obtained from the IRRI region showed the highest specificity to impairment, demonstrating their strong potential as biomarkers for the SCI severity.

Keywords Spinal cord injury · Diffusion tensor imaging · Subject-specific analysis · Injury region demarcation

✉ Ann S. Choe
annschoe@gmail.com

1 Russell H. Morgan Department of Radiology and Radiological Science, Johns Hopkins University School of Medicine, Baltimore, MD 21205, USA

2 F.M. Kirby Research Center for Functional Brain Imaging, Kennedy Krieger Institute, 707 North Broadway, Baltimore, MD 21205, USA

3 International Center for Spinal Cord Injury, Kennedy Krieger Institute, Baltimore, MD 21205, USA

4 Physical Medicine and Rehabilitation, Kennedy Krieger Institute, Baltimore, MD 21205, USA

5 Radiology and Radiological Sciences, Vanderbilt University, Nashville, TN 37235, USA

6 Vanderbilt University Institute of Imaging Science, Vanderbilt University, Nashville, TN 37235, USA

7 Department of Neurology, Johns Hopkins University School of Medicine, Baltimore, MD 21205, USA

Introduction

Diffusion tensor imaging (DTI) [1, 2]-derived indices of injured spinal cord are sensitive to myelin and axonal damage [3–10] and report on the integrity of the cord at a molecular level that is useful for prognosis of recovery [11–14]. However, averaging DTI indices over large regions of interest

Springer

(ROIs), a common approach to analyzing the images of injured spinal cord, can lead to a loss of subject-specific information. Therefore, accurate image segmentation of the spinal cord and placement of more biochemically homogeneous ROI around injury epicenter may maximize the potential of DTI indices as non-invasive imaging biomarkers for the severity of SCI.

Methods for spinal cord segmentation can be broadly categorized as manual, automated, and semi-automated. Although most time-consuming, the manual segmentation [11, 15–17] is highly accurate. However, application of the fully automated methods [18–21] in clinical environment is complicated by the small size of the spinal cord that often leads to low-resolution images that are suboptimal for fully automated segmentation. In semi-automated methods, compromise is made between the accuracy of the manual method and the efficiency of the fully automated method—by first performing automated segmentation of the entire spinal cord, followed by manual segmentation of the spinal cord columns [21, 22].

After segmentation, ROIs must be placed along the longitudinal axis of spinal cord. In one conventional approach, an entire neurological region (e.g., cervical region) is defined as an ROI [21, 23]. Examples of other approaches include obtaining finer-grained ROIs by further dividing the neurological regions into arbitrary subregions (e.g., upper, middle, and lower cervical regions) [11] and single-vertebra levels (e.g., C1,…, C8) [14]. In these approaches, the placement of ROIs is entirely anatomically determined; i.e., ROIs are placed at the same anatomically defined regions for all participants, irrespective of their varying levels or size of lesion. Such methods have been successfully used to observe robust correlations between clinical measures of function and DTI indices [11, 14, 21, 23]. However, those methods are also potentially less sensitive to pathological changes due to extensive averaging of DTI index values over regions of healthy spinal cord. Such regional averaging can be minimized by placing the ROIs in regions that are subject- and injury region-specific, reflecting the varying levels and sizes of lesion in each individual [17, 24, 25].

In this study, we analyzed DTI data in individuals with chronic SCI by first delineating the spinal cord and its columns using a robust semi-automated segmentation method [24, 26] that utilizes DTI fiber tractography [14, 27, 28], and then adapting a subject-specific ROI placement approach to demarcate individual injury regions. We hypothesized that DTI indices obtained using the DTI tractography-driven, subject-specific ROI placement approach would better correlate with residual sensorimotor function, compared to those obtained using the non-subject-specific, anatomically determined ROI placement approach.

Material and methods

Participants

Initially, 19 individuals with chronic cervical SCI gave informed written consent to participate in the study, which was approved by the Johns Hopkins Medicine Institutional Review Board. Data from one individual was eventually excluded from further data analysis, as described in details below. Of the 19 individuals, 15 had traumatic injuries and four had non-traumatic (specifically, transverse myelitis (TM)) injuries. In individuals with TM, a 1-year follow-up chart review was performed to exclude those who subsequently developed neurological conditions that are unrelated to SCI. Subsequently, one individual with TM who was later diagnosed with recurrent disseminated encephalopathy was identified and excluded from further data analysis. The remaining cohort of 18 study participants (20–66 years, mean 47, M/F ratio 14/4; Table 1) consisted of 15 individuals with traumatic injuries and three individuals with TM.

Previously acquired spinal cord images from 10 healthy individuals (21–49 years, mean 33, M/F ratio 6/4) [24] were used as a control dataset.

Spinal cord injury classification

The International Standard of Neurological Classification for Spinal Cord Injury (ISNCSCI) scoring system, developed by the American Spinal Injury Association (ASIA), was used to determine the level and severity of SCI [29, 30], and the classification of SCI was provided by the ASIA Impairment Scale (AIS) grade system. The evaluations consisted of testing of five arm and leg muscles to assess residual motor functions, and light touch and pinprick examinations of 28 sensory dermatomes to assess residual sensory functions.

Four ISNCSCI metrics were tabulated: injury level (C2–C6), total motor score (sum of upper and lower extremity motor scores; maximum 100), total sensory score (sum of left and right light touch sensory scores; maximum 112), and the ISNCSCI-tot score (sum of total motor score and total sensory score; maximum 212). For the sensory score, the light touch examination scores were arbitrarily selected for use in the study, as scores from the light touch and pinprick sensory examinations were highly correlated ($R^2 = 0.89$).

Image acquisition

The image acquisition protocol and analysis pipeline used in this study were previously described in detail [24] and are summarized here.

All participants (including both the healthy control and SCI patient cohorts) were scanned on a Philips 3-T scanner, using a 16-channel neurovascular coil. In order to increase the

Table 1 Demographics of the individuals with chronic spinal cord injury (SCI)

No.	Age (year)	Time since injury (year)	Injury level	AIS grade	ISNCSCI motor	ISNCSCI sensory	ISNCSCI total	Sex	Cause
1	30	4	C2	A	0	13	13	F	Traumatic
2	38	1	C4	A	14	21	35	F	TM
3	50	24	C4	A	21	14	35	M	Traumatic
4	26	5	C2	B	1	12	13	M	Traumatic
5	52	34	C5	B	34	65	99	M	Traumatic
6	62	1	C4	C	6	24	30	M	Traumatic
7	53	11	C6	C	34	33	67	M	TM
8	60	4	C3	C	55	51	106	M	Traumatic
9	33	15	C2	C	51	60	111	M	Traumatic
10	28	3	C3	C	56	60	116	F	Traumatic
11	20	3	C4	C	23	96	119	F	TM
12	62	2	C4	D	69	28	97	M	Traumatic
13	54	32	C2	D	97	27	124	M	Traumatic
14	60	2	C5	D	68	95	163	M	Traumatic
15	66	3	C3	D	89	87	176	M	Traumatic
16	43	30	C5	D	92	112	204	M	Traumatic
17	39	1	C5	D	97	108	205	M	Traumatic
18	65	2	C2	D	100	110	210	M	Traumatic

Of the 19 individuals with chronic cervical SCI who initially provided informed written consent to participate in the study, data from one individual with TM was excluded from further data analysis after a 1-year follow-up chart review

AIS American Spinal Injury Association Impairment Scale, *ISNCSCI* International Standard of Neurological Classification for Spinal Cord Injury, *ISNCSCI-tot* total ISNCSCI score, *M* male, *F* female, *TM* transverse myelitis

directional resolution of the DTI dataset while minimizing the effect of motion, three DTI scans were acquired and entered into the tensor calculation as separate entities (i.e., no pre-calculation averaging was performed): multi-slice pulsed gradient spin echo sequence, $b = 0$ and 500 s/mm^2, 16 diffusion-weighted directions that sample a prolate tensor, TR/TE = 6300/63 ms, SENSE factor = 2, 96 × 96 × 40 volume matrix, 1.5 × 1.5 × 3 mm^3 resolution (axial sections of 3-mm thickness; zero-filled to 0.57 × 0.57 × 3 mm^3), and matrix size = 256 × 256 × 40. Field of view was chosen to span the length of the cervical spinal cord. Smith et al. [26] and Landman et al. [31, 32] optimized the above-mentioned imaging parameters used in this study.

Studies have shown that magnetization transfer imaging (MTI) can be used to obtain high-contrast and resolution images that can assist semi-automated segmentation of the spinal cord [6, 24, 26]. For the purpose of this study, we specifically exploited the high contrast and resolution of the MT-weighted images to aid the manual drawing of ROIs within individual spinal cord columns. Note that the MT-weighted images were utilized for ROI placement purpose only, and further analysis of the MT parameters was not performed. MT-weighted images were acquired using a three-dimensional spoiled gradient-echo sequence with multi-shot EPI readout: EPI factor = 3, TR/TE = 102/13 ms, $\alpha = 9°$, SENSE factor = 2, 368 × 276 × 40 image volume matrix, and 0.61 × 0.69 × 3 mm^3 resolution. MT weighting was achieved using a 24-ms, five-lobed, sinc-shaped saturation pulse with peak amplitude of 8.5 μT at offset frequency of 1.5 kHz.

Total image acquisition time, including survey, SENSE reference, sagittal T2-weighted (T2-w), short tau inversion recovery (STIR), three DTI, and two MTI scans, was 28 min.

Image processing and analysis

Image registration and diffusion tensor estimation

Coregistration, Adjustment, and Tensor-solving, a Nicely Automated Program (CATNAP), Johns Hopkins University School of Medicine, Baltimore, MD, USA [31], was used to perform volume-wise coregistration as well as the estimation of DTI-derived indices (i.e., fractional anisotropy (FA), axial diffusivity (AD), and radial diffusivity (RD)) [31]. Specifically, each diffusion-weighted image was registered to an initial $b = 0$ s/mm^2 (b_0; non-diffusion-weighted image) volume using a six degrees of freedom rigid body registration, and the DTI-derived indices were estimated using a multivariate log-linear fitting method. Also, the diffusion gradient tables were updated to account for any rotation prior to the diffusion tensor estimation.

Registration of the MT dataset to b_0 volume was performed in two steps. First, the MT dataset was registered to the b_0 volume using a three-dimensional, six degrees of freedom, rigid body transformation [33]. For added accuracy, this was followed by an additional two-dimensional registration, using a three degrees of freedom rigid body transformation that involved two in-plane translations and one rotation. The detailed

description of this registration process, as well as the process' degree of reproducibility, can be found in Smith et al. [26].

Diffusion fiber tractography of spinal cord columns and creation of column profiles

Diffusion fiber tractography was performed using DTIStudio [34]. MT images were used to manually place ROIs in the left and right lateral, dorsal, and ventral spinal cord columns, example of which is shown in Fig. 1. The manual ROI placement was performed on every third axial section along the entire cervical cord in order to yield seed regions for the tractography. FA threshold of 0.2 and a maximum tract turning angle of 60° were used as the stopping criterion, and spurious fibers were manually excluded. Finally, column profiles [26, 35] spanning the vertebral levels C2 and C6 were created for each DTI index. Detailed description of the data processing pipeline and the method's degree of reproducibility can be found in Smith et al. [26].

Previous study has shown that typical neck length of individuals is approximately 75 mm [26], corresponding to 25, 3-mm-thick image sections. Using this information, each column profile was normalized to 25 equally-distanced points that span the length of the cervical cord.

Demarcation of regions relative to injury

For each SCI patient, three regions relative to injury (RRI) were identified (Fig. 2). First, epicenter RRI (ERRI) was manually identified using each individual's sagittal T2-w and axial MT images. Superior RRI (SRRI) was then defined as the region located above the superior edge of the ERRI, up to approximately the length of one vertebral level (~15 mm). Similarly, inferior RRI (IRRI) was defined as the region located below the inferior edge of the ERRI, up to approximately the length of one vertebral level.

Next, locations of the RRIs within the normalized column profile were identified, and DTI index measures for each spinal cord column (left, right, dorsal, and ventral columns), within each RRI region (SRRI, ERRI, and IRRI), were obtained. In instances where severe spinal cord atrophy yielded non-measurable DTI values at the site of injury or the extent of injury site expanded beyond the C2 to C6 vertebral levels, ROIs were treated as having missing data points.
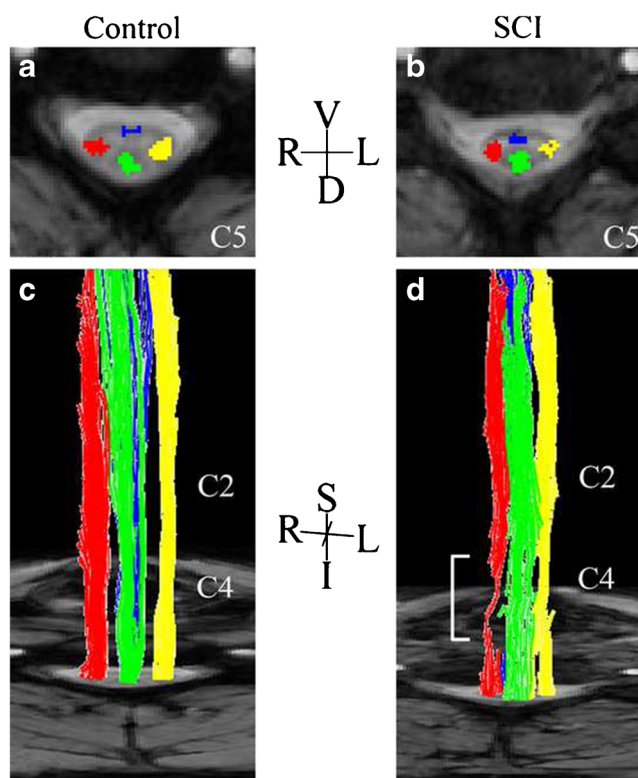

Fig. 1 Placement of seed regions in magnetization transfer (MT) images for diffusion fiber tractography. Examples of seed region placements are shown for images obtained from a healthy control (**a**, **c**) and an individual with spinal cord injury (SCI) (**b**, **d**). **a**, **b** Seed regions for the right lateral (*red*), left lateral (*yellow*), dorsal (*green*), and ventral (*blue*) spinal columns were placed within the MT images. **c**, **d** Diffusion tensor imaging (DTI) fiber tractography was performed using the seed regions. *White bracket* in **d** highlights the individual's injury epicenter. *V* ventral, *D* dorsal, *R* right, *L* left, *S* superior, *I* inferior, *C2–C5* cervical levels 2–5
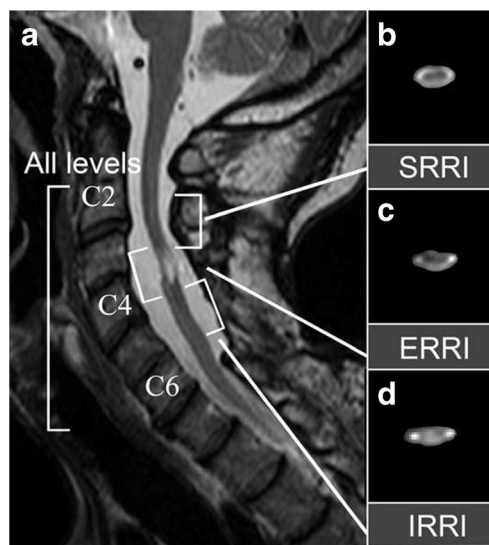

Fig. 2 Identification of regions relative to injury (RRI). **a** Sagittal T2-weighted (T2-w) images were used to demarcate subject-specific injury regions. Three regions relative to injury—regions superior to injury epicenter (SRRI; **b**), at injury epicenter (ERRI; **c**), and inferior to injury epicenter (IRRI; **d**)—were identified, where ERRI was defined as the injury epicenter, and SRRI and IRRI were defined as one vertebral level above and below the ERRI region. The entire length of the cervical spinal cord spanning the vertebral levels C2 to C6 was defined as the all level (AL) region. Representative axial views of fractional anisotropy (FA) maps for each corresponding RRI regions are shown in **b–d**, without diffusion direction color-coding

Statistical analysis

Statistical analysis was performed using MATLAB (The Mathworks, MA, USA).

A two-way analysis of variance (ANOVA) was performed to identify significant sources of variation on DTI-derived indices. The result was Bonferroni-corrected, and any corrected p values larger than 1 were set to 1.

Results of the ANOVA analysis were used to eventually conclude that spinal cord columns did not have significant effects on either the DTI indices or the degree of correlation between the DTI indices and ISNCSCI scores, as later described in the "Results" section. Based on this result, for each DTI-derived index, all following data analyses were performed using only the single "whole cord profile" (obtained by averaging the individual column profiles of the four spinal cord columns) instead of using separate cord profiles for each spinal cord columns. Similarly, as we are no longer separating ventrolateral motor columns from dorsal sensory columns by using the whole cord profile, ISNCSCI-tot score was selected as the behavioral outcome measure of choice.

The effect of spinal cord RRI on the degree of correlations between diffusion measurements (derived from the whole cord profiles of DTI index values) and residual sensorimotor function (obtained from ISNCSCI) was assessed using a series of linear regression analyses. Specifically, a set of four linear regression analyses was performed for each DTI-derived index, where ISNCSCI-tot was defined as a common independent variable, and four separate dependent variables were defined as DTI index values obtained from (1) the entire length of the cervical spinal cord (between vertebral levels C2–C6, here on referred to as "all levels" (AL)), (2) SRRI, (3) ERRI, and (4) IRRI regions. Bonferroni correction was used to account for multiple comparisons across different RRI regions.

In order to investigate if motor or the sensory ISNCSCI score had more explanatory power for DTI-derived indices, a stepwise regression analysis was performed. Specifically, the motor and sensory scores were considered as separate potential independent variables, and their effects on each SRRI- and IRRI-region DTI index were tested. And finally, stepwise regression analyses were performed to evaluate whether age and/or time since injury (TSI) had significant effects on DTI indices. TSI, age, and ISNCSCI-tot scores were considered as potential independent variables, and we tested for their effects on each IRRI-region DTI index. Correction for multiple comparisons was not performed for the two stepwise regression analyses.

Results

Demarcation of regions relative to injury

In an effort to increase the potential of DTI indices to serve as imaging biomarkers, we aimed to identify biochemically homogeneous ROIs that are more specific to the damage of the spinal cord, and two such classes of ROIs were initially investigated: (a) one class of ROI was identified using the described spinal cord column segmentation approach with DTI fiber tractography, and constituted of individual spinal cord columns (right and left lateral, dorsal, and ventral columns; Fig. 1). (b) The other class of ROI was identified using subject-specific injury region demarcation approach, and constituted of spinal cord RRIs (SRRI, ERRI, and IRRI regions; Fig. 2). The effect of spinal cord columns and RRI on FA, AD, and RD was tested using two-way ANOVA. This analysis revealed that significant effect ($p < 0.05$) of spinal cord RRI existed for all DTI indices (Table 2), indicating that DTI index values of different RRI regions were different from each other. The analysis also revealed that there was no significant effect of spinal cord columns on DTI indices (i.e., different spinal cord columns did not have significantly different DTI index values). Therefore, the relationship between DTI indices obtained from individual spinal cord columns and ISNCSCI scores was further investigated using a series of post hoc linear regression analyses, and no significant correlation between DTI indices from different spinal cord columns and ISNCSCI scores was observed (i.e., no significant lateral effects was observed; results not shown).

FA, AD, and RD values obtained by averaging over each ROI (i.e., AL, SRRI, ERRI, and IRRI regions) of the whole cervical cord profiles are summarized in Table 3 (note that hereon, an ROI from which a specific DTI measures is obtained will be expressed as a subscript of the DTI index—e.g., FA measurement obtained from the AL region is expressed as FA_{AL}). Lack of injury in healthy spinal cords renders the injury region demarcation and the identification of RRI regions inapplicable. Therefore, in healthy spinal cord, we only

Table 2 Effect of spinal cord column and spinal cord region-relative-to-injury (RRI) on diffusion tensor imaging (DTI) indices

DTI indices	Source of variation	
	Spinal cord columns (p value)	Spinal cord RRI (p value)
FA	0.258	0.004*
AD	0.539	0.002*
RD	0.781	0.002*

The effect of spinal cord column (right and left lateral, dorsal, and ventral columns) and RRI region (regions superior to, at, and inferior to injury epicenter) on fractional anisotropy (FA), axial diffusivity (AD), and radial diffusivity (RD) was tested using a two-way analysis of variance (ANOVA). Spinal cord RRI was identified as the main source of variation for all three DTI indices. In other words, DTI index values measured from each RRI region were significantly different from each other. Conversely, different spinal cord columns did not have significantly different DTI index values

*Statistically significant ($p < 0.05$; corrected)

Table 3 Mean and standard deviation measurement of each DTI index

	Mean ± SD				
	Healthy individuals	Individuals with SCI			
	AL	AL	SRRI	ERRI	IRRI
FA	0.72 ± 0.04	0.47 ± 0.09*	0.51 ± 0.10	0.46 ± 0.10	0.43 ± 0.13
AD (μm^2/ms)	2.04 ± 0.14	2.22 ± 0.28	2.13 ± 0.38	2.12 ± 0.31	2.47 ± 0.48
RD (μm^2/ms)	0.53 ± 0.09	1.15 ± 0.29*	1.01 ± 0.35	1.10 ± 0.30	1.37 ± 0.54

In healthy individuals, only the DTI indices from the all level (AL) region were obtained, and the measurements were then compared with the corresponding AL-region DTI index values from the individuals with SCI. Significant decrease in FA_{AL} (note that hereon, an ROI from which a specific DTI measures is obtained will be expressed as a subscript of the DTI index; e.g., FA measurement obtained from the AL region is expressed as FA_{AL}) and increase in RD_{AL} indicate severe damage in injured cords

SD standard deviation

*Statistically significant ($p < 0.05$; corrected)

considered DTI indices from the AL region. For the AL region, significant decrease in FA_{AL} ($p < 0.05$) and increase in RD_{AL} ($p < 0.05$) were observed in chronic SCI individuals compared to the healthy individuals—indicating severe damage in the injured cords.

Regional dependence of associations between impairment and diffusion indices

Next, we wanted to determine if there are correlations between DTI indices from each ROI and ISNCSCI-tot scores. For this, we utilized linear regression analysis. Table 4 lists the adjusted R^2 values, slopes with the corresponding p values, and intercept of the estimated regression lines for all three DTI indices.

Table 4 Spatial dependence of the correlation between DTI indices and total ISNCSCI scores

RRI	Adjusted R^2	Slope (p value)	Intercept
FA_{SRRI}	0.061	0.001 (0.666)	0.452
FA_{ERRI}	0.230	0.001 (0.102)	0.370
FA_{IRRI}	0.576	0.002 (0.002*)	0.236
FA_{AL}	0.389	0.001 (0.013*)	0.370
AD_{SRRI}	−0.051	−0.001 (1.000)	2.195
AD_{ERRI}	−0.008	−0.001 (1.000)	2.240
AD_{IRRI}	0.339	−0.005 (0.042*)	3.026
AD_{AL}	0.339	−0.001 (0.752)	2.365
RD_{SRRI}	0.009	−0.001 (1.000)	1.165
RD_{ERRI}	0.272	−0.003 (0.062)	1.381
RD_{IRRI}	0.466	−0.006 (0.009*)	2.091
RD_{AL}	0.343	−0.003 (0.025*)	1.448

Stronger correlation (i.e., larger R^2 value) is observed between total ISNCSCI scores (ISNCSCI-tot) and DTI indices obtained from the IRRI region, compared to that between the ISNCSCI-tot and DTI indices obtained from SRRI, ERRI, and AL regions—indicating spatial dependence of the correlation between DTI indices and total ISNCSCI scores

*Statistically significant ($p < 0.05$; corrected)

The slope and intercept values describe the existence of the correlations between variables, while R^2 values describe the strength of the correlations. Supplementary Fig. S1 visualizes the linear regression analysis results of FA. Results showed that a significant relationship exists between FA_{AL} and ISNCSCI-tot ($p = 0.013$). The slope was positive, indicating that as impairment became more severe (smaller ISNCSCI-tot), FA_{AL} values decreased. While this positive linear trend between FA and ISNCSCI-tot was preserved when FA_{AL} was further divided into subject-specific regions of FA_{SRRI}, FA_{ERRI}, and FA_{IRRI}, the correlation was significant only for FA_{IRRI} ($p = 0.002$). Also, the adjusted R^2 value for the FA_{IRRI} (0.576) was larger than that for the FA_{AL} (0.389). Finally, this tendency of tighter correlation between ISNCSCI-tot and IRRI-region DTI indices, compared to the DTI indices from other ROIs, was also true for AD ($p = 0.042$) and RD ($p = 0.009$).

We hypothesized that the observed stronger correlation of the IRRI region-derived DTI index values with ISNCSCI-tot may indicate directional contribution from Wallerian degeneration, and that the use of subject-specifically derived DTI indices as a biomarker for the severity of SCI would be affirmed if the degree of individual residual motor or sensory function of patients with SCI could be explained specifically by DTI indices obtained from either the IRRI or SRRI region. To investigate this possibility, we used a stepwise regression analysis. Our data, summarized in Table 5, indicates that the motor score had significant explanatory power for FA_{IRRI} ($p < 0.001$), AD_{IRRI} ($p < 0.01$), and RD_{IRRI} ($p < 0.01$), while neither motor nor sensory scores had significant explanatory power for SRRI-region DTI indices. In addition, we used a stepwise regression analysis to investigate if other factors such as age or TSI could explain changes in the IRRI region-derived DTI indices. Our data, summarized in Table 6, confirms that the level of neurological function assessed by ISNCSCI-tot had significant explanatory power for all three DTI indices (FA_{IRRI} ($p < 0.001$), AD_{IRRI} ($p < 0.05$), RD_{IRRI} ($p < 0.001$)), while age had significant explanatory power for RD_{IRRI} only ($p < 0.05$). TSI had no significant explanatory for any IRRI-region DTI

Table 5　Effect of ISNCSCI motor score and ISNCSCI sensory score on DTI indices obtained from SRRI and IRRI regions

	FA_{SRRI}		AD_{SRRI}		RD_{SRRI}	
	Motor	Sensory	Motor	Sensory	Motor	Sensory
Coefficients	1.30E−03	4.58E−04	−6.18E−04	−4.47E−04	−1.40E−03	−1.40E−03
Standard error	6.35E−04	6.78E−04	1.50E−03	2.60E−03	1.30E−03	2.40E−03
P value	5.31E−02	5.09E−01	6.77E−01	8.67E−01	2.97E−01	5.83E−01
	FA_{IRRI}		AD_{IRRI}		RD_{IRRI}	
	Motor	Sensory	Motor	Sensory	Motor	Sensory
Coefficients	3.00E−03	9.94E−04	−4.80E−03	−9.28E−04	−6.20E−03	2.10E−03
Standard error	6.79E−04	7.90E−04	1.60E−03	7.00E−03	1.60E−03	7.10E−03
P value	<0.001*	2.30E−01	<0.01*	8.96E−01	<0.01*	7.76E−01

Effect of ISNCSCI motor score and sensory score on SRRI and IRRI region DTI indices was investigated using stepwise regression analyses. Motor score had significant explanatory power for IRRI region-derived DTI indices (FA_{IRRI}, AD_{IRRI}, and RD_{IRRI}), while neither motor scores nor sensory scores had significant explanatory power for SRRI region-derived DTI indices (FA_{SRRI}, AD_{SRRI}, and RD_{SRRI})

*Statistically significant ($p < 0.05$; not corrected)

indices. These results confirm that DTI indices measured from the IRRI region, particularly FA_{IRRI} and AD_{IRRI}, are indeed more suitable to serve as non-invasive biomarkers for the severity of SCI and structural improvements in the injured spinal cord independent of age and TSI.

Discussion

DTI tractography can be used to perform semi-automated segmentation of the spinal cord in ways that are effective and reproducible [26], as well as clinically applicable [24]. In this study, we investigated the usage of DTI indices as biomarkers for spinal cord integrity by introducing a subject-specific injury demarcation approach to a previously established segmentation method to define a more biochemically homogeneous ROIs around the injury epicenter.

Subject-specific demarcation of injury regions

Two classes of ROIs—specifically, spinal cord *columns* (right and left lateral, dorsal, and ventral columns) and spinal cord

RRI (SRRI, ERRI, and IRRI regions)—were initially identified. In particular, spinal cord RRIs were identified using a subject-specific ROI placement approach to demarcate individual injury regions, which yielded ROIs that are focal and biochemically homogeneous. Such subject-specific approach can reduce partial voluming of DTI index values within ROIs and enable us to probe the tissues more specifically in relation to SCI. This is supported by the observation that while the spinal cord columns did not have significant effects on either the DTI indices or the degree of correlation between DTI indices and ISNCSCI scores, the spinal cord RRI showed significant effects on all three DTI indices (Table 2)—which suggests that spinal cord RRI is more sensitive to injury severity.

Regional dependence of associations between impairment and diffusion indices

The mean DTI values measured from the entire length of the cervical cord (e.g., FA_{AL}, AD_{AL}, and RD_{AL}) (Table 3) that represents DTI index values obtained using the conventional non-region-specific approach were within the range of values reported in previous studies, for healthy controls [26, 36–39]

Table 6　Effect of time since injury and age

	FA_{IRRI}			AD_{IRRI}			RD_{IRRI}		
	TSI	Age	ISNCSCI total	TSI	Age	ISNCSCI total	TSI	Age	ISNCSCI total
Coefficients	0.000	−0.003	0.002	0.007	0.014	−0.005	0.004	0.015	−0.007
Standard error	0.002	0.001	0.000	0.009	0.007	0.002	0.008	0.007	0.002
P value	0.887	0.067	<0.001*	0.439	0.061	<0.05*	0.600	<0.05*	<0.001*

Stepwise regression analyses were performed to determine the optimal multi-linear model for each indices of interest—specifically FA_{IRRI}, AD_{IRRI}, and RD_{IRRI}. Time since injury (TSI), age, and ISNCSCI-tot score were considered as potential independent variables, and their explanatory power on each DTI index value were tested for significance. ISNCSCI-tot had significant explanatory power for all three DTI indices, while age had significant explanatory power for RD only. TSI had no significant explanatory for all three DTI indices

*Statistically significant ($p < 0.05$; not corrected)

and chronic SCI patients [14, 23]. Studies have shown that axonal and myelin damage that occurs following SCI is associated with decreased FA and increased RD values [11–14]. The significant changes in FA_{AL} and RD_{AL} observed in individuals with chronic SCI (Table 3) are also in agreement with the previous findings. Similarly, the observed significant correlation between functional impairment and the values of the DTI indices is in accordance with previous studies [11, 14, 17, 23], where lower FA and higher AD and RD values are reported to be correlated with worse ISNCSCI scores.

Notably, we observed that compared to FA_{AL}, FA_{IRRI} showed stronger correlation with ISNCSCI-tot, which is in accordance with a previous study [17]—indicating that subject-specific regional measures of FA, and in particular, those measured from IRRI region, may be more specific to impairment. A similar trend of stronger correlations between ISNCSCI-tot and other IRRI-region DTI indices, specifically RD_{IRRI} and AD_{IRRI}, was also observed (Table 4).

Inclusion of the TM patient cohort was intentional, as we expected the proposed method to be applicable to SCI of different etiologies. However, in order to address the question of whether the inclusion of the TM patient data could have introduced any bias to the result, additional analyses were performed on the subset of data comprised exclusively of traumatic SCI individuals, as shown in the Supplemental Materials (Tables S1–S3). The data showed that the results were consistent, irrespective of the inclusion/exclusion of the data from the TM patient cohort—affirming that the proposed method is applicable to SCI of different etiologies.

Wallerian degeneration

Wallerian degeneration describes a secondary anterograde degeneration of axons and myelin sheaths that occurs in regions distal to the primary injury, and identification and characterization of Wallerian degeneration is important for the comprehensive assessment and prognosis of SCI. In spinal cord, Wallerian degeneration is characterized by directionality, as the cord consists of longitudinally arranged major descending motor fibers and ascending sensory fibers—leading to involvement of the mainly ventrolateral motor columns inferior to the primary injury region, and dorsal columns superior to the primary injury region [23, 25, 40, 41]. The directionality observed in the current study (i.e., the high correlation between functional impairment and IRRI-region DTI indices) may therefore indicate that water diffusion measurements in the IRRI region reflect the effects of Wallerian degeneration that are specific to the severity of injury. This is supported in part by the observation that the motor scores displayed significant explanatory power for all three IRRI-region DTI indices (Table 5). However, neither motor nor sensory scores had significant explanatory power for SRRI-region DTI indices (Table 5).

Conventionally, descending motor and ascending sensory columns are defined as ventrolateral and dorsal spinal cord columns, respectively. While extensively adapted in SCI studies by others [23, 42] and us, the definition greatly simplifies the complex structure of the spinal cord. Most noticeably, the above definition of motor and sensory columns disregards the existence of sensory fibers that ascend laterally, such as the spinocerebellar and spinothalamic fibers [43, 44]. Thus, one explanation for the observed lack of correlation of sensory scores with SRRI-region DTI indices, compared to that with IRRI-region DTI indices, may be due to the more distributed nature of the ascending sensory fibers in the spinal cord, which is not fully accounted for in this study. This may also explain the observed lack of significant effect of spinal cord columns on DTI indices (Table 2).

Finally, ISNCSCI sensory scores are ordinal and non-linear, with each dermatome tested and scored as absent (0), abnormal (1), or normal (2). This introduces subjectivity and rater variability into the scoring system and may lower the direct correspondence between objective MRI markers and subjective clinical ones [45, 46]. Alternative measures of residual sensory function with higher sensitivity exist [45, 47, 48], but the methods are often time-consuming and impractical for clinical use. Nonetheless, sensory testing methods with high sensitivity may be used to better understand the relationship between the SRRI-region DTI indices and residual sensory function in individuals with SCI.

Study limitations

Recruitment of individuals with SCI for MRI studies—which require participants to lie still for extended time—is challenging due to their often severe sensorimotor impairments. This greatly limited our ability to recruit a homogeneous cohort of SCI patients—of similar TSI, age, and injury level. Here, we briefly discuss the effects of these potential confounds.

First, previous studies have shown that TSI and age affect the values of DTI indices [38, 49–51]. In order to investigate whether TSI and age had significant effect on DTI indices, we therefore performed a series of stepwise regression analyses. The results showed that ISNCSCI-tot had significant explanatory power ($p < 0.05$; not corrected) on FA_{IRRI}, AD_{IRRI}, and RD_{IRRI}, while TSI and age did not, as shown in Table 6. One exception was the relationship between age and RD_{IRRI}, which was significantly correlated. This observation is consistent with previous findings that RD is more sensitive to the effects of aging, compared to other DTI indices [50, 52]. It is, however, also possible that the effect sizes of TSI and age were too small to be observed in this small-sampled group study. This is supported in part by the decreased amount of correlations (but still in the same direction) between DTI index and ISNCSCI scores observed in the data analysis results

of a sub-group that include only the patients with a traumatic SCI (Tables S1–S3).

Secondly, previous studies have shown that FA values decrease 10–15% along the length of the cervical cord (in C2 to C6 direction), possibly modulated by the varying ratio of gray to white matter in different spinal segmental levels [39]. Therefore, we also investigated the possible effects of such underlying decrease of baseline FA values by weighting the FA_{IRRI} values to reflect the varying injury level in SCI patients (refer to Supplemental Text and Fig. S2 for further description). Figure S2 shows that when adjusted to reflect the varying injury level in SCI patients, the strength of the correlation between FA_{IRRI} and ISNCSCI-tot becomes stronger. This result, while suggesting that the segmental-level-dependent changes in FA may exist in individuals with SCI, also shows compared to the conventional approach that the proposed subject-specific injury demarcation approach can provide robust outcome measures that are more specific to impairments despite possible confound. A possible explanation of this observation is that by no longer diluting the effect of the injury (e.g., 30–40% FA decrease at and around the injury epicenter) across the entire cervical region, the benefit of the subject-specific demarcation approach outweighs the possible confounding effects.

The small size of the study cohort ($n = 18$) limits our ability to utilize the abovementioned confounds (i.e., TSI, age, and level of injury) to derive a multivariate model that better describes the association between the behavioral and DTI outcome measures. A future multi-center study with a larger cohort could help create a more accurate description of the relationship by enabling the inclusion of TSI, age, and the level of injury as covariates in the model.

The small size of the spinal cord was an inherent limitation of this study, leading to increased vulnerability to partial volume effect and motion artifact [53]. At cervical level, the anterior-posterior and transverse diameters of the cervical cord are reported as ca. 8.7–14 mm [54, 55]. This may have contributed to the observed lack of significant effect of spinal cord column on DTI indices (Table 2). One approach for addressing this limitation is to acquire the spinal cord images at higher magnetic field strengths. Our study was performed at 3 T, which provided images with higher SNR and spatial resolution compared to those expected to be provided by 1.5-T magnet, commonly used for clinical diagnostic purposes. As DTI is inherently low in SNR, such benefits of higher field strengths are especially important for DTI, and we expect that the sensitivity and the accuracy of DTI in probing spinal cords microstructures would be even more enhanced in higher field strength (e.g., 7 T). However, trade-offs also exist—that at higher field strengths, chemical shift, susceptibility, and flow/motion artifacts are enhanced—and caution is warranted when analyzing images acquired at higher fields. Another approach would be to acquire higher-resolution images using motion-artifact reducing techniques, such as respiratory and cardiac gating. However, these techniques often require longer scan times that are clinically infeasible for individuals with paralysis. There is also the issue of image misregistration, which is exacerbated by the small cord size. In this study, we used a robust registration scheme utilizing a publically available CATNAP program [31, 56] to minimize the effects of misregistration. Future studies may also benefit from more advanced MR acquisition methods such as accelerated parallel imaging techniques [57, 58].

Finally, CATNAP was also used to perform the tensor estimation by utilizing a multivariate log-linear fitting method. During this process, each DW image and its corresponding vector from the gradient table were entered as unique entries, and no averaging of DW images was performed. The multivariate log-linear fitting method is a simple, yet widely adapted tensor estimation method that has previously been shown to reproducibly estimate DTI-derived indices [31, 59, 60]. It is however a well-known fact that the use of different fitting algorithms such as weighted linear and non-linear least squares can systematically influence the estimation of DTI-derived indices [61]. Consequently, other more robust fitting methods have been proposed over the years to address the issue [61–64]. An interesting area of future research would be to evaluate how different tensor fitting methods impact the precision and accuracy of the DTI-derived indices from impaired spinal cords, and whether more robust fitting methods will yield DTI measures that are even more specific to impairment.

Conclusion

DTI allows for non-invasive assessment of the severity and level of SCI, as well as objective and efficient semi-automated segmentation of the spinal cord. We investigated whether subject-specific demarcation of the injury region, performed using DTI fiber tractography, yields diffusion measures that are more specific to impairment. Results showed that the proposed approach preserved information specific to each individual's injury, and the resulting subject-specific RRIs were a large source of variation for DTI indices. Importantly, IRRI-region DTI indices demonstrated the strongest correlation with impairment, indicating that DTI index measurements from IRRI region have a strong potential to serve as biomarkers for the severity of SCI. Indeed, this correlation suggests that diffusion measures in this region may be more sensitive to Wallerian degeneration in the descending ventrolateral motor columns. We therefore conclude that regional analysis of water diffusion using subject-specific injury demarcation is more specific to impairment, and potentially can have a clinical application in diagnosis of SCI severity and in

measuring anatomical improvements in response to therapeutic interventions.

References

1. Basser PJ, Mattiello J, LeBihan D (1994) Estimation of the effective self-diffusion tensor from the NMR spin echo. J Magn Reson B 103:247–254

2. Pierpaoli C, Jezzard P, Basser PJ, Barnett A, Di Chiro G (1996) Diffusion tensor MR imaging of the human brain. Radiology 201:637–648

3. Beaulieu C (2002) The basis of anisotropic water diffusion in the nervous system—a technical review. NMR Biomed 15:435–455

4. Song SK, Sun SW, Ramsbottom MJ, Chang C, Russell J, Cross AH (2002) Dysmyelination revealed through MRI as increased radial (but unchanged axial) diffusion of water. NeuroImage 17:1429–1436

5. Song SK, Yoshino J, Le TQ, Lin SJ, Sun SW, Cross AH, Armstrong RC (2005) Demyelination increases radial diffusivity in corpus callosum of mouse brain. NeuroImage 26:132–140

6. Smith SA, Golay X, Fatemi A, Jones CK, Raymond GV, Moser HW, van Zijl PC (2005) Magnetization transfer weighted imaging in the upper cervical spinal cord using cerebrospinal fluid as intersubject normalization reference (MTCSF imaging). Magn Reson Med 54:201–206

7. Farrell JA, Zhang J, Jones MV, Deboy CA, Hoffman PN, Landman BA, Smith SA, Reich DS, Calabresi PA, van Zijl PC (2010) Q-space and conventional diffusion imaging of axon and myelin damage in the rat spinal cord after axotomy. Magn Reson Med 63:1323–1335

8. Landman BA, Farrell JA, Smith SA, Reich DS, Calabresi PA, van Zijl PC (2010) Complex geometric models of diffusion and relaxation in healthy and damaged white matter. NMR Biomed 23:152–162

9. Levesque IR, Giacomini PS, Narayanan S, Ribeiro LT, Sled JG, Arnold DL, Pike GB (2010) Quantitative magnetization transfer and myelin water imaging of the evolution of acute multiple sclerosis lesions. Magn Reson Med 63:633–640

10. Choe AS, Stepniewska I, Colvin DC, Ding Z, Anderson AW (2012) Validation of diffusion tensor MRI in the central nervous system using light microscopy: quantitative comparison of fiber properties. NMR Biomed 25:900–908

11. Cheran S, Shanmuganathan K, Zhuo J, Mirvis SE, Aarabi B, Alexander MT, Gullapalli RP (2011) Correlation of MR diffusion tensor imaging parameters with ASIA motor scores in hemorrhagic and nonhemorrhagic acute spinal cord injury. J Neurotrauma 28:1881–1892

12. Klawiter EC, Schmidt RE, Trinkaus K, Liang HF, Budde MD, Naismith RT, Song SK, Cross AH, Benzinger TL (2011) Radial diffusivity predicts demyelination in ex vivo multiple sclerosis spinal cords. NeuroImage 55:1454–1460

13. Mohamed FB, Hunter LN, Barakat N, Liu CS, Sair H, Samdani AF, Betz RR, Faro SH, Gaughan J, Mulcahey MJ (2011) Diffusion tensor imaging of the pediatric spinal cord at 1.5 T: preliminary results. AJNR Am J Neuroradiol 32:339–345

14. Petersen JA, Wilm BJ, von Meyenburg J, Schubert M, Seifert B, Najafi Y, Dietz V, Kollias S (2012) Chronic cervical spinal cord injury: DTI correlates with clinical and electrophysiological measures. J Neurotrauma 29:1556–1566

15. Lundell H, Barthelemy D, Skimminge A, Dyrby TB, Biering-Sorensen F, Nielsen JB (2011) Independent spinal cord atrophy measures correlate to motor and sensory deficits in individuals with spinal cord injury. Spinal Cord 49:70–75

16. Qian W, Chan Q, Mak H, Zhang Z, Anthony MP, Yau KK, Khong PL, Chan KH, Kim M (2011) Quantitative assessment of the cervical spinal cord damage in neuromyelitis optica using diffusion tensor imaging at 3 tesla. J Magn Reson Imaging 33:1312–1320

17. Kim SY, Shin MJ, Chang JH, Lee CH, Shin YI, Shin YB, Ko HY (2015) Correlation of diffusion tensor imaging and phase-contrast MR with clinical parameters of cervical spinal cord injuries. Spinal Cord 53:608–614

18. Chen M, Carass A, Oh J, Nair G, Pham DL, Reich DS, Prince JL (2013) Automatic magnetic resonance spinal cord segmentation with topology constraints for variable fields of view. NeuroImage 83:1051–1062

19. Asman AJ, Smith SA, Reich DS, Landman BA (2013) Robust GM/WM segmentation of the spinal cord with iterative non-local statistical fusion. Med Image Comput Comput Assist Interv 16:759–767

20. Taso M, Le Troter A, Sdika M, Cohen-Adad J, Arnoux PJ, Guye M, Ranjeva JP, Callot V (2015) A reliable spatially normalized template of the human spinal cord—applications to automated white matter/gray matter segmentation and tensor-based morphometry (TBM) mapping of gray matter alterations occurring with age. NeuroImage 117:20–28

21. Samson RS, Ciccarelli O, Kachramanoglou C, Brightman L, Lutti A, Thomas DL, Weiskopf N, Wheeler-Kingshott CA (2013) Tissue- and column-specific measurements from multi-parameter mapping of the human cervical spinal cord at 3 T. NMR Biomed 26:1823–1830

22. Oh J, Saidha S, Chen M, Smith SA, Prince J, Jones C, Diener-West M, van Zijl PC, Reich DS, Calabresi PA (2013) Spinal cord quantitative MRI discriminates between disability levels in multiple sclerosis. Neurology 80:540–547

23. Cohen-Adad J, El Mendili MM, Lehericy S, Pradat PF, Blancho S, Rossignol S, Benali H (2011) Demyelination and degeneration in the injured human spinal cord detected with diffusion and magnetization transfer MRI. NeuroImage 55:1024–1033

24. Choe AS, Belegu V, Yoshida S, Joel S, Sadowsky CL, Smith SA, van Zijl PC, Pekar JJ, McDonald JW (2013) Extensive neurological recovery from a complete spinal cord injury: a

case report and hypothesis on the role of cortical plasticity. Front Hum Neurosci 7:290

25. Cohen-Adad J, Leblond H, Delivet-Mongrain H, Martinez M, Benali H, Rossignol S (2011) Wallerian degeneration after spinal cord lesions in cats detected with diffusion tensor imaging. NeuroImage 57:1068–1076

26. Smith SA, Jones CK, Gifford A, Belegu V, Chodkowski B, Farrell JA, Landman BA, Reich DS, Calabresi PA, McDonald JW, van Zijl PC (2010) Reproducibility of tract-specific magnetization transfer and diffusion tensor imaging in the cervical spinal cord at 3 tesla. NMR Biomed 23:207–217

27. Budzik JF, Balbi V, Le Thuc V, Duhamel A, Assaker R, Cotten A (2011) Diffusion tensor imaging and fibre tracking in cervical spondylotic myelopathy. Eur Radiol 21:426–433

28. Kerkovsky M, Bednarik J, Dusek L, Sprlakova-Pukova A, Urbanek I, Mechl M, Valek V, Kadanka Z (2012) Magnetic resonance diffusion tensor imaging in patients with cervical spondylotic spinal cord compression: correlations between clinical and electrophysiological findings. Spine (Phila Pa 1976) 37:48–56

29. Marino RJ, Ditunno JF Jr, Donovan WH, Maynard F Jr (1999) Neurologic recovery after traumatic spinal cord injury: data from the model spinal cord injury systems. Arch Phys Med Rehabil 80: 1391–1396

30. Maynard FM Jr, Bracken MB, Creasey G, Ditunno JF Jr, Donovan WH, Ducker TB, Garber SL, Marino RJ, Stover SL, Tator CH, Waters RL, Wilberger JE, Young W (1997) International standards for neurological and functional classification of spinal cord injury. American Spinal Injury Association. Spinal Cord 35:266–274

31. Landman BA, Farrell JA, Jones CK, Smith SA, Prince JL, Mori S (2007) Effects of diffusion weighting schemes on the reproducibility of DTI-derived fractional anisotropy, mean diffusivity, and principal eigenvector measurements at 1.5 T. NeuroImage 36:1123–1138

32. Landman BA, Farrell JA, Huang H, Prince JL, Mori S (2008) Diffusion tensor imaging at low SNR: nonmonotonic behaviors of tensor contrasts. Magn Reson Imaging 26:790–800

33. Maes F, Vandermeulen D, Suetens P (1999) Comparative evaluation of multiresolution optimization strategies for multimodality image registration by maximization of mutual information. Med Image Anal 3:373–386

34. Jiang H, van Zijl PC, Kim J, Pearlson GD, Mori S (2006) DtiStudio: resource program for diffusion tensor computation and fiber bundle tracking. Comput Methods Prog Biomed 81:106–116

35. Cohen-Adad J, El Mendili MM, Morizot-Koutlidis R, Lehericy S, Meininger V, Blancho S, Rossignol S, Benali H, Pradat PF (2013) Involvement of spinal sensory pathway in ALS and specificity of cord atrophy to lower motor neuron degeneration. Amyotroph Lateral Scler Frontotemporal Degener 14:30–38

36. Clark CA, Werring DJ (2002) Diffusion tensor imaging in spinal cord: methods and applications—a review. NMR Biomed 15:578–586

37. Ducreux D, Fillard P, Facon D, Ozanne A, Lepeintre JF, Renoux J, Tadie M, Lasjaunias P (2007) Diffusion tensor magnetic resonance imaging and fiber tracking in spinal cord lesions: current and future indications. Neuroimaging Clin N Am 17:137–147

38. Mamata H, Jolesz FA, Maier SE (2005) Apparent diffusion coefficient and fractional anisotropy in spinal cord: age and cervical spondylosis-related changes. J Magn Reson Imaging 22:38–43

39. Wheeler-Kingshott CA, Hickman SJ, Parker GJ, Ciccarelli O, Symms MR, Miller DH, Barker GJ (2002) Investigating cervical spinal cord structure using axial diffusion tensor imaging. NeuroImage 16:93–102

40. Buss A, Pech K, Merkler D, Kakulas BA, Martin D, Schoenen J, Noth J, Schwab ME, Brook GA (2005) Sequential loss of myelin proteins during Wallerian degeneration in the human spinal cord. Brain 128:356–364

41. Qian J, Herrera JJ, Narayana PA (2010) Neuronal and axonal degeneration in experimental spinal cord injury: in vivo proton magnetic resonance spectroscopy and histology. J Neurotrauma 27: 599–610

42. Xu J, Shimony JS, Klawiter EC, Snyder AZ, Trinkaus K, Naismith RT, Benzinger TL, Cross AH, Song SK (2013) Improved in vivo diffusion tensor imaging of human cervical spinal cord. NeuroImage 67:64–76

43. Willis WD Jr (2007) The somatosensory system, with emphasis on structures important for pain. Brain Res Rev 55:297–313

44. Rub U, Schultz C, Del Tredici K, Gierga K, Reifenberger G, de Vos RA, Seifried C, Braak H, Auburger G (2003) Anatomically based guidelines for systematic investigation of the central somatosensory system and their application to a spinocerebellar ataxia type 2 (SCA2) patient. Neuropathol Appl Neurobiol 29:418–433

45. Hayes KC, Wolfe DL, Hsieh JT, Potter PJ, Krassioukov A, Durham CE (2002) Clinical and electrophysiologic correlates of quantitative sensory testing in patients with incomplete spinal cord injury. Arch Phys Med Rehabil 83:1612–1619

46. Steeves JD, Lammertse D, Curt A, Fawcett JW, Tuszynski MH, Ditunno JF, Ellaway PH, Fehlings MG, Guest JD, Kleitman N, Bartlett PF, Blight AR, Dietz V, Dobkin BH, Grossman R, Short D, Nakamura M, Coleman WP, Gaviria M, Privat A, International Campaign for Cures of Spinal Cord Injury Paralysis (2007) Guidelines for the conduct of clinical trials for spinal cord injury (SCI) as developed by the ICCP panel: clinical trial outcome measures. Spinal Cord 45:206–221

47. Finnerup NB, Johannesen IL, Fuglsang-Frederiksen A, Bach FW, Jensen TS (2003) Sensory function in spinal cord injury patients with and without central pain. Brain 126:57–70

48. Ellaway PH, Catley M (2013) Reliability of the electrical perceptual threshold and Semmes-Weinstein monofilament tests of cutaneous sensibility. Spinal Cord 51:120–125

49. Kumar R, Chavez AS, Macey PM, Woo MA, Harper RM (2013) Brain axial and radial diffusivity changes with age and gender in healthy adults. Brain Res 1512:22–36

50. Davis SW, Dennis NA, Buchler NG, White LE, Madden DJ, Cabeza R (2009) Assessing the effects of age on long white matter tracts using diffusion tensor tractography. NeuroImage 46:530–541

51. Kennedy MR, Wozniak JR, Muetzel RL, Mueller BA, Chiou HH, Pantekoek K, Lim KO (2009) White matter and neurocognitive changes in adults with chronic traumatic brain injury. J Int Neuropsychol Soc 15:130–136

52. Giorgio A, Watkins KE, Douaud G, James AC, James S, De Stefano N, Matthews PM, Smith SM, Johansen-Berg H (2008) Changes in white matter microstructure during adolescence. NeuroImage 39:52–61

53. Kharbanda HS, Alsop DC, Anderson AW, Filardo G, Hackney DB (2006) Effects of cord motion on diffusion imaging of the spinal cord. Magn Reson Med 56:334–339

54. Sherman JL, Nassaux PY, Citrin CM (1990) Measurements of the normal cervical spinal cord on MR imaging. AJNR Am J Neuroradiol 11:369–372

55. Sigmund EE, Suero GA, Hu C, McGorty K, Sodickson DK, Wiggins GC, Helpern JA (2011) High-resolution human cervical spinal cord imaging at 7 T. NMR Biomed 25:891–899

56. Farrell JA, Landman BA, Jones CK, Smith SA, Prince JL, van Zijl PC, Mori S (2007) Effects of signal-to-noise ratio on the accuracy and reproducibility of diffusion tensor imaging-derived fractional anisotropy, mean diffusivity, and principal eigenvector measurements at 1.5 T. J Magn Reson Imaging 26:756–767

57. Cohen-Adad J, Mareyam A, Keil B, Polimeni JR, Wald LL (2011) 32-channel RF coil optimized for brain and cervical spinal cord at 3 T. Magn Reson Med 66:1198–1208

58. Tsuchiya K, Fujikawa A, Suzuki Y (2005) Diffusion tractography of the cervical spinal cord by using parallel imaging. AJNR Am J Neuroradiol 26:398–400

59. Kumar M, Gupta RK, Saksena S, Behari S, Malik GK, Kureel SN, Pandey CM, Rathore RK (2010) A diffusion tensor imaging study of deep gray and white matter brain maturation differences between patients with spina bifida cystica and healthy controls. J Clin Neurosci 17:879–885

60. Saksena S, Husain N, Malik GK, Trivedi R, Sarma M, Rathore RS, Pandey CM, Gupta RK (2008) Comparative evaluation of the cerebral and cerebellar white matter development in pediatric age group using quantitative diffusion tensor imaging. Cerebellum 7:392–400

61. Lanzafame S, Giannelli M, Garaci F, Floris R, Duggento A, Guerrisi M, Toschi N (2016) Differences in Gaussian diffusion tensor imaging and non-Gaussian diffusion kurtosis imaging model-based estimates of diffusion tensor invariants in the human brain. Med Phys 43:2464

62. Veraart J, Van Hecke W, Sijbers J (2011) Constrained maximum likelihood estimation of the diffusion kurtosis tensor using a Rician noise model. Magn Reson Med 66:678–686

63. Veraart J, Sijbers J, Sunaert S, Leemans A, Jeurissen B (2013) Weighted linear least squares estimation of diffusion MRI parameters: strengths, limitations, and pitfalls. NeuroImage 81: 335–346

64. Koay CG, Chang LC, Carew JD, Pierpaoli C, Basser PJ (2006) A unifying theoretical and algorithmic framework for least squares methods of estimation in diffusion tensor imaging. J Magn Reson 182:115–125

RESEARCH ARTICLE

Reproducibility and Temporal Structure in Weekly Resting-State fMRI over a Period of 3.5 Years

Ann S. Choe[1,2,3]*, Craig K. Jones[1,2], Suresh E. Joel[1,2], John Muschelli[4], Visar Belegu[3,5], Brian S. Caffo[4], Martin A. Lindquist[4], Peter C. M. van Zijl[1,2], James J. Pekar[1,2]

1 Russell H. Morgan Department of Radiology and Radiological Science, Johns Hopkins University School of Medicine, Baltimore, MD, United States of America, 2 F. M. Kirby Research Center for Functional Brain Imaging, Kennedy Krieger Institute, Baltimore, MD, United States of America, 3 International Center for Spinal Cord Injury, Kennedy Krieger Institute, Baltimore, MD, United States of America, 4 Department of Biostatistics, Bloomberg School of Public Health, Johns Hopkins University, Baltimore, MD, United States of America, 5 Department of Neurology, Johns Hopkins University School of Medicine, Baltimore, MD, United States of America

* annschoe@gmail.com

Abstract

Resting-state functional MRI (rs-fMRI) permits study of the brain's functional networks without requiring participants to perform tasks. Robust changes in such resting state networks (RSNs) have been observed in neurologic disorders, and rs-fMRI outcome measures are candidate biomarkers for monitoring clinical trials, including trials of extended therapeutic interventions for rehabilitation of patients with chronic conditions. In this study, we aim to present a unique longitudinal dataset reporting on a healthy adult subject scanned weekly over 3.5 years and identify rs-fMRI outcome measures appropriate for clinical trials. Accordingly, we assessed the reproducibility, and characterized the temporal structure of, rs-fMRI outcome measures derived using independent component analysis (ICA). Data was compared to a 21-person dataset acquired on the same scanner in order to confirm that the values of the single-subject RSN measures were within the expected range as assessed from the multi-participant dataset. Fourteen RSNs were identified, and the inter-session reproducibility of outcome measures—network spatial map, temporal signal fluctuation magnitude, and between-network connectivity (BNC)–was high, with executive RSNs showing the highest reproducibility. Analysis of the weekly outcome measures also showed that many rs-fMRI outcome measures had a significant linear trend, annual periodicity, and persistence. Such temporal structure was most prominent in spatial map similarity, and least prominent in BNC. High reproducibility supports the candidacy of rs-fMRI outcome measures as biomarkers, but the presence of significant temporal structure needs to be taken into account when such outcome measures are considered as biomarkers for rehabilitation-style therapeutic interventions in chronic conditions.

Introduction

Functional magnetic resonance imaging (fMRI) can noninvasively reveal the functional organization of the human brain, even in the absence of explicit tasks. Referred to as resting-state functional MRI (rs-fMRI), the method exploits synchronous fluctuations in blood oxygen level dependent (BOLD) signal throughout intrinsic brain functional networks [1]. The ability to study the brain's functional networks without requiring participants to perform explicit tasks has clinical appeal, as it allows use of an identical protocol for all patients, regardless of cognitive or physical limitations. This is especially important in chronic conditions that affect motor function, and the need for non-invasive and reproducible biomarkers is enhanced by advances in long-term therapeutic interventions for such chronic conditions [2–5]. Further, robust changes in resting state networks (RSNs) have been observed in chronic diseases such as spinal cord injury [6], cerebral palsy [4,5], Parkinson's disease [7,8], multiple sclerosis [9,10], and stroke [11], indicating that rs-fMRI based network outcome measures have the potential to serve as biomarkers for chronic diseases and their progression, as well as the effects of possible therapeutics.

Here we report the use of a unique longitudinal dataset that covers the time span of 185 weeks with weekly repeat measures. The dataset is exceptional in its length and frequency of acquisition and provides a unique opportunity to gain insight into two different aspects of rs-fMRI derived measures that were previously not accessible: 1) the reproducibility of the RSN outcome measures over an extended time period relevant for long-term clinical trials, and 2) inter-session temporal characteristics of the multi-year time courses of the rs-fMRI based outcome measures, provided through time series analysis.

In this study, we aimed to: 1) present the unique longitudinal dataset reporting on a healthy adult subject scanned weekly over 3.5 years, 2) identify RSN outcome measures appropriate for clinical trials, with high intra-subject inter-session reproducibility over an extended timeframe, and 3) identify potential parameters-of-interest by assessing the existence of temporal structure within RSN outcome measure time courses. To achieve these goals, we first investigated the intra-subject inter-session reproducibility of independent component analysis (ICA)-derived rs-fMRI outcome measures, namely network spatial maps, BOLD temporal signal fluctuation magnitudes, and temporal correlations between pairs of functional networks (between-network connectivity; BNC). We then performed time series analysis on the time courses of the RSN outcome measures to assess their temporal structure.

The RSN outcome measures were stable over the period of 185 weeks, with executive RSNs showing the highest reproducibility. Significant trend, annual periodicity, and persistence existed in the time courses of the outcome measures, suggesting that when such outcome measures are considered as biomarkers for rehabilitation-style therapeutic interventions in chronic conditions, it may be beneficial to take into consideration the temporal structure of the outcome measure.

Material and Methods

Participants

The longitudinal single-subject dataset was acquired from a healthy volunteer (40 years of age at time of initial scan; male). A total of 158 sessions of MRI data was acquired on a weekly basis, over a span of 185 weeks. Scans were typically performed on Thursday mornings at 11:30am; in cases of scheduling conflicts, scans were performed on different days of the week and/or times, or skipped, depending on the types of conflicts. The initial image acquisition was performed on the 7th of December, 2009, and the last image acquisition was performed on the

20th of June, 2013. Acquisition dates for each session as well as the dates of the missed scans are reported in the S1 Table.

A publically available multi-participant dataset [12] (referred to as "Kirby-21"; available at http://www.nitrc.org/projects/multimodal), which was acquired using the same rs-fMRI imaging protocol on the same MRI scanner, was used in order to confirm that the values of the single-subject RSN measures are within the expected range as assessed from the multi-participant dataset. The multi-participant dataset is from 21 healthy volunteers (22–61 years, mean 32 years, Male/Female ratio: 11/10).

In order to distinguish the study participant of the longitudinal single-subject study from the participants of the Kirby-21 study, the former will be referred as "the subject" from this point on. The term "participants" will be used inclusively to refer to study participants from both single- and multi-participant studies.

Both the longitudinal single-subject and multi-participant Kirby-21 studies were performed under protocols approved by the Institutional Review Board at Johns Hopkins University School of Medicine. Signed informed consents were obtained from all study participants of the studies.

Image Acquisition

All participants were scanned on a 3T Philips Achieva scanner (Philips HealthCare, Best, Netherlands).

T1 weighted (T1w) MPRAGE (Magnetization-Prepared Rapid Acquisition Gradient Echo) structural scans were acquired for each session (acquisition time = 6 min, TR/TE/TI = 6.7/3.1/842 ms, resolution = 1x1x1.2 mm^3, SENSE factor = 2, flip angle = 8°).

Rs-fMRI data of the subject was acquired using a multi-slice SENSE-EPI pulse sequence [13,14] with TR/TE = 2000/30 ms, SENSE factor = 2, flip angle = 75°, 37 axial slices, nominal resolution = 3x3x3 mm^3, 1 mm gap, 16 channel neuro-vascular coil, number of dynamics (frames) per run = 200. Identical imaging parameters were used to acquire the Kirby-21 rs-fMRI data [12], except for the number of dynamics per run, which was 210. Only the first 200 dynamics of the multi-participant data were analyzed, in order to match the length of the runs with the single-subject data. One of the 21 healthy volunteer dataset was identified to include excess motion and was excluded from further data analysis. The rs-fMRI scans were always acquired after the T1w scans, to allow participants to get acclimated to the noise and environment inside the scanner. Participants were instructed to stay as still as possible with their eyes closed during the entire scan, and no other instruction was provided.

Data Processing

Preprocessing of the rs-fMRI datasets was performed using SPM8 (http://www.fil.ion.ucl.ac.uk/spm) [15] and Matlab (Natick, MA). The preprocessing pipeline included: 1) slice timing correction, used to correct differences in image acquisition time between image slices, 2) motion correction, 3) co-registration, used to align structural images to functional images, 4) unified segmentation-normalization [16], used to transform functional images to normalized Montreal Neurological Institute (MNI) space (2x2x2 mm^3), 5) high pass filtering with 0.01 Hz cutoff, used to eliminate slowly varying background noise and effects of scanner drift, and 6) spatial smoothing using 6 mm full-width at half-maximum Gaussian kernel (*i.e.*, twice the nominal size of the rs-fMRI acquisition voxel), used to suppress noise and reduce effects of imperfect normalization.

Group ICA of fMRI toolbox (GIFT) software (http://mialab.mrn.org/software/gift) [17] was used to perform group independent component analysis (GICA) [18]. Single- and multi-

participant datasets were combined, and two steps of principal component analysis (PCA) data reduction were performed for group level analysis, where individual session data were first reduced to 70 principal components. The reduced data was then concatenated in the temporal direction and further reduced to 35 principal components.

Estimation of the number of independent components (*i.e.*, 35) was guided by order selection using the minimum description length (MDL) criterion [19]. The dimensionality of the individual session PCA data reduction (*i.e.*, 70) was set by doubling the estimated component number, to ensure robust backreconstruction [20,21] following the ICA decomposition.

ICA [22] is one of the most commonly used methods for analyzing rs-fMRI data. It models the data as a linear mixture of signals originating from spatially-independent sources, and then estimates the sources by maximizing their independence [23]. These sources include not only the spontaneous fluctuations in BOLD signals in functional networks, but also "nuisance" signals such as those arising from head motion, respiration, and cardiac pulsations. Later, these nuisance components are eliminated and only sources identified as RSNs are retained for further analysis. One of the biggest advantages of the method is that it allows the analysis of rs-fMRI data without *a priori* knowledge of the sources [18,24]. In this study, ICA was performed using the InfoMax algorithm [22], and the process yielded a total of 35 aggregate independent component (IC) spatial maps and associated time courses. Single-session maps for each session (single-subject) and participant (multi-participant) were obtained using backreconstruction [18] via the "GICA3" procedure [20]. A flowchart that visualizes the details of the preprocessing and GICA steps is presented as S1 Fig.

RSNs were identified manually from the 35 ICs estimated. Three were rejected due to low reliability of the ICs as assessed using the ICASSO toolbox [25]. The spatial distribution (*i.e.*, grey matter vs. white matter and cerebral spinal fluid) and temporal frequency power distribution of the remaining 32 ICs were manually assessed, and 18 ICs were eliminated as representing non-neuronal sources such as head motion, respiration, and cardiac pulsations—specifically, the peak activations of the networks were required to be within the gray matter, and RSN spatial maps were required to have low overlap with vascular and ventricular regions. Motion artifact components that display high intensity values around the edges of the brain were also identified and eliminated.–The process identified the remaining 14 ICs as RSNs that represent unique functional networks.

Resting State Network Outcome Measures

The reproducibility and temporal structure (trend, annual periodicity, and persistence) were assessed for three types of RSN outcome measures: spatial similarity of RSN maps, temporal signal fluctuation magnitude, and BNC.

Spatial similarity of RSN maps. The spatial similarity of each week's RSN spatial maps to the group mean map, as calculated using η^2 [26], was obtained as an outcome measure. First, the single-session RSN maps for each week were obtained through backreconstruction of the aggregate maps, and converted to z-score using Fisher's r-to-z transformation [18,20]. A given voxel's value in each RSN maps, therefore, represents the weight of the RSN time course with respect to the measured relative BOLD signal. The similarity measure η^2 [26–28] was defined as:

$$\eta^2 = 1 - \frac{\sum_{i=1}^{n} (a_i - m_i)^2 + (b_i - m_i)^2}{\sum_{i=1}^{n} (a_i - \bar{M})^2 + (b_i - \bar{M})^2} \tag{1}$$

Page | 55

where i represent voxel index within a brain, n is number of voxels in a brain, a_i and b_i are the values at position i in maps a and b, respectively, m_i is the mean value of the two images at position i, and $\bar{M}$ is the grand mean across the mean image m. η^2 values can range from 0 to 1, where 0 indicates no similarity between two images, and 1 indicates that two images are identical.

By calculating the fraction of the variance in one image accounted for by variance in a second image, η^2 reports on the difference in the values at corresponding points in the two images. One of the biggest advantages of η^2 is that it allows the quantification of differences/similarity of the two images instead of the correlational relationship between them [26].

Finally, for each network, a spatial overlap map [29] was created in order to provide visual means to assess the repeatability of the single-session RSN maps. The process first involved thresholding (z-score > 1) of the single session maps to obtain voxels most representative of each RSN. The resulting binary maps were subsequently summed, and then normalized by dividing the maps by the total number of image acquisition, and multiplying by 100 to convert to percentage.

Temporal fluctuation magnitude of RSN time courses. The magnitude of temporal signal fluctuations for each RSN was calculated as the quadratic mean (root mean square; RMS) of the backreconstructed time courses that were scaled to the original data to represent percent signal change [18,20].

Between-network connectivity of RSN time courses. BNC, a measure of synchrony between RSNs, was computed for each session as the Pearson correlation coefficient of the network time courses [30,31].

Analysis of RSN Outcome Measures over Sessions

Reproducibility. The intra-class correlation (ICC), a metric of test-retest reliability, is widely used in the rs-fMRI reproducibility literature. However, the ICC cannot be used for the present study, which is a longitudinal case report, because there is no 'class' (or group) of subjects who underwent 3.5 years of weekly scanning. Instead, for each type of RSN outcome measure (*i.e.*, spatial similarity of RSN maps, temporal fluctuation magnitude, and BNC), intra-subject inter-session reproducibility was characterized using coefficient of variation (CV), defined as the ratio of standard deviation (SD) to mean, expressed in percentage. CV enables the comparison of data sets with different means, by providing a standardized measure of dispersion. However, the calculated CV can appear artificially inflated if a mean value of a data set is close to zero. Therefore, in order to help keep things in perspective, we also report corresponding SD values.

Time series analysis—trend, annual periodicity, and persistence. The single-subject, multi-year acquisition of the longitudinal rs-fMRI dataset enabled time series analysis of weekly RSN outcome measures and observation of their temporal structure (trend, annual periodicity, and persistence) over the extended time period.

Existence of linear trends in the weekly RSN outcome measures was tested using general linear model. Significance of the trend was tested using F statistics, and each outcome measure's p-value was adjusted for multiple comparisons using false discovery rate (FDR) correction for the number of tested RSNs.

Recognizing that changes in degree of subject motion as well as changes in signal intensity due to variable scanning environment over time may introduce linear trends not of neurological origin, the degree of subject motion over each session over the 185 weeks period was assessed to identify potential confounds. A quantitative measure of subject motion was provided by frame-wise displacement (FD) [32], which was calculated by summing the absolute

value of the three differenced translational realignment parameters and the three differenced rotational parameters, which were converted from radians to millimeters by assuming a brain radius of 50 mm.

Additionally, potential changes in signal intensity arising from a variable scanning environment were assessed using a dataset from a concurrent ongoing phantom stability scan within the F.M. Kirby Research Center. The study was run by placing a 15 cm diameter silicone oil filled sphere "phantom" in a 32 channel head coil and running gradient-echo echo-planar imaging (EPI) scans (TR/TE = 3000/40ms, 20 axial slices, imaging matrix: 64x64, field of view: 230 x 230 mm, 3mm slice thickness, 1 mm gap, 300 dynamics) [33], which is equivalent to running a rs-fMRI scan. Signal intensity of the phantom from the corresponding weeks was calculated, and a weekly signal intensity measure was constructed for detection of any linear trend. To prevent reporting of spurious results, permutation tests with 1000 iterations were performed.

The significance of the spectral peaks at 0.0192 weeks^{-1} (annual periodicity; 1/52.18 weeks) in the RSN outcome measures was tested using a procedure for finding spectral peaks in time series described by Ahdesmaki et al [34,35] at $p < 0.05$, after FDR correction for the number of tested RSNs. The robust detection method uses Fisher's g-test for the detection of periodic fluctuations in multiple time courses. The method also incorporates regression based methods to find the spectral estimate of a time course instead of using the basic periodogram, allowing robust estimation of spectral peaks in non-uniformly sampled data with unknown noise characteristics. This makes the method especially appropriate for the 185 weeks dataset (with 158 time points) described in this study. We refer readers to the above mentioned references for further details of the detection method. The seasonal effect on RSN outcome measures was also investigated by correlating the RSN outcome measure time courses with the recorded daily maximum temperature of Baltimore (freely distributed by the National Oceanic and Atmospheric Administration (NOAA); www.noaa.gov). To prevent reporting of spurious results, permutation tests with 1000 iterations were performed.

Finally, existence of autocorrelation within the RSN outcome measures was assessed by estimating the autoregressive moving average (ARMA) models of the weekly RSN outcome measures using automatic spectral analysis [36,37]. As with the robust spectral peak detection method used to observe annual periodicity, the method is specifically designed to account for non-uniformly sampled data with unknown noise characteristics. ARMA model is estimated in two parts, through separate estimation of the autoregressive (AR) and moving average (MA) models. Traditional ARMA model estimation algorithms often utilize maximum likelihood (ML) approach for both the AR and MA model estimations. However, the ML approach is known to provide poor estimates of the MA model when there are missing data. We therefore utilize the automatic spectral analysis method, which uses reduced statistics algorithm [36,37] to improve estimates of MA model.

Results

Functional Networks

Fourteen RSNs were identified: auditory network (Aud), ventral and dorsal sensorimotor networks (Smot-ven, Smot-dor), two visual networks (Vis-a, Vis-b; arbitrarily labeled), three default mode networks (DMN; DMN-a, DMN-b, DMN-c; arbitrarily labeled), ventral and dorsal attention networks (Attn-ven, Attn-dor), left and right executive-function networks (Exec-L, Exec-R), a salience network (Sal), and a cerebellar network (Cb). Fig 1 shows aggregate spatial maps of the 14 RSNs in representative sagittal, coronal, and axial views.
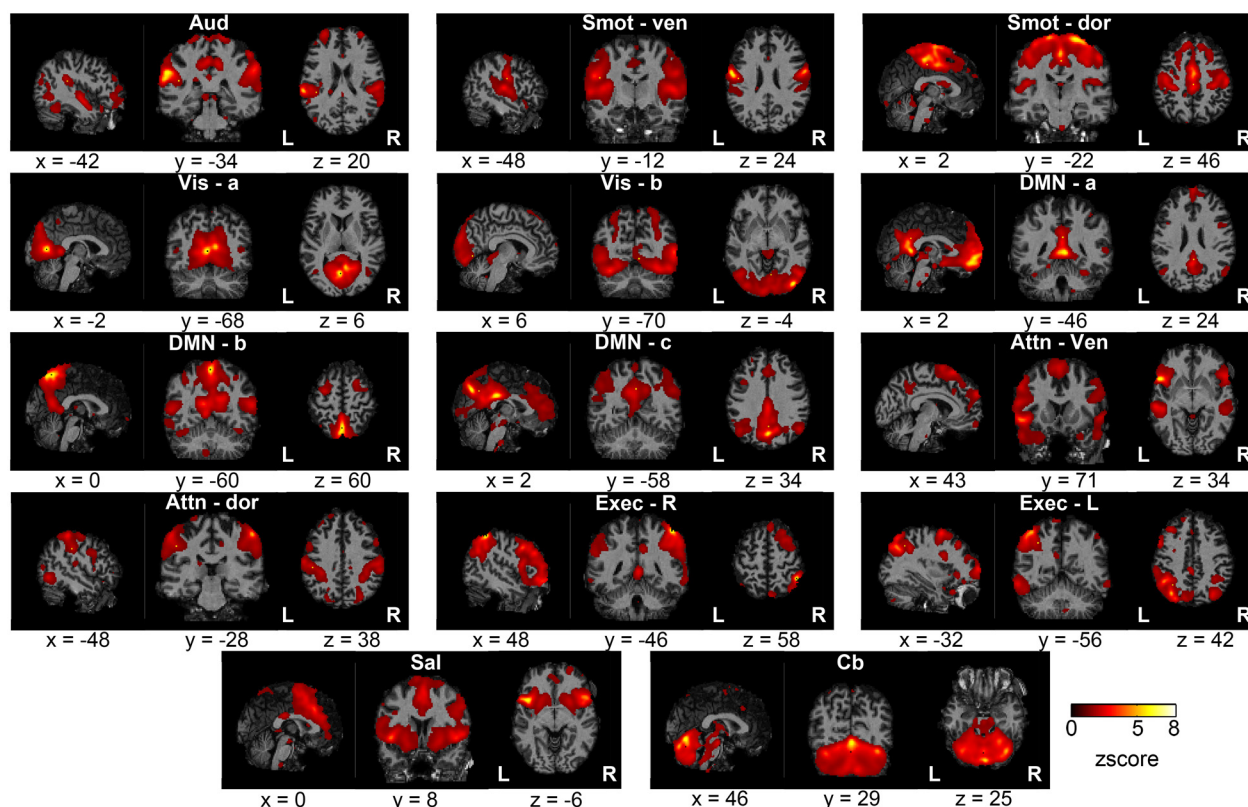
Fig 1. Aggregate spatial maps of the resting state networks (RSNs). Group independent component analysis (GICA) was used to estimate the RSNs and obtain the aggregate spatial maps. The spatial maps of each RSN are shown as subfigures, with representative sagittal, coronal, and axial views (left-to-right) overlaid on structural images within the Montreal Neurological Institute (MNI) template space; coordinates (in mm) for each view are indicated below each subfigure. (Aud: auditory, Smot: seonsorimotor, Vis: visual, DMN: default mode network, Attn: attention, Exec: executive, Sal: salience, Cb: cerebellar, ven: ventral, dor: dorsal, R: right, L: left).

doi:10.1371/journal.pone.0140134.g001

Reproducibility

Spatial similarity of RSN maps. Backreconstructed, single-session RSN spatial maps from representative imaging sessions and the mean spatial maps of the 14 RSNs are shown in the middle and leftmost column of Fig 2, respectively. Spatial overlap maps, whose values within each voxel represent the fraction of the time the voxel is categorized as a member of the corresponding RSN, are shown in the rightmost columns of Fig 2. Each overlap map showed good agreement with the corresponding group mean spatial map.

Reproducibility of the spatial map similarity measure for both single- and multi-participant datasets is presented using violin plots (Fig 3). For visualization purposes, the violin plots were sorted based on the interquartile range of the single-subject data.

For each RSN, the degree of spatial similarity of the single-subject dataset's backreconstructed spatial maps to the group mean map was found to be high, with mean η^2 values ranging from 0.747 to 0.841 (Fig 3, Table 1). Also, for all RSNs, the median (second quartile) η^2 values of the single-subject dataset were within the range of η^2 values of the multi-participant dataset.

The two visual networks (Vis-a and Vis-b) and a sensorimotor network (Smot-dor) showed the lowest intra-subject inter-session reproducibility, with CV values of 6.68, 4.86, and 4.75%, while the executive networks (Exec-R and Exec-L) showed the highest reproducibility, with CV values of 1.60 and 1.65% (Table 1). Similarly, the sensorimotor network (Smot-ven) and visual
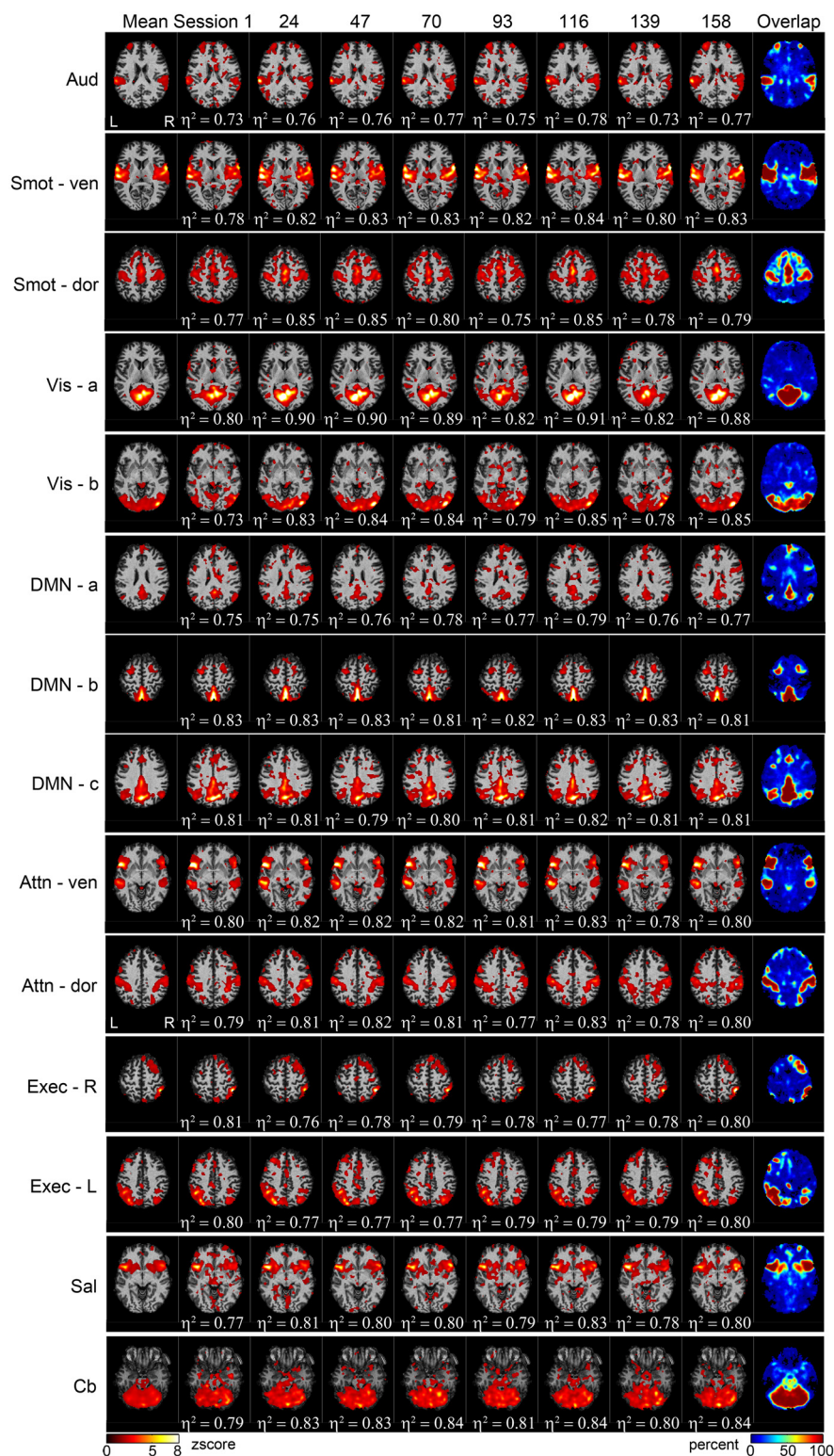
Fig 2. RSN spatial maps for representative weekly sessions. RSN mean spatial maps (leftmost column), representative backreconstructed weekly single-session spatial maps (middle eight columns), and overlap maps (rightmost column) for the 14 RSNs. The degree of spatial similarity of each session's spatial map to the corresponding mean map, as measured using eta-squared (η^2), is indicated below the single-session maps.

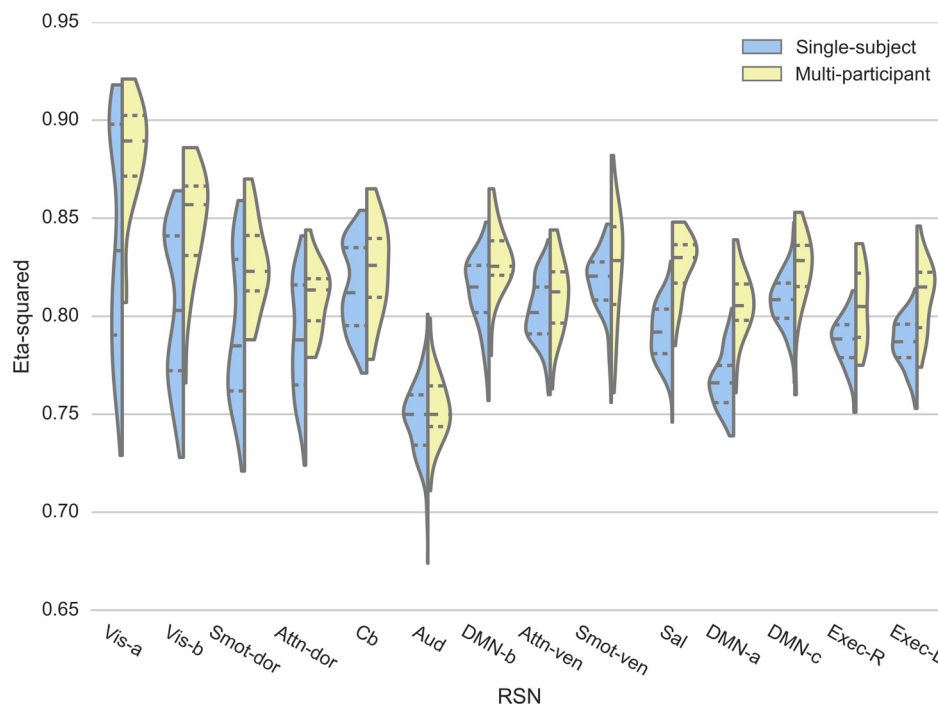doi:10.1371/journal.pone.0140134.g002

Fig 3. Reproducibility of RSN spatial maps. Spatial similarity of each session's RSN spatial map to the corresponding group mean map, measured using eta-squared (η^2), for single-subject (blue) and multi-participant (yellow) datasets, is visualized using violin plots. The first, second, and third quartiles of the data are represented within the violin plots as dotted lines.

doi:10.1371/journal.pone.0140134.g003

(Vis-b, and Vis-a) networks were also the least reproducible (intra-subject inter-session reproducibility; CV = 3.72, 3.54, 3.44%, respectively) for the multi-participant dataset. Sal network showed the highest inter-subject reproducibility (CV = 1.91%).

A test of equal variance (f-test) indicated that Smot-ven network showed higher intra-subject inter-session spatial map reproducibility compared to its inter-participant reproducibility ($p < 0.05$, corrected; Table 1). The Vis-a network, on the other hand, showed an opposite trend; intra-subject inter-session reproducibility was significantly lower than the inter-participant reproducibility ($p < 0.05$, corrected; Table 1). The higher intra-subject inter-session spatial map reproducibility for the Smot-ven network was preserved when the same analysis was performed using only the first twenty sessions of the single-subject data, matching the multi-participant dataset's number of sessions (not reported separately to avoid overlap). Such was not the case for the Vis-a network; while the trend of lower intra-subject inter-session spatial map reproducibility was still observed, the difference was no longer significant.

Temporal fluctuation magnitude of RSN time courses. Reproducibility of the RMS % BOLD value for each session's backreconstructed time course for both the single- and multi-participant datasets are presented using violin plots in Fig 4. For visualization purposes, the violin plots were sorted based on the interquartile range of the single-subject data.

The single-subject, median temporal signal fluctuation magnitude of each RSN, was within the range of temporal signal fluctuation magnitude values of the same RSNs within the multi-participant dataset, as shown in Fig 4. Also, the ranges of the mean temporal signal fluctuation magnitude for the single- and multiple-participant dataset were similar—from 0.454% to 2.02% and 0.716% to 2.282%, respectively (Table 2).

Table 1. Reproducibility of resting state network (RSN) spatial maps.

RSN	Spatial similarity (η^2) to group mean map					
	Single-subject			Multi-participant		
	mean	SD	CV¶	mean	SD	CV
Exec-R	0.786	0.0126	1.60	0.810	0.0183	2.26
Exec-L	0.787	0.0130	1.65	0.806	0.0195	2.42
DMN-c	0.808	0.0138	1.70	0.824	0.0210	2.55
DMN-a	0.767	0.0145	1.89	0.805	0.0177	2.20
Sal	0.792	0.0152	1.91	0.826	0.0166	2.01
Smot-ven	0.817	0.0162	1.98	0.824	0.0306	3.72
Attn-ven	0.802	0.0165	2.05	0.811	0.0203	2.50
DMN-b	0.813	0.0185	2.27	0.828	0.0186	2.25
Aud	0.747	0.0185	2.48	0.753	0.0190	2.52
Cb	0.814	0.0218	2.68	0.824	0.0239	2.90
Attn-dor	0.789	0.0289	3.66	0.809	0.0175	2.16
Smot-dor	0.792	0.0376	4.75	0.826	0.0232	2.81
Vis-b	0.804	0.0391	4.86	0.847	0.0300	3.54
Vis-a	0.841	0.0562	6.68	0.882	0.0304	3.44

¶ Sorting column/variable.

The mean, standard deviation (SD), and coefficient of variation (CV) values for each RSN are shown for the single- and multi-participant datasets. (Aud: auditory, Smot: seonsorimotor, Vis: visual, DMN: default mode network, Attn: attention, Exec: executive, Sal: salience, Cb: cerebellar, ven: ventral, dor: dorsal, R: right, L: left)

For the single-subject dataset, the DMN-a and Smot-dor networks showed the lowest intra-subject inter-session reproducibility over time, with CV values of 85.8 and 68.4%, respectively, while the Exec-L and Exec-R networks showed the highest reproducibility over time, with CV values of 24.5 and 25.0%, respectively (Table 2). For the multi-participant dataset, Aud and Cb networks showed the lowest inter-participant reproducibility with CV values of 111.4 and 101%, respectively, and Attn-dor and Attn-ven networks had the highest reproducibility, with CV values of 37.7 and 38.7%, respectively.

Test of equal variance (f-test) between the single-subject and multi-participant dataset indicated higher intra-subject inter-session reproducibility of temporal fluctuation magnitude, with eight RSN networks (Exec-L, Exec-R, DMN-c, Smot-ven, aud, Vis-b, Cb, and Sal networks) showing significantly higher intra-subject inter-session reproducibility. In contrast, only two RSN networks (Smot-dor and DMN-a) showed significantly lower intra-subject inter-session reproducibility of the networks (Table 2; $p < 0.05$, corrected). In order to ensure that such high intra-subject inter-session reproducibility is not solely due to the larger sample size of the single-subject dataset, reproducibility was also calculated using the first twenty sessions from the single-subject dataset (not reported separately). The observation was consistent, with six of the eight RSNs (Exec-L, Exec-R, DMN-b, DMN-c, Smot-ven, Aud, and Cb) still showing significantly higher intra-subject inter-session reproducibility (f-test; $p < 0.05$, corrected)

Between-network connectivity of RSNs. Mean BNC values for the single-subject dataset ranged from -0.133 (Sal/DMN-a) to 0.660 (Aud/Smot-ven), and from -0.104 (Sal/DMN-a) to 0.606 (Vis-a/Vis-b) for the multi-participant dataset (Table 3, S2 Table). The top ten RSN pairs with the largest mean BNC values for the single- and multi-participant datasets are reported in Table 3. There was a significant overlap between the top ten lists from the single- and multi-
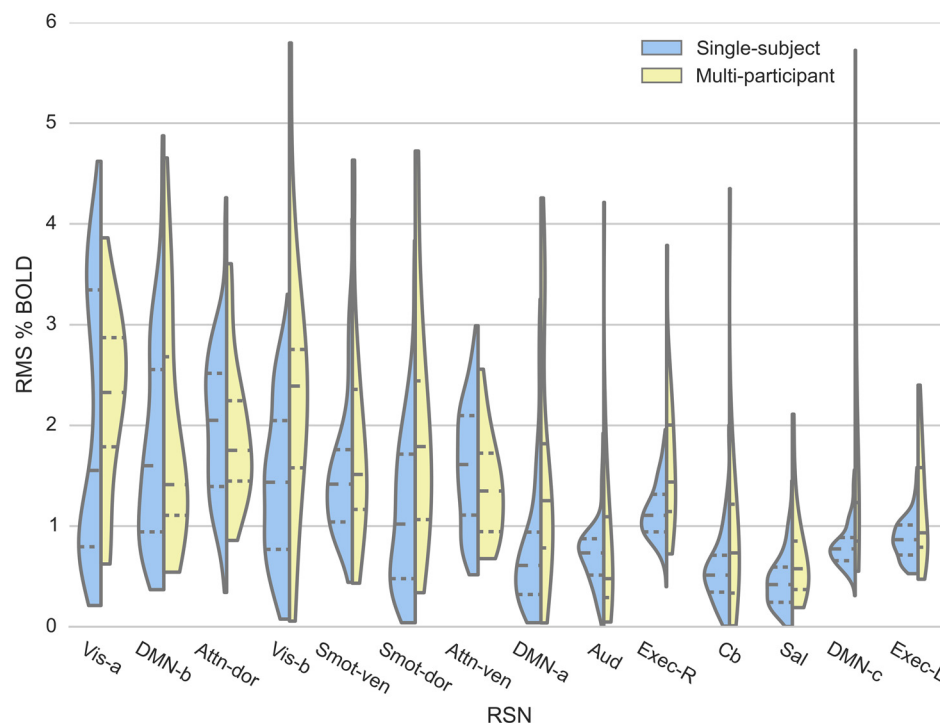
Fig 4. Reproducibility of RSN signal temporal fluctuation magnitude. Blood oxygenation level dependent (BOLD) signal fluctuation magnitude for each session's RSN time courses, calculated as root-mean-squared (RMS) % BOLD for the single-subject (blue) and multi-participant (yellow) data, is visualized using violin plots.

doi:10.1371/journal.pone.0140134.g004

participant datasets, with seven out of ten RSN pairs with the strongest connectivity in the single-subject dataset's top ten list also appearing in the multi-participant dataset's top ten list.

Values of mean and SD BNCs are also visualized as matrices in Fig 5(a) and 5(b), respectively. Within each matrix, the single-subject dataset is presented below the main diagonal, and the multi-participant dataset is presented above. For each RSN pair, differences in mean and SD BNC between single- and multi-participant datasets was small, as shown in Fig 5(c).

In order to verify that the mean BNC values for each RSN pair in the single-subject dataset are within the range of BNC values for the corresponding RSN pairs in the multi-participant dataset, the difference in mean BNC between the two datasets were used to sort and identify ten RSN pairs with the smallest (Fig 5d; top) and the largest (Fig 5d; bottom) differences. Fig 5d-bottom shows that the single-subject mean BNC values for the ten RSN pairs with the largest differences are still within the range of the corresponding multi-participant BNC values.

Additionally, CV values of the BNC measures were used to sort and identify ten RSN pairs with the highest reproducibility for both the single- and multi-participant datasets (Table 4). For the single-subject dataset (Table 4; top), the Exec-L/Exec-R network pair was shown to be the most reproducible, with a CV value of 13.6%, while the Smot-dor/Smot-ven network pair was the most reproducible for the multi-participant dataset (Table 4; bottom), with a CV value of 27.4%. For the single-subject dataset, the somatosensory and visual networks had the most reproducible correlations with other RSNs, and this observation also held for the multi-participant dataset.

Finally, recognizing that artificially inflated CV values can arise if a mean value of a data set is close to zero, and therefore to help keep things in perspective, we also report corresponding

Table 2. Reproducibility of RSN temporal signal fluctuation magnitude.

RSN	Quadratic mean (RMS) of percent signal change					
	Single-subject			Multi-participant		
	mean	SD	CV (%)[¶]	mean	SD	CV (%)
Exec-L	0.879	0.2151	24.5	1.177	0.5682	48.3
Exec-R	1.146	0.2866	25.0	1.646	0.7456	45.3
DMN-c	0.803	0.2153	26.8	1.692	1.3629	80.6
Attn-dor	2.024	0.7637	37.7	1.916	0.7261	37.9
Attn-ven	1.589	0.6157	38.7	1.378	0.5371	39.0
Smot-ven	1.509	0.6486	43.0	1.821	1.1022	60.5
Aud	0.726	0.3308	45.6	0.866	0.9645	111.4
Vis-b	1.428	0.7839	54.9	2.283	1.3495	59.1
DMN-b	1.793	1.0336	57.6	1.902	1.1687	61.4
Cb	0.568	0.3439	60.6	0.948	0.9579	101.0
Sal	0.454	0.2766	60.9	0.716	0.4888	68.2
Vis-a	2.009	1.3182	65.6	2.260	0.9217	40.8
Smot-dor	1.144	0.7834	68.4	1.981	1.2326	62.2
DMN-a	0.783	0.6713	85.8	1.574	1.2306	78.2

[¶]Sorting column/variable.

The mean, SD, and CV values for each network's temporal signal fluctuation magnitude, expressed as the quadratic mean (root mean square; RMS), is shown for the single- and multi-participant datasets.

doi:10.1371/journal.pone.0140134.t002

SD values (Tables 3 and 4, S2 Table, and Fig 5b). BNC SD values ranged from 0.082 to 0.29 (Fig 5b and S2 Table), and the RSN pairs with the smallest SD values in the single-subject dataset were Exec-L/Exec-R and Cb/Vis-a pairs, with SD values of 0.082 and 0.101, respectively. Weekly BNC measures of the two RSN pairs with the smallest SD values (Exec-L/Exec-R and Cb/Vis-a) and two RSN pairs with the largest SD values (DMN-c/Smot-ven and Smot-dor/DMN-c) in the single-subject dataset are showed in Fig 6.

Time Series Analysis

Trend. RSNs and RSN pairs with significant (after correction for multiple comparisons) linear trends in rs-fMRI outcome measures are visualized as matrices in the top row of Fig 7. These matrices are color-coded to indicate statistically identified positive, negative, and no trend. For each RSN outcome measure, the intercept and slope of the estimated linear trend, as well as the slope's corresponding F statistic and associated p-value, are listed in Table 5. Eleven out of the fourteen RSNs showed significant linear trends in η^2 over 185 weeks. Of these eleven RSNs, ten showed positive trends, while Exec-R showed a negative trend. In comparison, only two (Vis-a and DMN-b) of 14 RSNs showed significant trends in the temporal fluctuation magnitude and twenty-nine out of 105 RSN pairs showed significant trends in BNC. All trends were positive for temporal fluctuation magnitude and BNC. Significant linear trends in BNC were more pronounced in RSN pairs containing DMN-a or DMN-c networks, although significant trends were observed in various RSN pairs involving all categories of functional networks (*i.e.*, auditory, sensorimotor, visual, DMN, attention, executive, salience, and cerebellar).

The weekly FD (a measure of subject motion) and signal intensity measures from the phantom stability study (a measure of week-to-week scanner stability), did not show significant linear trends (not reported separately). Additionally, permutation tests with 1000 iterations

Table 3. Strength of between-network connectivity (BNC).

RSN pairs	Between network connectivity					
	Single-subject			Multi-participant		
	mean¶	SD	CV (%)	mean	SD	CV (%)
Aud / Smot-ven	0.660	0.126	19.1	0.567	0.187	32.9
Smot-dor / Vis-b	0.650	0.135	20.7	0.445	0.223	50.1
Vis-b / Vis-a	0.636	0.166	26.1	0.606	0.191	31.6
Exec-L / Exec-R	0.599	0.0815	13.6	0.509	0.152	29.9
Smot-ven / Vis-a	0.593	0.167	28.1	0.453	0.163	36.0
Vis-b / DMN-b	0.554	0.208	37.6	0.398	0.215	54.2
Smot-dor / Smot-ven	0.551	0.204	37.1	0.554	0.152	27.4
Aud / Vis-a	0.538	0.171	31.8	0.306	0.160	52.2
Smot-dor / Vis-a	0.538	0.212	39.4	0.488	0.182	37.3
Aud / DMN-b	0.527	0.182	34.5	0.345	0.247	71.5
RSN pairs	Between network connectivity					
	Single-subject			Multi-participant		
	mean	SD	CV (%)	mean¶	SD	CV (%)
Vis-b / Vis-a	0.636	0.166	26.1	0.606	0.191	31.6
Aud / Smot-ven	0.660	0.126	19.1	0.567	0.187	32.9
Smot-dor / Smot-ven	0.551	0.204	37.1	0.554	0.152	27.4
Exec-L / Exec-R	0.599	0.082	13.6	0.509	0.152	29.9
Smot-dor / Vis-a	0.538	0.212	39.4	0.488	0.182	37.3
Smot-ven / Vis-a	0.593	0.167	28.1	0.453	0.163	36.0
Smot-dor / Vis-b	0.650	0.135	20.7	0.445	0.223	50.1
Vis-b / Attn-dor	0.358	0.233	65.3	0.412	0.230	55.9
DMN-c / DMN-b	0.276	0.198	71.9	0.411	0.208	50.7
Aud / Attn-dor	0.505	0.164	32.5	0.402	0.179	44.5

¶Sorting column/variable.

The mean, SD, and CV values of the ten RSN pairs with the largest BNC values of the single- (top table) and multi- (bottom table) participant datasets. Each table was sorted based on the mean BNC values. A full table of mean and SD values for all RSN pairs can be found in the S2 Table.

doi:10.1371/journal.pone.0140134.t003

confirmed that significant linear trends no longer exist when weekly outcome measures are randomized.

Annual periodicity. RSNs and RSN pairs with significant (after correction for multiple comparisons) annual periodicity in relevant outcome measures are visualized as matrices in the middle row of Fig 7. The matrices are color-coded in black and red, where red blocks highlight RSNs and RSN pairs with significant annual periodicity. Table 6 lists p-values for RSNs and RSN pairs with significant periodicity, for each outcome measure. Nine out of 14 total RSNs showed significant annual periodicity in the η^2 measure over the period of 185 weeks. In comparison, only three (Vis-a, Attn-ven, and Attn-dor) of the 14 RSNs showed significant annual periodicity for temporal fluctuation magnitude measures, and none of the 105 RSN pairs showed significant annual periodicity for the BNC measures. Additionally, Table 6 shows that the majority of the RSNs with significant annual periodicity also display good correlation with Baltimore's daily maximum temperature, with correlation coefficients ranging from 0.27 to 0.34. Permutation tests with 1000 iterations confirmed that the observed significant linear trends no longer exist when weekly outcome measures are randomized.

Persistence. After ARMA models that best described the autocorrelation structure of RSN outcome measure time courses had been estimated, the order of the AR portion of the model
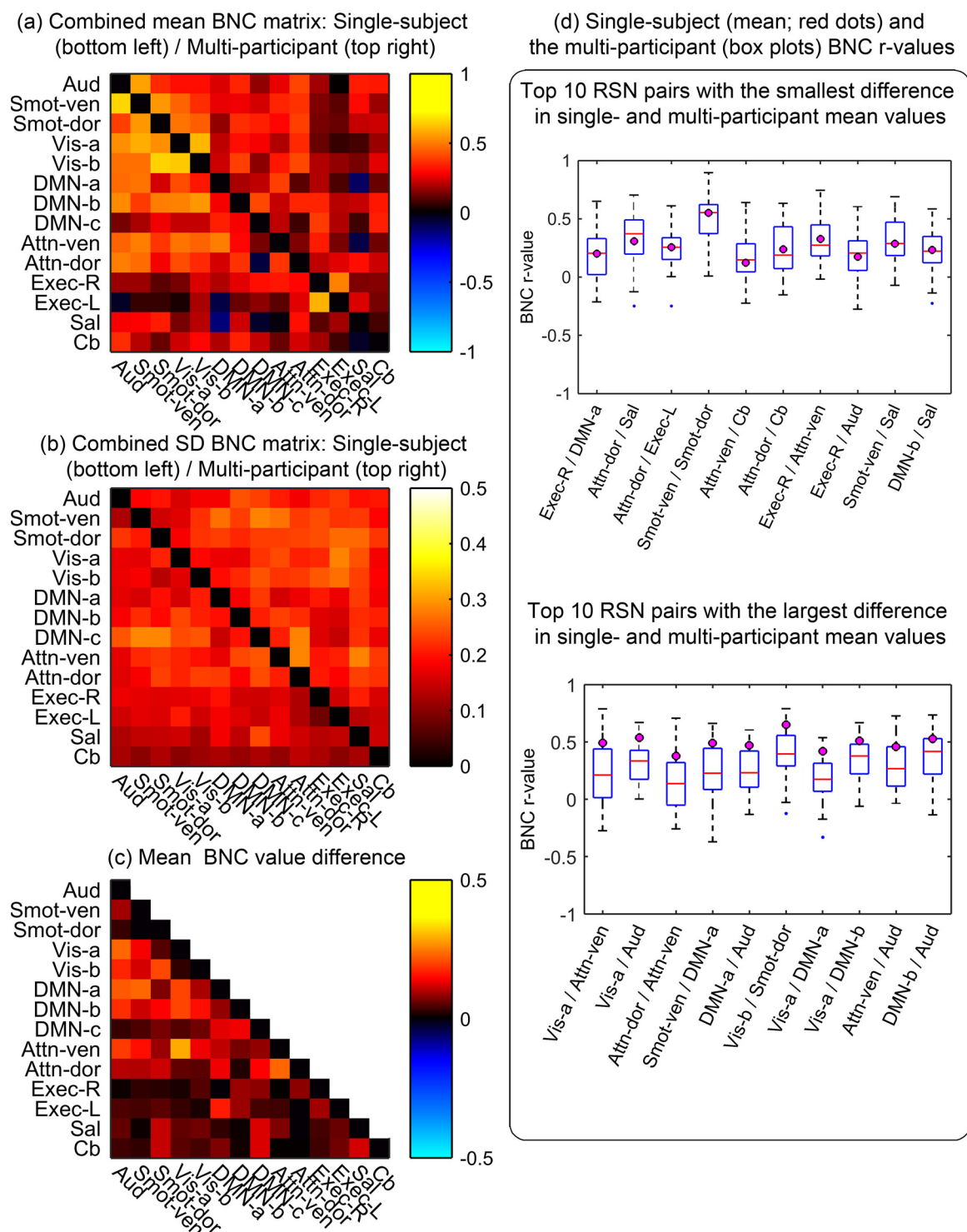
(a) Combined mean BNC matrix: Single-subject (bottom left) / Multi-participant (top right)

(b) Combined SD BNC matrix: Single-subject (bottom left) / Multi-participant (top right)

(c) Mean BNC value difference

(d) Single-subject (mean; red dots) and the multi-participant (box plots) BNC r-values

Top 10 RSN pairs with the smallest difference in single- and multi-participant mean values

Top 10 RSN pairs with the largest difference in single- and multi-participant mean values

Fig 5. Reproducibility of between-network connectivity (BNC) measurements. The combined BNC matrices show the degree of temporal synchrony between RSN pairs. Mean (a) and standard deviation (SD) (b) BNC values of the single- (below the main diagonal) and multi-participant (above the main diagonal) are shown. The diagonal elements were zeroed for display purposes. (c) Absolute value of the difference between the single- and the multi-participant BNC values. (d) Ten RSN pairs with the smallest (top) and the biggest (bottom) differences between single- and multi-participant mean BNC values. Mean BNC values from the single-subject dataset are overlaid as magenta circles on boxplots reporting on multi-participant data.

Table 4. Reproducibility of BNC.

RSN pairs	Between network connectivity					
	Single-subject			Multi-participant		
	mean	SD	CV (%)¶	mean	SD	CV (%)
Exec-L / Exec-R	0.599	0.0815	13.6	0.509	0.152	29.9
Aud / Smot-ven	0.660	0.126	19.1	0.567	0.187	32.9
Smot-dor / Vis-b	0.650	0.135	20.7	0.445	0.223	50.1
Vis-b / Vis-a	0.636	0.166	26.1	0.606	0.191	31.6
Smot-ven / Vis-a	0.593	0.167	28.1	0.453	0.163	36.0
Aud / Vis-a	0.538	0.171	31.8	0.306	0.160	52.2
DMN-a / Smot-ven	0.489	0.158	32.3	0.259	0.268	104
Cb / DMN-b	0.338	0.110	32.4	0.325	0.209	64.3
Aud / Attn-dor	0.505	0.164	32.5	0.402	0.179	44.5
Aud / Cb	0.360	0.123	34.1	0.323	0.201	62.4
RSN pairs	Between-network connectivity					
	Single-subject			Multi-participant		
	mean	SD	CV (%)	mean	SD	CV (%)¶
Smot-dor / Smot-ven	0.551	0.204	37.1	0.554	0.152	27.4
Exec-L / Exec-R	0.599	0.082	13.6	0.509	0.152	29.9
Vis-b / Vis-a	0.636	0.166	26.1	0.606	0.191	31.6
Aud / Smot-ven	0.660	0.126	19.1	0.567	0.187	32.9
Smot-ven / Vis-a	0.593	0.167	28.1	0.453	0.163	36.0
Smot-dor / Vis-a	0.538	0.212	39.4	0.488	0.182	37.3
Attn-ven / DMN-a	0.502	0.172	34.2	0.395	0.154	39.1
DMN-c / Exec-R	0.306	0.151	49.3	0.387	0.162	41.9
Aud / Attn-dor	0.505	0.164	32.5	0.402	0.179	44.5
DMN-b / Exec-R	0.256	0.153	59.8	0.345	0.165	47.9

¶Sorting column/variable.

The mean, SD, and CV values of the ten most reproducible network pairs of the single- (top table) and multi-participant (bottom table) datasets. A full table of mean and SD values of all network pairs can be found in the S2 Table.

doi:10.1371/journal.pone.0140134.t004

for each RSN and RSN pair were visualized as matrices in the bottom rows of Fig 7 (More detailed description of the ARMA models can be found in S1 Text). The matrices were color-coded, where red indicates AR order of 1, yellow indicates AR order of 2, and white indicates AR order of 3. The MA portion of the model are not visualized, but are listed in S3 Table, which lists the ARMA models that best describe the autocorrelation structure of the weekly outcome measures.

Twelve out of 14 RSNs displayed significant autocorrelation in the η^2 measure over the period of 185 weeks. In comparison, only three (Vis-a, DMN-b, and Sal) out of 14 RSNs displayed significant autocorrelation for temporal fluctuation magnitude measures, and 26 of the 105 RSN pairs displayed significant autocorrelation in BNC. The order of estimated ARMA models was shown to vary, where AR and MA orders ranged from 0 to 3 for the three types of RSN outcome measures (S3 Table).

Discussion

Previous reproducibility studies of intrinsic functional networks showed that RSNs are reproducible across participants [29,38,39], within participants over durations of weeks to months
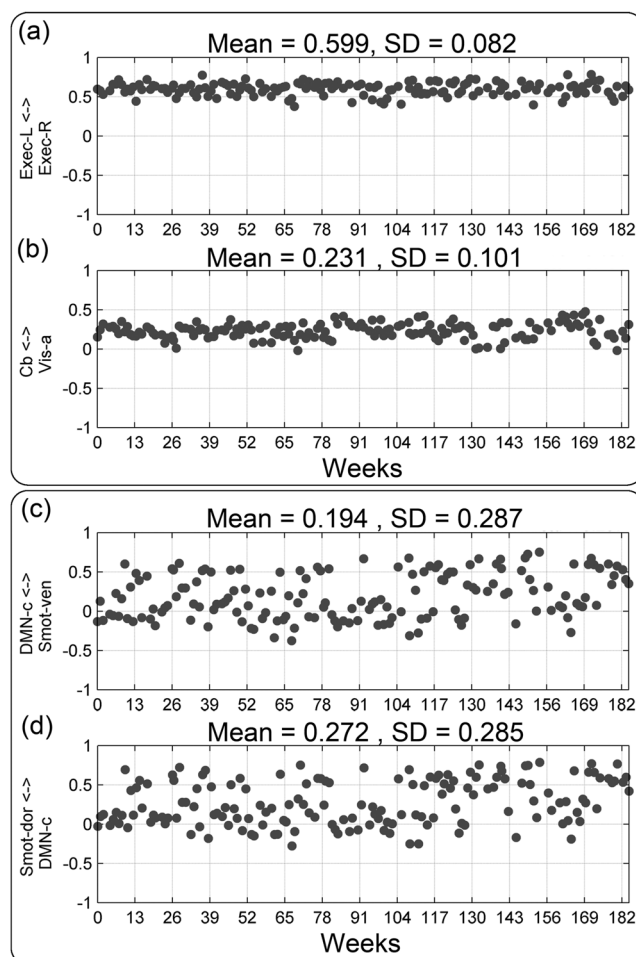
Fig 6. Weekly BNC measures of RSN pairs with the two largest and smallest variations in BNC measurements. Weekly BNC measures are plotted against the corresponding image acquisition weeks for the RSN pairs with the two largest (top) and two smallest (bottom) variations in BNC measurements, as measured by SD.

doi:10.1371/journal.pone.0140134.g006

[29,40,41], as well as up to a year [42]. The primary goal of this study was to investigate whether intra-subject inter-session RSN outcome measures were reproducible over an even longer period that is more relevant for rehabilitation studies, and this is confirmed by the results.

Functional Networks

The 14 RSNs identified in this study (Fig 1) were in good correspondence with those consistently reported in previous rs-fMRI studies. The identified RSNs included an auditory network [41], ventral and dorsal sensorimotor networks [1,24,41], two visual networks [24,41], three default mode networks [24,41,43], ventral and dorsal attention networks [41], left and right executive-function networks [44], a salience network [45], and a cerebellar network [29,46]. Of the 35 initially estimated ICs, 21 were rejected as nuisance components (of non-neuronal sources); this rate of rejection of nuisance components was consistent with previous studies [29].
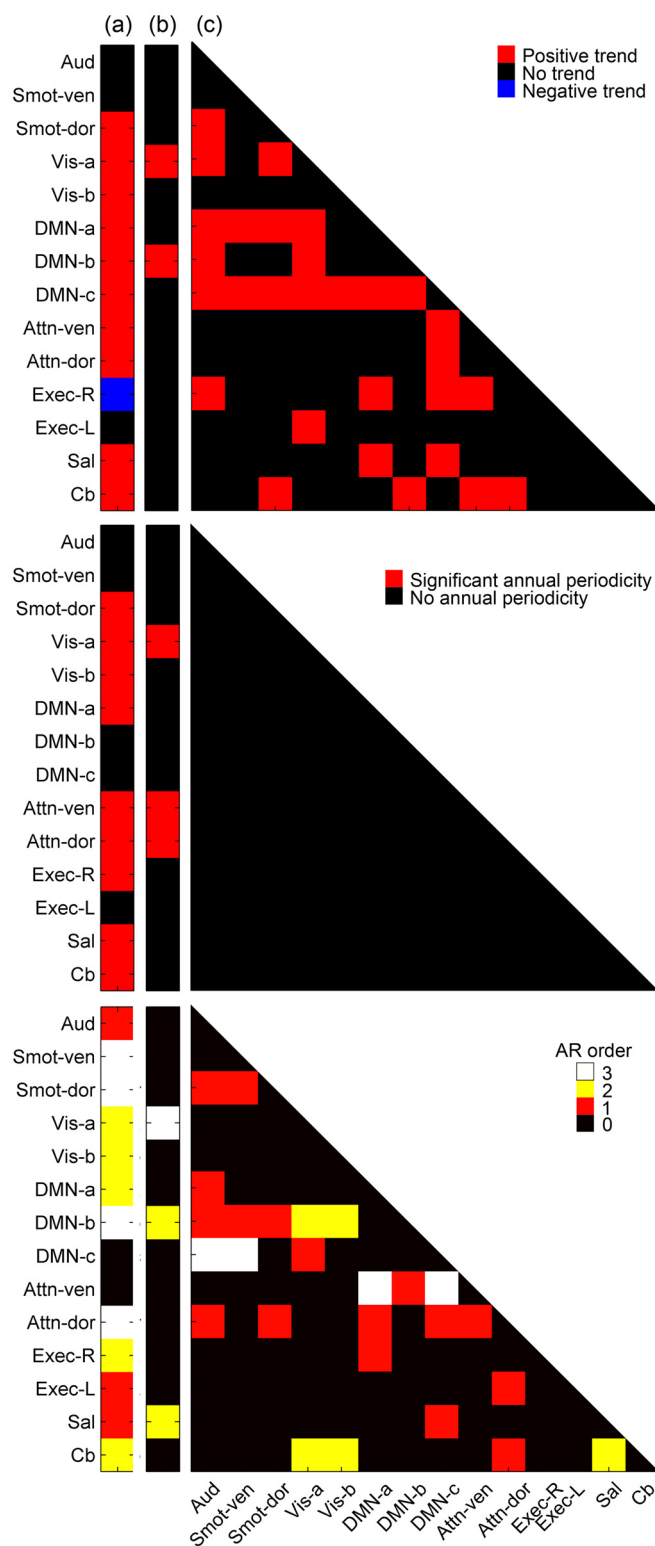
Fig 7. RSNs with significant temporal structures. TOP Existence of significant (after correction for multiple comparisons) linear trends in three RSN outcome measures, namely the (a) spatial similarity (eta-squared, η^2), (b) temporal signal fluctuation magnitude, and (c) BNC, are visualized using matrices. Red blocks indicate significant positive linear trend, blue blocks negative trend, and black boxes no significant trend. MIDDLE Existence of significant (after correction for multiple comparisons) annual periodicity in three RSN

outcome measures. Red blocks indicate significant annual periodicity and black boxes no annual periodicity. BOTTOM AR orders of the estimated ARMA models for RSNs and RSN pairs are visualized for each outcome measures, where black box indicates no autocorrelation, red box AR order of 1, yellow box AR order of 2, and white box AR order of 3. Refer to S3 Table for information on full ARMA model parameters.

doi:10.1371/journal.pone.0140134.g007

Reproducibility

Spatial similarity of RSN maps. As group mean maps (Fig 2; left column) are obtained by averaging multiple RSN spatial maps across sessions, the most robust "core" activation regions in the RSN spatial maps are preserved within the group mean maps. Measuring the spatial similarity of each backreconstructed RSN map to its corresponding group mean map, therefore, may provide insight into the degree of robustness of core activation region, reflected by the value of η^2, and the degree of robustness of "non-core" activations, reflected by the variance of η^2. The high mean η^2 values of all RSNs, ranging from 0.747 to 0.84, show that the 14 RSNs identified in the study have very robust core activation regions. Stronger core activation regions, however, did not translate to higher reproducibility. The Vis-a network, for example, showed that a network can have a strong core activation region and also have variable non-core activation regions that lead to increased variability in the spatial similarity measure (Table 1 and Fig 3). This network's variable non-core activation regions can also be visually observed in Fig 2.

For both single- and multi-participant datasets, the three networks with the lowest spatial map inter-session reproducibility were exteroceptive in nature (*i.e.*, related to the external world), namely visual and sensorimotor networks (Vis-a, Vis-b, Smot-dor, and Cb). Consistent with Kosslyn's reports on ideation [47], "mind wandering" during rest may have led to increased modulation in the exteroceptive networks.

Finally, for nine out of 14 RSNs, the intra-subject inter-session reproducibility, as measured using CV, of the RSN spatial maps was higher than, or similar to, inter-participant reproducibility, with Smot-ven network displaying significant difference after Bonferroni correction for multiple comparisons. While this observation may be explained by the inherent higher inter-participant variability in the dataset, such a difference could also arise due to imperfect spatial normalization across participants. This suggests that caution may be warranted in using atlas-based seed placement for seed-based correlation, and that more sophisticated spatial normalization methods (*e.g.*, large deformation diffeomorphic metric mapping (LDDMM) [48,49]) may be beneficial.

Temporal fluctuation magnitudes of RSN time courses. For all RSNs, mean intra-subject inter-session RMS % BOLD values (Fig 4, Table 2) were comparable to those reported in a previous multi-participant rs-fMRI study [41]. Additionally, RSNs that showed low spatial map intra-subject inter-session reproducibility also tended to show low temporal fluctuation magnitude intra-subject inter-session reproducibility. Many such least-reproducible RSNs were of exteroceptive nature, and thus may support the previously stated hypothesis that "mind wandering" [47] during rest may have led to increased modulation in exteroceptive networks.

It should also be noted that compared to the CV values of the network spatial maps (Table 1), the CV values of the temporal fluctuation magnitude (Table 2) were significantly larger, ranging from 24.5 to 85.8% for the single-subject dataset and from 37.9 to 111.4% for the multi-participant dataset. These significantly larger CV values were driven by the small mean values and large SD values of the temporal signal fluctuation measurement. Using CV as a measure of dispersion is suboptimal when a mean value is close to zero, as calculated CV measure becomes sensitive to small changes. In this case, a larger issue may be the relatively

Table 5. RSNs with significant linear trends in RSN outcome measures.

(a) Eta-squared (η^2)

RSN	Intercept	Slope (week^{-1})	F statistic (slope)	p-value
Smot-dor	0.77	1.94E-04	12.78	4.67E-04
Vis-a	0.81	3.77E-04	22.89	3.94E-06
Vis-b	0.78	2.50E-04	20.57	1.14E-05
DMN-a	0.76	1.31E-04	46.92	1.61E-10
DMN-b	0.8	1.15E-04	19.28	2.07E-05
DMN-c	0.8	5.65E-05	7.87	5.67E-03
Attn-ven	0.8	7.40E-05	9.47	2.47E-03
Attn-dor	0.78	1.50E-04	12.91	4.38E-04
Exec-R	0.79	-6.15E-05	11.42	9.16E-04
Sal	0.78	7.76E-05	12.59	5.13E-04
Cb	0.8	1.21E-04	14.96	1.61E-04

(b) Temporal fluctuation magnitude

RSN	Intercept	Slope (week^{-1})	F statistic (slope)	p-value
Vis-a	1.42	6.51E-03	11.64	8.24E-04
DMN-b	1.4	4.36E-03	8.33	4.46E-03

(c) Between-network connectivity

RSN pairs	Intercept	Slope (week^{-1})	F statistic (slope)	p-value
Aud/Smot-dor	0.3	1.01E-03	9.4	2.56E-03
Aud/Vis-a	0.46	8.26E-04	11.11	1.07E-03
Aud/DMN-a	0.41	6.44E-04	6.78	1.01E-02
Aud/DMN-b	0.47	6.82E-04	6.48	1.19E-02
Aud/DMN-c	0.02	1.30E-03	13.14	3.90E-04
Aud/Exec-R	0.12	6.50E-04	6.46	1.20E-02
Smot-ven/DMN-a	0.43	6.06E-04	6.79	1.01E-02
Smot-ven/DMN-c	0.06	1.45E-03	12.19	6.24E-04
Smot-dor/Vis-a	0.47	7.68E-04	6.05	1.50E-02
Smot-dor/DMN-a	0.17	7.76E-04	7.27	7.77E-03
Smot-dor/DMN-c	0.13	1.58E-03	14.99	1.59E-04
Smot-dor/Cb	0.07	6.09E-04	10.65	1.36E-03
Vis-a/ DMN-a	0.36	5.88E-04	6.4	1.24E-02
Vis-a/ DMN-b	0.43	8.59E-04	6.01	1.53E-02
Vis-a/ DMN-c	0.13	1.05E-03	8.93	3.27E-03
Vis-a/Exec-L	0.12	-9.81E-04	10.87	1.21E-03
Vis-b/DMN-c	0.09	1.43E-03	16.16	9.02E-05
DMN-a/ DMN-c	0.28	6.38E-04	9.03	3.09E-03
DMN-a/Exec-R	0.13	7.83E-04	7.18	8.16E-03
DMN-a/ Sal	-0.21	8.33E-04	10.34	1.59E-03
DMN-b/ DMN-c	0.19	9.64E-04	11.27	9.90E-04
DMN-b/ Cb	0.29	5.40E-04	11.55	8.60E-04
DMN-c/Attn-ven	-0.02	1.69E-03	23.52	2.96E-06
DMN-c/Attn-dor	-0.17	1.18E-03	11.51	8.78E-04
DMN-c/Exec-R	0.25	6.04E-04	7.44	7.10E-03
DMN-c /Sal	-0.14	1.01E-03	8.3	4.51E-03
Attn-ven/ Cb	0.09	3.82E-04	5.93	1.60E-02
Attn-ven/Exec-R	0.27	5.84E-04	5.89	1.64E-02

(*Continued*)

Page | 70

Table 5. (*Continued*)

Attn-dor/ Cb	0.16	8.40E-04	18.04	3.71E-05

Intercept and slope of the estimated linear trend, as well as the slope's F statistic and p-value in three RSN outcome measures, namely the (a) spatial similarity (eta-squared, η^2), (b) temporal fluctuation magnitude, and (c) BNC, for each RSNs with significant linear trends are listed.

doi:10.1371/journal.pone.0140134.t005

large SD values of the RSN temporal fluctuation magnitude; the fact that the SD values of many RSNs are close to the corresponding mean values indicates that the measure may be relatively insensitive to small effect sizes, and caution is thus warranted when using the this outcome measure in longitudinal studies.

Between-network connectivity of RSN time courses. The ranges of mean BNC values for the single-subject dataset (-0.133–0.660), and the multi-participant dataset (-0.104–0.606) (Table 3, S2 Table) were similar, and strong BNC values were observed between networks within the same functional domains; such as between the Vis-a/Vis-b (0.636), Exec-L/Exec-R (0.599), and Smot-dor/Smot-ven (0.551) RSN pairs. The same held for the multi-participant dataset, with BNC values of 0.606 for Vis-a/Vis-b, 0.554 for Smot-dor/Smot-ven, and 0.509 for Exec-L/Exec-R network pairs. Overall, the mean BNC values for the single- and multi-participant datasets were similar, reflected by the highly symmetric combined correlation matrix of the datasets (Fig 5a). In addition, network pairs that showed strong connectivity within the single-subject dataset also showed strong connectivity within the multi-participant dataset.

Similar to the large CV values that were observed for temporal fluctuation magnitude measurements, the CV values for the BNC measurements were also relatively high, driven by the

Table 6. RSNs with significant annual periodicity and/or significant correlation with daily maximum temperature (Baltimore MD, USA) in outcome measures.

(a) Eta-squared (η^2)			
RSN	p-value (annual periodicity)	Correlation coefficient (w/ daily maximum temperature)	p-value (w/ daily maximum temperature)
Aud	&	0.27	5.44E-04
Smot-dor	1.32E-03	0.31	6.41E-05
Vis-a	2.28E-03	0.29	2.14E-04
Vis-b	4.71E-04	0.29	2.80E-04
DMN-a	3.38E-05	0.29	2.78E-04
Attn-ven	7.44E-03	0.34	1.13E-05
Attn-dor	2.61E-03	0.31	9.74E-05
Exec-R	2.81E-03	&	&
Sal	3.79E-03	0.31	6.85E-05
Cb	5.29E-04	0.34	1.44E-05
(b) Temporal fluctuation magnitude			
RSN	p-value (annual periodicity)	Correlation coefficient (w/ daily maximum temperature)	p-value (w/ daily maximum temperature)
Vis-a	7.90E-03	0.30	1.43E-04
DMN-b	&	0.25	1.44E-03
Attn-ven	7.84E-04	0.30	1.31E-04
Attn-dor	5.72E-03	0.23	3.34E-03

& Statistically not significant.

P-values of RSNs with significant annual periodicity and/or correlation coefficient and associated p-values of RSNs with significant correlation with daily maximum temperature of Baltimore, MD, are listed for two RSN outcome measures; namely the (a) spatial similarity (η^2) and (b) temporal fluctuation magnitude. No RSN pairs showed significant annual periodicity for BNC measures.

doi:10.1371/journal.pone.0140134.t006

small mean BNC values. Nonetheless, the intra-subjection inter-session reproducibility of BNC values was good, reflected by the small SD values, as shown in Fig 5b and S2 Table. It should be noted, however, that in cases where a mean BNC value is close to zero, the corresponding SD value needs to be very small before the BNC value of a particular functional network pair can be used as a reproducible longitudinal measure. Therefore, caution should be taken when investigating network pairs with high variance, relative to the corresponding mean BNC value.

For both the single- and multi-participant datasets, RSN pairs with connections to the somatosensory and visual networks demonstrated higher reproducibility (Table 4). This observation agrees with results from a previous study that reported robust inter-participant reliability for the primary visual network [50], compared with other networks.

One of the main observations of this study was the very high intra-subject inter-session reproducibility of the Exec-L and Exec-R networks. For the single-subject dataset, these networks were the most reproducible RSNs for spatial map (Table 1) and temporal signal fluctuation magnitude (Table 2) outcome measures. Additionally, connectivity between the Exec-L/Exec-R RSN pair was the most reproducible, with the smallest CV value of 13.6% (Fig 4, Table 4). This RSN pair was also among the most reproducible networks for all rs-fMRI outcome measures in the multi-participant dataset. Such high intra-subject inter-session reproducibility of the executive control network components has an important implication, as the executive control network is known to be actively involved in functions such as impulse control [51] and consciousness [52,53], and is closely related to disease states such as substance abuse [51], unresponsive wakefulness syndrome [52], and Alzheimer's disease [54]. Accordingly, this suggests that the executive RSN components and the related outcome measures have high potential for serving as biomarkers of disease states.

Time Series Analysis

Trend. η^2 values of weekly RSN spatial maps correspond to degrees of spatial similarity between weekly maps and a group mean map. Therefore, the existence of a trend in the η^2 measurements (Fig 7 TOP(a), Table 5a) is noteworthy. Specifically, a positive trend in η^2 indicates that as time passes, weekly single-session maps become more stable, looking more like the group mean map. A negative trend, on the other hand, would indicate that weekly maps become more variable, looking less like the group mean map as time passes. Previous studies show that a constant and linear decrease of gray matter volume can be initiated as early as the 20's [55–57]. While the exact cause of this decline is still under debate, one theory suggests that the decline is due to neuronal and synaptic pruning in the human cortex during reorganization following neural maturation [58]. Our observation of positive trends in the η^2 values for most of the RSNs may partially be explained by such neuronal pruning of gray matter. Preliminary analysis of the subject's high resolution T1w structural images revealed that the subject's gray matter volume decreased by about 0.30 ml/month over the study period [59]; this linear decrease in gray matter volume is consistent with previous reports [55].

Possible long-term habituation of the subject to the scanning environment, and a subsequent decrease of subject motion, was also identified as possible causes for the almost ubiquitous positive trends in η^2 measures. Analysis of the degree of subject motion, represented by weekly FD measures, however, showed that there was no significant trend in the degree of movement across imaging sessions. Similarly, there was no significant trend in the weekly signal intensity measures from the phantom stability data, indicating that any contribution of variable scanning environment over the 185 weeks to the observed linear trends in the η^2 values was minimal.

The effect of age on RSNs has been extensively explored in previous literature [20,60–68]. Specifically, the level of coherent activity and degree of co-activation within RSNs are shown to increase during early childhood and young adulthood, indicating neuronal maturation of the networks. This phase is followed by decreases in the level of coherent activity and degree of co-activation in the older population, marked by subsequent cognitive decline [20,60–68]. Such decreases in coherent activity, measured using the magnitude of temporal fluctuation, and degree of co-activation, measured using BNC, were not observed in the subject. Instead, all significant trends reported in this study were positive (Fig 7 TOP(b-c) and Table 5b and 5c). One reason for the discrepancy may be that majority of the above-mentioned studies compared cohorts of young participants (10–34 yrs) and much older participants (60–93 yrs), thus not including the age range of the subject studied here (ca. 40 yrs). Two studies that did include participants in their 40's [20,68] reported mixed results for different RSNs. It should also be noted that the effects of age on functional connectivity could be mediated by various factors such as stress, education, and exercise [69,70].

A limitation of this study is that the existence of a trend was inferred only using general linear model. This method reports the best fitting linear model of the type specified, but more sophisticated trend detection algorithms may reveal more complex types of trends. Also, it should be noted that effect sizes in the temporal analyses are very small, which may indicate that observed significance is driven by the large number of degrees of freedom. And while this data set is large for fMRI, it is not an exceptionally long time series relative to the norm of seasonal studies.

Annual periodicity. The unique longitudinal dataset of the study enabled us to investigate whether seasonal (more specifically, annual) patterns exists in RSN outcome measures, and the results show that such seasonal patterns exist in the weekly η^2 and temporal fluctuation magnitude measures of relevant RSNs (Fig 7 MIDDLE and Table 6). This result is also confirmed by the good correlation between the RSN outcome measure time courses and Baltimore's daily maximum temperature observed in Table 6. However, the cause and mechanism of the observed seasonal patterns is unknown at this time. There are, however, several studies that look into the fluctuating patterns of shorter timeframe (*e.g.*, diurnal and monthly) in functional connectivity measures, and we looked to see whether such higher frequency fluctuation in relevant RSNs translate to lower frequency annual fluctuation.

Interaction between circadian rhythmicity and time awake (homeostatic process), and the resulting diurnal rhythms within various biological systems that range from gene expression [71,72] to body temperature [73] is well-known. Diurnal rhythms were also shown to affect higher order cognitive functions [74–76], and recent studies have shown that diurnal rhythms also exist in the strength of functional connectivity [77–79]. One study in particular showed that highly rhythmic connectivity patterns exist within sub-systems of DMN and sensorimotor network [77]. However, the observed diurnal rhythm in DMN and sensorimotor networks did not translate to the existence of annual periodicity in the same RSNs (*i.e.*, DMN and sensorimotor networks did not show annual periodicity; Fig 7 TOP(b)). None of the BNC measures display significant annual periodicity (Fig 7 MIDDLE(c) and Table 6c), and this result is consistent in part with a previous study [80], which reported a lack of monthly fluctuation of BNC values. It is not clear at this time why some RSN outcome measures, but not others, show annual periodicity.

Persistence. The persistence, or autocorrelation, of a system describes the system's tendency to stay in the same state from one observation to the next, and is a common feature of many biological systems. While the existence of persistence within a system can complicate the understanding of its underlying mechanism by reducing the number of independent variables and introducing multiple confounding parameters that are not easily separable, persistence can

also be exploited to predict future observations based on those of the past [81,82]. Realization of the existence of persistence in a system, and the subsequent estimation of a best-fit mathematical model of the persistence, therefore can lead to: 1) better understanding of the system by quantitatively assessing the fraction of the system's variance explained by the measured persistence, and 2) better prediction of the behavior of a time course based on past observations. Our results show that persistence is a characteristic of many RSNs and RSN pairs, for all three types of RSN outcome measures (Fig 7 BOTTOM and S3 Table). Within the context of using rs-fMRI derived outcome measures as patient-specific biomarkers of recovery during clinical trials, this observation may lead to the development of more accurate inferences from such data.

Limitations

A major limitation of this report is that only one subject underwent the weekly scanning for 185 weeks. Scanning additional participants would have helped to ensure the generality of our findings. However, ensuring compliance of multiple participants over such a prolonged period would have been difficult. We have sought to address this issue by including results from a previously acquired multi-participant dataset on the same scanner and with identical acquisition parameters [12], and ensured that the healthy male individual of the longitudinal dataset was a representative healthy control. Estimated means of all network outcome measures for the longitudinal dataset—spatial maps, temporal fluctuation magnitude, and BNC—were within the range of the corresponding outcome measures from the multi-participant dataset, as shown in Figs 3–5 –*i.e.*, in all cases, values for the longitudinal dataset were within the range of those computed for the multi-participant dataset.

While we report some outcome measures for the multi-participant dataset, we refrain from an in-depth analysis of it, as the focus of this paper was on long-term reproducibility of the single-subject data. However, published reproducibility studies have consistently shown that rs-fMRI derived outcome measures were robust across participants [29,38,39,83], and here we briefly summarize previous literature on this subject. An early study by Chen *et al.*, acquired data from 14 healthy participants over the period of 16 days and reported that the intrinsic networks were consistent across multiple sessions [29]. Meindl *et al.*, assessed the reproducibility of DMN networks across multiple sessions in 18 healthy participants each scanned three times over the period of a week, and found DMN networks to be highly spatially consistent across sessions [38]. Shehzad *et al.* reported modest to high inter-participant reproducibility in a dataset acquired from 26 participants at three different times over five months [83].

Another limitation of this study is that we report only on outcome measures derived using group ICA (GICA) [18]. However, as one of the most commonly used methods to estimate RSNs, GICA offers many advantages. GICA is an extension of the ICA method, in which reducing and concatenating multi-session/multi-participant fMRI data allows ICA to be applied once to the aggregate data. This obviates the cumbersome and potentially inaccurate matching of components estimated separately from data from individual sessions and/or participants. Furthermore, the alternative method of performing ICA separately for each session may result in different numbers of components for different sessions, depending on the level of noise. A possible consequence of such approach is that networks may split into varying numbers of sub-networks, as seen in higher-order ICA analysis [20]. This in turn introduces additional uncertainty into the network identification process, and may make group inference across sessions unfeasible. Alternatively, use of GICA [18] allows delineation of identical networks for the single- and multi-participant datasets, eliminating the need to perform ICA separately on each dataset. There have been concerns that the identification of aggregate networks

using a single dataset of multiple groups, and then backreconstructing the single-session datasets, may bias the results towards the group mean. However, the original report by Calhoun *et al.*, [18], and a study by Schmidhorst and Holland [84] show that GICA can identify a network present in as little as 10% of the study population. Also, the findings reported in this study are consistent with reports of the reproducibility of rs-fMRI outcome measures estimated using alternative analytic approaches such as seed based temporal correlation [85–89].

Finally, due to time constraints, additional physiological or psychological measures were not obtained during the acquisition of this dataset. Together, such additional measures would have provided valuable information regarding the nature of the temporal structure we have observed in this study. Indeed, there are now ongoing endeavors to acquire longitudinal rs-fMRI data like ours, augmented with the regular parallel acquisition of many auxiliary measures, ranging from sleep data to blood samples. One such example is the MyConnectome project (http://myconnectome.org/wp/), during which along with rs-fMRI, biological samples (*i.e.*, blood) as well as data about daily life activities were collected. We expect our study, along with other unique longitudinal studies, will provide new insight into understanding the dynamics of brain function over time.

Conclusions

Rs-fMRI allows noninvasive observation of brain networks, and has potential to yield biomarkers for clinical trials in neurological diseases where such RSNs may change. The goal of this study was to present a unique longitudinal dataset reporting on a healthy adult subject scanned weekly over 3.5 years, and identify RSN outcome measures with high intra-subject inter-session reproducibility over prolonged timeframes appropriate for rehabilitation trials. ICA was used to identify fourteen RSNs that represent unique functional networks. Three types of rs-fMRI outcome measures, namely spatial map similarity, temporal fluctuation magnitude, and BNC, were found to be reproducible across the extended study period. In particular, the Exec-R and Exec-L networks, which are closely related to disease states such as substance abuse and Alzheimer's disease, showed high intra-subject inter-session reproducibility for all three types of RSN outcome measures, suggesting that these networks may be of particular interest.

Additionally, we sought to identify potential parameters-of-interest for clinical studies, by assessing the existence of temporal structure in the three types of rs-fMRI outcomes measures. Time series analysis showed that the RSN outcome measures displayed properties including linear trend, annual periodicity, and persistence. This finding suggests that when RSN outcome measures are considered as imaging biomarkers for lengthy therapeutic interventions in chronic conditions it may be beneficial to take the temporal structure parameters into consideration.

Supporting Information

S1 Fig. Preprocessing and group independent component analysis (GICA) flowchart.
(DOCX)

S2 Fig. Reproducibility of resting state network (RSN) spatial maps, visualized using boxplots. Spatial similarity of each session's RSN spatial map to the corresponding group mean map, measured using eta-squared (η^2), for single-subject (a) and multi-participant (b) datasets, is visualized using box plots (end of boxes: quartiles, bar within boxes: median, small dots: outliers). In (b), for each RSN, the mean η^2 of the single-subject dataset is overlaid as a large gray circle.
(DOCX)

Page | 75

S3 Fig. Reproducibility of RSN signal temporal fluctuation magnitude, visualized using boxplots. Blood oxygenation level dependent (BOLD) signal fluctuation magnitude for each session's RSN time courses, calculated as root-mean-squared (RMS) % BOLD for single-subject (a) and multi-participant (b) datasets, is visualized using boxplots. In (b), for each RSN, the mean RMS % BOLD value for the single-subject dataset is overlaid as a large gray circle. (DOCX)

S1 Table. Acquisition dates of the 158 resting state functional MRI (rs-fMRI) scans. A total of 158 scans were acquired over the period of 185 weeks. (DOCX)

S2 Table. Reproducibility of single- and multi-participant between-network connectivity (BNC) measurements. The mean and standard deviation (SD) values for all resting state network (RSN) pairs are shown for the single- and multi-participant datasets. (Aud: auditory, Smot: seonsorimotor, Vis: visual, DMN: default mode network, Attn: attention, Exec: executive, Sal: salience, Cb: cerebellar, ven: ventral, dor: dorsal, R: right, L: left). (DOCX)

S3 Table. Estimated autoregressive moving average (ARMA) models of each RSNs, for three rs-fMRI outcome measures–η^2, temporal signal fluctuation, and BNC. Properties of the estimated ARMA models for three outcome measures of each RSN are listed. The observed outcome measures are (a) spatial similarity (η^2), (b) temporal fluctuation magnitude, and (c) BNC. The coefficients of the estimated ARMA model conform to the following equation:

$$Y_t + a_1 y_{t-1} + a_2 y_{t-2} + a_3 y_{t-3} = e_t + c_1 e_{t-1} + c_2 e_{t-2} + c_3 e_{t-3},$$

where autoregressive (AR) coefficients are listed on top rows and moving-average (MA) coefficients are listed on bottom. (DOCX)

S1 Text. Detailed explanation of the autoregressive moving average (ARMA) models. (DOCX)

Acknowledgments

Author Contributions

Conceived and designed the experiments: AC SJ JP. Performed the experiments: AC CJ SJ. Analyzed the data: AC SJ. Contributed reagents/materials/analysis tools: AC JM BC ML. Wrote the paper: AC SJ VB BC ML PvZ JP.

References

1. Biswal B, Yetkin FZ, Haughton VM, Hyde JS. Functional connectivity in the motor cortex of resting human brain using echo-planar MRI. Magn Reson Med. 1995; 34: 537–541. PMID: 8524021

2. Belegu V, Oudega M, Gary DS, McDonald JW. Restoring function after spinal cord injury: Promoting spontaneous regeneration with stem cells and activity-based therapies. Neurosurg Clin N Am. 2007; 18: 143–68, xi. PMID: 17244561

3. Lorenz DJ, Datta S, Harkema SJ. Longitudinal patterns of functional recovery in patients with incomplete spinal cord injury receiving activity-based rehabilitation. Arch Phys Med Rehabil. 2012; 93: 1541–1552. doi: 10.1016/j.apmr.2012.01.027 PMID: 22920451

4. Damiano DL. Activity, activity, activity: Rethinking our physical therapy approach to cerebral palsy. Phys Ther. 2006; 86: 1534–1540. PMID: 17094192

5. Martin JH, Chakrabarty S, Friel KM. Harnessing activity-dependent plasticity to repair the damaged corticospinal tract in an animal model of cerebral palsy. Dev Med Child Neurol. 2011; 53 Suppl 4: 9–13. doi: 10.1111/j.1469-8749.2011.04055.x PMID: 21950387

6. Choe AS, Belegu V, Yoshida S, Joel S, Sadowsky CL, Smith SA, et al. Extensive neurological recovery from a complete spinal cord injury: A case report and hypothesis on the role of cortical plasticity. Front Hum Neurosci. 2013; 7: 290. doi: 10.3389/fnhum.2013.00290 PMID: 23805087

7. Helmich RC, Derikx LC, Bakker M, Scheeringa R, Bloem BR, Toni I. Spatial remapping of cortico-striatal connectivity in parkinson's disease. Cereb Cortex. 2010; 20: 1175–1186. doi: 10.1093/cercor/bhp178 PMID: 19710357

8. Hacker CD, Perlmutter JS, Criswell SR, Ances BM, Snyder AZ. Resting state functional connectivity of the striatum in parkinson's disease. Brain. 2012; 135: 3699–3711. doi: 10.1093/brain/aws281 PMID: 23195207

9. Richiardi J, Gschwind M, Simioni S, Annoni JM, Greco B, Hagmann P, et al. Classifying minimally disabled multiple sclerosis patients from resting state functional connectivity. Neuroimage. 2012; 62: 2021–2033. doi: 10.1016/j.neuroimage.2012.05.078 PMID: 22677149

10. Filippi M, Agosta F, Spinelli EG, Rocca MA. Imaging resting state brain function in multiple sclerosis. J Neurol. 2013; 260: 1709–1713. doi: 10.1007/s00415-012-6695-z PMID: 23052604

11. Inman CS, James GA, Hamann S, Rajendra JK, Pagnoni G, Butler AJ. Altered resting-state effective connectivity of fronto-parietal motor control systems on the primary motor network following stroke. Neuroimage. 2012; 59: 227–237. doi: 10.1016/j.neuroimage.2011.07.083 PMID: 21839174

12. Landman BA, Huang AJ, Gifford A, Vikram DS, Lim IA, Farrell JA, et al. Multi-parametric neuroimaging reproducibility: A 3-T resource study. Neuroimage. 2011; 54: 2854–2866. doi: 10.1016/j.neuroimage.2010.11.047 PMID: 21094686

13. Stehling MK, Turner R, Mansfield P. Echo-planar imaging: Magnetic resonance imaging in a fraction of a second. Science. 1991; 254: 43–50. PMID: 1925560

14. Pruessmann KP, Weiger M, Scheidegger MB, Boesiger P. SENSE: Sensitivity encoding for fast MRI. Magn Reson Med. 1999; 42: 952–962. PMID: 10542355

15. Friston KJ, Holmes AP, Worsley KJ, Poline JP, Frith CD, Frackowiak RSJ. Statistical parametric maps in functional imaging: A general linear approach. Human brain mapping. 1994; 2: 189–210.

16. Ashburner J, Friston KJ. Unified segmentation. Neuroimage. 2005; 26: 839–851. PMID: 15955494

17. Egolf E, Kiehl KA, Calhoun VD. Group ICA of fMRI toolbox (GIFT). 2004.

18. Calhoun VD, Adali T, Pearlson GD, Pekar JJ. A method for making group inferences from functional MRI data using independent component analysis. Hum Brain Mapp. 2001; 14: 140–151. PMID: 11559959

19. Li YO, Adali T, Calhoun VD. Estimating the number of independent components for functional magnetic resonance imaging data. Hum Brain Mapp. 2007; 28: 1251–1266. PMID: 17274023

20. Allen EA, Erhardt EB, Damaraju E, Gruner W, Segall JM, Silva RF, et al. A baseline for the multivariate comparison of resting-state networks. Front Syst Neurosci. 2011; 5: 2. doi: 10.3389/fnsys.2011.00002 PMID: 21442040

21. Allen EA, Erhardt EB, Wei Y, Eichele T, Calhoun VD. Capturing inter-subject variability with group independent component analysis of fMRI data: A simulation study. Neuroimage. 2011; 59: 4141–4159. doi: 10.1016/j.neuroimage.2011.10.010 PMID: 22019879

22. Bell AJ, Sejnowski TJ. An information-maximization approach to blind separation and blind deconvolution. Neural Comput. 1995; 7: 1129–1159. PMID: 7584893

23. McKeown MJ, Jung TP, Makeig S, Brown G, Kindermann SS, Lee TW, et al. Spatially independent activity patterns in functional MRI data during the stroop color-naming task. Proc Natl Acad Sci U S A. 1998; 95: 803–810. PMID: 9448244

24. Beckmann CF, DeLuca M, Devlin JT, Smith SM. Investigations into resting-state connectivity using independent component analysis. Philos Trans R Soc Lond B Biol Sci. 2005; 360: 1001–1013. PMID: 16087444

25. Himberg J, Hyvarinen A, Esposito F. Validating the independent components of neuroimaging time series via clustering and visualization. Neuroimage. 2004; 22: 1214–1222. PMID: 15219593

26. Cohen AL, Fair DA, Dosenbach NU, Miezin FM, Dierker D, Van Essen DC, et al. Defining functional areas in individual human brains using resting functional connectivity MRI. Neuroimage. 2008; 41: 45–57. doi: 10.1016/j.neuroimage.2008.01.066 PMID: 18367410

27. Kelly C, Uddin LQ, Shehzad Z, Margulies DS, Castellanos FX, Milham MP, et al. Broca's region: Linking human brain functional connectivity data and non-human primate tracing anatomy studies. Eur J Neurosci. 2010; 32: 383–398. doi: 10.1111/j.1460-9568.2010.07279.x PMID: 20662902

28. Kim JH, Lee JM, Jo HJ, Kim SH, Lee JH, Kim ST, et al. Defining functional SMA and pre-SMA subregions in human MFC using resting state fMRI: Functional connectivity-based parcellation method. Neuroimage. 2010; 49: 2375–2386. doi: 10.1016/j.neuroimage.2009.10.016 PMID: 19837176

29. Chen S, Ross TJ, Zhan W, Myers CS, Chuang KS, Heishman SJ, et al. Group independent component analysis reveals consistent resting-state networks across multiple sessions. Brain Res. 2008; 1239: 141–151. doi: 10.1016/j.brainres.2008.08.028 PMID: 18789314

30. Jafri MJ, Pearlson GD, Stevens M, Calhoun VD. A method for functional network connectivity among spatially independent resting-state components in schizophrenia. Neuroimage. 2008; 39: 1666–1681. PMID: 18082428

31. Joel SE, Caffo BS, van Zijl PC, Pekar JJ. On the relationship between seed-based and ICA-based measures of functional connectivity. Magn Reson Med. 2011; 66: 644–657. doi: 10.1002/mrm.22818 PMID: 21394769

32. Power JD, Barnes KA, Snyder AZ, Schlaggar BL, Petersen SE. Spurious but systematic correlations in functional connectivity MRI networks arise from subject motion. Neuroimage. 2012; 59: 2142–2154. doi: 10.1016/j.neuroimage.2011.10.018 PMID: 22019881

33. Friedman L, Glover GH. Report on a multicenter fMRI quality assurance protocol. J Magn Reson Imaging. 2006; 23: 827–839. PMID: 16649196

34. Ahdesmaki M, Lahdesmaki H, Pearson R, Huttunen H, Yli-Harja O. Robust detection of periodic time series measured from biological systems. BMC Bioinformatics. 2005; 6: 117. PMID: 15892890

35. Ahdesmaki M, Lahdesmaki H, Gracey A, Shmulevich L, Yli-Harja O. Robust regression for periodicity detection in non-uniformly sampled time-course gene expression data. BMC Bioinformatics. 2007; 8: 233. PMID: 17605777

36. Broersen PMT, de Waele S, Bos R. Autoregressive spectral analysis when observations are missing. Automatica. 2004; 40: 1495–1504.

37. Broersen PMT. Automatic spectral analysis with missing data. Digital Signal Processing. 2006; 16: 754–766.

38. Meindl T, Teipel S, Elmouden R, Mueller S, Koch W, Dietrich O, et al. Test-retest reproducibility of the default-mode network in healthy individuals. Hum Brain Mapp. 2010; 31: 237–246. doi: 10.1002/hbm.20860 PMID: 19621371

39. Li Z, Kadivar A, Pluta J, Dunlop J, Wang Z. Test-retest stability analysis of resting brain activity revealed by blood oxygen level-dependent functional MRI. J Magn Reson Imaging. 2012; 36: 344–354. doi: 10.1002/jmri.23670 PMID: 22535702

40. Wisner KM, Atluri G, Lim KO, Macdonald AW 3rd. Neurometrics of intrinsic connectivity networks at rest using fMRI: Retest reliability and cross-validation using a meta-level method. Neuroimage. 2013; 76: 236–251. doi: 10.1016/j.neuroimage.2013.02.066 PMID: 23507379

41. Damoiseaux JS, Rombouts SA, Barkhof F, Scheltens P, Stam CJ, Smith SM, et al. Consistent resting-state networks across healthy subjects. Proc Natl Acad Sci U S A. 2006; 103: 13848–13853. PMID: 16945915

42. Guo CC, Kurth F, Zhou J, Mayer EA, Eickhoff SB, Kramer JH, et al. One-year test-retest reliability of intrinsic connectivity network fMRI in older adults. Neuroimage. 2012; 61: 1471–1483. doi: 10.1016/j.neuroimage.2012.03.027 PMID: 22446491

43. Raichle ME, MacLeod AM, Snyder AZ, Powers WJ, Gusnard DA, Shulman GL. A default mode of brain function. Proc Natl Acad Sci U S A. 2001; 98: 676–682. PMID: 11209064

44. Weiland BJ, Sabbineni A, Calhoun VD, Welsh RC, Hutchison KE. Reduced executive and default network functional connectivity in cigarette smokers. Hum Brain Mapp. 2014.

45. Seeley WW, Menon V, Schatzberg AF, Keller J, Glover GH, Kenna H, et al. Dissociable intrinsic connectivity networks for salience processing and executive control. J Neurosci. 2007; 27: 2349–2356. PMID: 17329432

46. Segall JM, Allen EA, Jung RE, Erhardt EB, Arja SK, Kiehl K, et al. Correspondence between structure and function in the human brain at rest. Front Neuroinform. 2012; 6: 10. doi: 10.3389/fninf.2012.00010 PMID: 22470337

47. Kosslyn SM. Mental images and the brain. Cogn Neuropsychol. 2005; 22: 333–347. doi: 10.1080/02643290442000130 PMID: 21038254

48. Miller MI, Beg MF, Ceritoglu C, Stark C. Increasing the power of functional maps of the medial temporal lobe by using large deformation diffeomorphic metric mapping. Proc Natl Acad Sci U S A. 2005; 102: 9685–9690. PMID: 15980148

49. Oishi K, Faria A, Jiang H, Li X, Akhter K, Zhang J, et al. Atlas-based whole brain white matter analysis using large deformation diffeomorphic metric mapping: Application to normal elderly and alzheimer's disease participants. Neuroimage. 2009; 46: 486–499. PMID: 19385016

50. Yang Z, Zuo XN, Wang P, Li Z, LaConte SM, Bandettini PA, et al. Generalized RAICAR: Discover homogeneous subject (sub)groups by reproducibility of their intrinsic connectivity networks. Neuroimage. 2012; 63: 403–414. doi: 10.1016/j.neuroimage.2012.06.060 PMID: 22789741

51. Krmpotich TD, Tregellas JR, Thompson LL, Banich MT, Klenk AM, Tanabe JL. Resting-state activity in the left executive control network is associated with behavioral approach and is increased in substance dependence. Drug Alcohol Depend. 2013; 129: 1–7. doi: 10.1016/j.drugalcdep.2013.01.021 PMID: 23428318

52. Samann PG, Wehrle R, Hoehn D, Spoormaker VI, Peters H, Tully C, et al. Development of the brain's default mode network from wakefulness to slow wave sleep. Cereb Cortex. 2011; 21: 2082–2093. doi: 10.1093/cercor/bhq295 PMID: 21330468

53. Mazoyer B, Zago L, Mellet E, Bricogne S, Etard O, Houde O, et al. Cortical networks for working memory and executive functions sustain the conscious resting state in man. Brain Res Bull. 2001; 54: 287–298. PMID: 11287133

54. Agosta F, Pievani M, Geroldi C, Copetti M, Frisoni GB, Filippi M. Resting state fMRI in alzheimer's disease: Beyond the default mode network. Neurobiol Aging. 2012; 33: 1564–1578. doi: 10.1016/j.neurobiolaging.2011.06.007 PMID: 21813210

55. Ge Y, Grossman RI, Babb JS, Rabin ML, Mannon LJ, Kolson DL. Age-related total gray matter and white matter changes in normal adult brain. part I: Volumetric MR imaging analysis. AJNR Am J Neuroradiol. 2002; 23: 1327–1333. PMID: 12223373

56. Pfefferbaum A, Mathalon DH, Sullivan EV, Rawles JM, Zipursky RB, Lim KO. A quantitative magnetic resonance imaging study of changes in brain morphology from infancy to late adulthood. Arch Neurol. 1994; 51: 874–887. PMID: 8080387

57. Courchesne E, Chisum HJ, Townsend J, Cowles A, Covington J, Egaas B, et al. Normal brain development and aging: Quantitative analysis at in vivo MR imaging in healthy volunteers. Radiology. 2000; 216: 672–682. PMID: 10966694

58. Webb SJ, Monk CS, Nelson CA. Mechanisms of postnatal neurobiological development: Implications for human development. Dev Neuropsychol. 2001; 19: 147–171. PMID: 11530973

59. Jones CK, Calabresi PA, Barker PB, van Zijl PC. Weekly scanning of a normal control over four years. 22nd Scientific Meeting and Exhibition, International Society of Magnetic Resonance in Medicine 2014, Milan Italy. 2014: 1775.

60. Geerligs L, Renken RJ, Saliasi E, Maurits NM, Lorist MM. A brain-wide study of age-related changes in functional connectivity. Cereb Cortex. 2014.

61. Vogel AC, Power JD, Petersen SE, Schlaggar BL. Development of the brain's functional network architecture. Neuropsychol Rev. 2010; 20: 362–375. doi: 10.1007/s11065-010-9145-7 PMID: 20976563

62. Sato JR, Salum GA, Gadelha A, Picon FA, Pan PM, Vieira G, et al. Age effects on the default mode and control networks in typically developing children. J Psychiatr Res. 2014; 58C: 89–95.

63. Koch W, Teipel S, Mueller S, Buerger K, Bokde AL, Hampel H, et al. Effects of aging on default mode network activity in resting state fMRI: Does the method of analysis matter? Neuroimage. 2010; 51: 280–287. doi: 10.1016/j.neuroimage.2009.12.008 PMID: 20004726

64. Damoiseaux JS, Beckmann CF, Arigita EJ, Barkhof F, Scheltens P, Stam CJ, et al. Reduced resting-state brain activity in the "default network" in normal aging. Cereb Cortex. 2008; 18: 1856–1864. PMID: 18063564

65. Andrews-Hanna JR, Snyder AZ, Vincent JL, Lustig C, Head D, Raichle ME, et al. Disruption of large-scale brain systems in advanced aging. Neuron. 2007; 56: 924–935. PMID: 18054866

66. Fair DA, Cohen AL, Dosenbach NU, Church JA, Miezin FM, Barch DM, et al. The maturing architecture of the brain's default network. Proc Natl Acad Sci U S A. 2008; 105: 4028–4032. doi: 10.1073/pnas.0800376105 PMID: 18322013

67. Karunanayaka PR, Holland SK, Schmithorst VJ, Solodkin A, Chen EE, Szaflarski JP, et al. Age-related connectivity changes in fMRI data from children listening to stories. Neuroimage. 2007; 34: 349–360. PMID: 17064940

68. Szaflarski JP, Holland SK, Schmithorst VJ, Byars AW. fMRI study of language lateralization in children and adults. Hum Brain Mapp. 2006; 27: 202–212. PMID: 16035047

69. Kramer AF, Bherer L, Colcombe SJ, Dong W, Greenough WT. Environmental influences on cognitive and brain plasticity during aging. J Gerontol A Biol Sci Med Sci. 2004; 59: M940–57. PMID: 15472160

70. Pesonen AK, Eriksson JG, Heinonen K, Kajantie E, Tuovinen S, Alastalo H, et al. Cognitive ability and decline after early life stress exposure. Neurobiol Aging. 2013; 34: 1674–1679. doi: 10.1016/j. neurobiolaging.2012.12.012 PMID: 23337341

71. Yamada H, Yamamoto MT. Association between circadian clock genes and diapause incidence in drosophila triauraria. PLoS One. 2011; 6: e27493. doi: 10.1371/journal.pone.0027493 PMID: 22164210

72. Merrow M, Spoelstra K, Roenneberg T. The circadian cycle: Daily rhythms from behaviour to genes. EMBO Rep. 2005; 6: 930–935. PMID: 16222241

73. Paredes SD, Marchena AM, Bejarano I, Espino J, Barriga C, Rial RV, et al. Melatonin and tryptophan affect the activity-rest rhythm, core and peripheral temperatures, and interleukin levels in the ringdove: Changes with age. J Gerontol A Biol Sci Med Sci. 2009; 64: 340–350. doi: 10.1093/gerona/gln054 PMID: 19211547

74. Schmidt C, Collette F, Cajochen C, Peigneux P. A time to think: Circadian rhythms in human cognition. Cogn Neuropsychol. 2007; 24: 755–789. PMID: 18066734

75. Kent BA. Synchronizing an aging brain: Can entraining circadian clocks by food slow alzheimer's disease? Front Aging Neurosci. 2014; 6: 234. doi: 10.3389/fnagi.2014.00234 PMID: 25225484

76. Anderson JA, Campbell KL, Amer T, Grady CL, Hasher L. Timing is everything: Age differences in the cognitive control network are modulated by time of day. Psychol Aging. 2014; 29: 648–657. doi: 10. 1037/a0037243 PMID: 24999661

77. Blautzik J, Vetter C, Peres I, Gutyrchik E, Keeser D, Berman A, et al. Classifying fMRI-derived resting-state connectivity patterns according to their daily rhythmicity. Neuroimage. 2013; 71: 298–306. doi: 10. 1016/j.neuroimage.2012.08.010 PMID: 22906784

78. Blautzik J, Vetter C, Schneider A, Gutyrchik E, Reinisch V, Keeser D, et al. Dysregulated daily rhythmicity of neuronal resting-state networks in MCI patients. Chronobiol Int. 2014; 1–10.

79. Hodkinson DJ, O'Daly O, Zunszain PA, Pariante CM, Lazurenko V, Zelaya FO, et al. Circadian and homeostatic modulation of functional connectivity and regional cerebral blood flow in humans under normal entrained conditions. J Cereb Blood Flow Metab. 2014; 34: 1493–1499. doi: 10.1038/jcbfm. 2014.109 PMID: 24938404

80. Hjelmervik H, Hausmann M, Osnes B, Westerhausen R, Specht K. Resting states are resting traits—an FMRI study of sex differences and menstrual cycle effects in resting state cognitive control networks. PLoS One. 2014; 9: e103492. doi: 10.1371/journal.pone.0103492 PMID: 25057823

81. Sandler RA, Song D, Hampson RE, Deadwyler SA, Berger TW, Marmarelis VZ. Model-based asessment of an in-vivo predictive relationship from CA1 to CA3 in the rodent hippocampus. J Comput Neurosci. 2014.

82. Stanculescu I, Williams CK, Freer Y. Autoregressive hidden markov models for the early detection of neonatal sepsis. IEEE J Biomed Health Inform. 2014; 18: 1560–1570. doi: 10.1109/JBHI.2013. 2294692 PMID: 25192568

83. Shehzad Z, Kelly AM, Reiss PT, Gee DG, Gotimer K, Uddin LQ, et al. The resting brain: Unconstrained yet reliable. Cereb Cortex. 2009; 19: 2209–2229. doi: 10.1093/cercor/bhn256 PMID: 19221144

84. Schmithorst VJ, Holland SK. Comparison of three methods for generating group statistical inferences from independent component analysis of functional magnetic resonance imaging data. J Magn Reson Imaging. 2004; 19: 365–368. PMID: 14994306

85. Amann M, Hirsch JG, Gass A. A serial functional connectivity MRI study in healthy individuals assessing the variability of connectivity measures: Reduced interhemispheric connectivity in the motor network during continuous performance. Magn Reson Imaging. 2009; 27: 1347–1359. doi: 10.1016/j.mri. 2009.05.016 PMID: 19559557

86. Anderson JS, Ferguson MA, Lopez-Larson M, Yurgelun-Todd D. Reproducibility of single-subject functional connectivity measurements. AJNR Am J Neuroradiol. 2011; 32: 548–555. doi: 10.3174/ajnr. A2330 PMID: 21273356

87. Chou YH, Panych LP, Dickey CC, Petrella JR, Chen NK. Investigation of long-term reproducibility of intrinsic connectivity network mapping: A resting-state fMRI study. AJNR Am J Neuroradiol. 2012; 33: 833–838. doi: 10.3174/ajnr.A2894 PMID: 22268094

88. Seibert TM, Majid DS, Aron AR, Corey-Bloom J, Brewer JB. Stability of resting fMRI interregional correlations analyzed in subject-native space: A one-year longitudinal study in healthy adults and premanifest huntington's disease. Neuroimage. 2012; 59: 2452–2463. doi: 10.1016/j.neuroimage.2011.08.105 PMID: 21945695

89. Zuo XN, Kelly C, Adelstein JS, Klein DF, Castellanos FX, Milham MP. Reliable intrinsic connectivity networks: Test-retest evaluation using ICA and dual regression approach. Neuroimage. 2010; 49: 2163–2177. doi: 10.1016/j.neuroimage.2009.10.080 PMID: 19896537